UNIVERSIDADE FEDERAL DE SÃO CARLOS
CENTRO DE CIÊNCIAS EXATAS E DE TECNOLOGIA
PROGRAMA DE PÓS-GRADUAÇÃO EM CIÊNCIA E ENGENHARIA DE MATERIAIS

DESIGN, PROCESSING, AND CHARACTERIZATION OF HIGH STRENGTH PRECIPITATION-HARDENED CrCoNiAlTi HIGH ENTROPY ALLOYS

Diego de Araujo Santana

São Carlos - SP
2023

UNIVERSIDADE FEDERAL DE SÃO CARLOS
CENTRO DE CIÊNCIAS EXATAS E DE TECNOLOGIA
PROGRAMA DE PÓS-GRADUAÇÃO EM CIÊNCIA E ENGENHARIA DE MATERIAIS

DESIGN, PROCESSING, AND CHARACTERIZATION OF HIGH STRENGTH PRECIPITATION-HARDENED CrCoNiAlTi HIGH ENTROPY ALLOYS

Diego de Araujo Santana

A thesis submitted to Graduate Program in Materials Science and Engineering as a requirement for the degree of DOCTOR IN MATERIALS SCIENCE AND ENGINEERING.

Thesis advisor: Dr. Francisco Gil Coury
Thesis co-advisor: Dr. Claudio Shyinti Kiminami
Funding agencies: CNPq (grant: 167552/2018-0) and FAPESP (grant: 2018/26390-3) with BEPE internship at the Colorado School of Mines (grant: 2021/10997-9).

São Carlos - SP
2023

DEDICATION

To my mother, who has been always a source of love and inspiration to me.

VITAE OF CANDIDATE

Master of Science in Materials Science and Engineering from Universidade Federal de São Carlos (2018). Bachelor in Metallurgical Engineering from Universidade Federal de Ouro Preto (2015).

UNIVERSIDADE FEDERAL DE SÃO CARLOS

Centro de Ciências Exatas e de Tecnologia
Programa de Pós-Graduação em Ciência e Engenharia de Materiais

Folha de Aprovação

Defesa de Tese de Doutorado do candidato Diego de Araujo Santana, realizada em 22/03/2023.

Comissão Julgadora:

Prof. Dr. Francisco Gil Coury (UFSCar)

Prof. Dr. Claudemiro Bolfarini (UFSCar)

Prof. Dr. Guilherme Zepon (UFSCar)

Prof. Dr. Michael Joseph Kaufman (Mines)

Prof. Dr. Witor Wolf (UFMG)

O Relatório de Defesa assinado pelos membros da Comissão Julgadora encontra-se arquivado junto ao Programa de Pós-Graduação em Ciência e Engenharia de Materiais.

ACKNOWLEDGMENTS

I would like to express my gratitude to the Conselho Nacional de Desenvolvimento Científico e Tecnológico (CNPq), doctoral grant #167552/2018-0, and to the Fundação de Amparo à Pesquisa do Estado de São Paulo (FAPESP), doctoral grant #2018/26390-3 and BEPE grant #2021/10997-9, for their financial support. This study was financed in part by the Coordenação de Aperfeiçoamento de Pessoal de Nível Superior - Brasil (CAPES) - Finance Code 001.

I would like to thank my advisor, Prof. Francisco Coury, for his guidance, teachings, friendship, patience, opportunities, and support. I am also grateful to Prof. Claudio Kiminami for his co-advising, encouragement, and all the attention and teachings over the years. You are both professional and personal examples to me.

I extend my appreciation to Prof. Michael Kaufman and Garritt Tucker for their teachings, patience, and attention. I am also thankful to Amy Clarke and Kester Clarke for their invaluable assistance.

I thank all my colleagues from the Mezanino, LHM, Solidification Laboratory, and Corrosion Laboratory for their help, advice, and fun moments. I would like to express my gratitude to Nelson, Renata, Lucas, and Carol for the support and countless enjoyable moments we shared during my stay in Golden.

I am indebted to laboratory technicians Beto and Rolver. I would like to thank the postdoctoral Benjamin Ellyson and the undergraduate research student Kayque Rodrigues for their assistance with the experimental part of this work. I also thank LCE and its members for the coffee breaks and assistance with microscopy and sample preparations.

I am grateful to PPGCEM/DEMa/UFSCar for the excellence in teaching and infrastructure, as well as to the Colorado School of Mines for providing me with all the necessary resources during my BEPE internship.

I would like to acknowledge my girlfriend, Mariana, for her love, care, attention, and support throughout my journey.

Lastly, I express my deepest gratitude to my parents and my nephew for their unconditional love and unwavering support.

ABSTRACT

High Entropy Alloys (HEAs) have been attracting considerable interest in literature. While early studies focused on producing single-phase HEAs, more recent investigations have expanded to multi-phase compositions to take advantage of precipitation hardening or other benefits of having multiple phases in the microstructure. In this work, two approaches were used to design precipitation-hardened HEAs with an FCC matrix and $L1_2$ precipitates. In the first approach, the focus was to introduce $L1_2$ precipitates into a highly concentrated Cr-Co-Ni matrix. The $Cr_{29.7}Co_{29.7}Ni_{35.4}Al_{4.0}Ti_{1.2}$ (at. %) alloy was designed using the CALPHAD method by replacing some Cr, Co, and Ni with Al and Ti, so that an FCC+$L1_2$ field was stable at high temperatures. This alloy was produced, processed, and characterized. The results showed that the precipitates were effective in increasing the yield stress of the alloy by about ~55% compared to its homogenized counterpart. Moreover, this approach yielded insights for designing new precipitation-hardened HEAs with optimized strength. In this context, a second approach was proposed to effectively explore the large compositional landscape typical of these multi-component systems and design strong HEAs with an FCC matrix and $L1_2$ precipitates. Specifically, thermodynamic calculations using the CALPHAD method were used to screen a series of Cr-Co-Ni-Al-Ti alloys. A total of 11235 compositions was analyzed. After applying specific filtering criteria, the remaining alloys had their solid solution hardening and maximum precipitation hardening contributions to yield strength estimated. To assess the effectiveness of the proposed methodology, three alloys were selected, processed, and characterized using various microstructural and mechanical characterization techniques. The good qualitative agreement between the results and predictions suggests that the approach taken in this study has the potential to significantly expedite the identification and development of new precipitation-hardened alloys with optimized mechanical properties, making it a promising pathway for future research.

Keywords: High Entropy Alloys; Multicomponent Alloys; Multi-principal element alloys; Complex and Concentrated Alloys; Superalloys; Precipitation Hardening.

RESUMO

DESENVOLVIMENTO, PROCESSAMENTO E CARACTERIZAÇÃO DE LIGAS DE ALTA ENTROPIA CrCoNiAlTi DE ALTA RESISTÊNCIA ENDURECIDAS POR PRECIPITAÇÃO

Ligas de alta entropia (LAE) têm despertado considerável interesse na literatura. Enquanto estudos iniciais focaram na produção de LEA monofásicas, trabalhos mais recentes expandiram-se para composições multifásicas para possibilitar o endurecimento por precipitação ou outros benefícios de ter múltiplas segunda fases na microestrutura. Neste trabalho, duas abordagens foram utilizadas para desenvolver LAE endurecidas por precipitação com uma matriz CFC e precipitados $L1_2$. Na primeira abordagem, o foco foi introduzir precipitados $L1_2$ em uma matriz Cr-Co-Ni altamente concentrada. A liga $Cr_{29.7}Co_{29.7}Ni_{35.4}Al_{4.0}Ti_{1.2}$ (%at.) foi projetada usando o método CALPHAD, substituindo parte de Cr, Co e Ni por Al e Ti, de modo que um campo CFC + $L1_2$ fosse estável em altas temperaturas. Essa liga foi produzida, processada e caracterizada. Os resultados mostraram que os precipitados foram eficazes em aumentar o limite de escoamento da liga em cerca de ~55% em comparação com sua contraparte homogeneizada. Além disso, essa abordagem proporcionou ideias para o desenvolvimento de novas LAE endurecidas por precipitação com resistência mecânica otimizada. Nesse contexto, uma segunda abordagem foi proposta para explorar efetivamente o vasto espaço composicional típico desses sistemas multi-componentes e desenvolver LAE resistentes com matriz CFC e precipitados $L1_2$. Especificamente, cálculos termodinâmicos usando o método CALPHAD foram usados para varrer uma série de ligas do Sistema Cr-Co-Ni-Al-Ti. Um total de 11235 composições foi analisado. Após aplicação de alguns critérios de filtragem, as ligas restantes tiveram seu endurecimento por solução sólida e as contribuição máxima de endurecimento por precipitação para o limite de escoamento estimados. Para avaliar a eficácia da metodologia proposta, três ligas foram selecionadas, processadas e caracterizadas usando várias técnicas de caracterização microestrutural e mecânica. A boa concordância qualitativa entre os resultados

e as previsões sugere que a abordagem adotada neste estudo tem o potencial de acelerar significativamente a identificação e o desenvolvimento de novas ligas endurecidas por precipitação com propriedades mecânicas otimizadas, tornando-se um caminho promissor para pesquisas futuras.

Palavras-chaves: Ligas de Alta Entropia; Ligas Multicomponentes; Ligas Multi-elementos Principais; Superligas; Endurecimento por Precipitação.

PUBLICATIONS

Journal articles:

- J.G. Lopes, P. Rocha, **D. A. Santana,** J. Shen, E. Maawad, N. Schell, F. G. Coury, J. P. Oliveira. Impact of arc-based welding on the microstructure evolution and mechanical properties in newly developed $Cr_{29.7}Co_{29.7}Ni_{35.4}Al_4Ti_{1.2}$ multi-principal element alloy. ADVANCED ENGINEERING MATERIALS, 2023. https://doi.org/10.1002/adem.202300109.
- **D. de Araujo Santana**, C.S. Kiminami, F.G. Coury. Mechanical properties and yield strength modeling of a medium entropy alloy containing $L1_2$ precipitates, Journal of Alloys and Compounds, 898 (2022) 162923. https://doi.org/10.1016/j.jallcom.2021.162923.
- **D. A. Santana**, K. R. Santos, C. S. Kiminami, F. G. Coury. Design, phase equilibria, and coarsening kinetics of a new γ/γ′ precipitation-hardened multi-principal element alloy, Journal of Alloys and Compounds, v. 882, p. 160729, 2021. https://doi.org/10.1016/j.jallcom.2021.160729.

Presentation in Congress:

- **Diego de Araujo Santana**, Michael Kaufman, Amy Clarke, Kester Clarke, Garritt Tucker, Claudio Shyinti Kiminami e Francisco Gil Coury. Desenvolvimento de ligas de alta entropia com matriz CFC, precipitados $L1_2$ e propriedades mecânicas otimizadas - Uma nova abordagem para exploração do vasto espaço composicional. In: **24° Congresso Brasileiro de Ciência e Engenharia de Materiais (24° CBCiMat)**, Água de Lindóia/Brazil, 2022. Presented by: Diego Santana. Presentation format: in person oral presentation.
- **Diego de Araujo Santana**, Kayque R. dos Santos, Claudio S. Kiminami, Francisco G. Coury. Design e caracterização de uma liga multicomponente endurecida por precipitação. In: **24° Congresso Brasileiro de Ciência e Engenharia de Materiais (24° CBCiMat)**, Água

de Lindóia/Brazil, 2022. Presented by: Diego Santana. Presentation format: in person poster presentation.

- **Diego de Araujo Santana**, Claudio Kiminami, Francisco Coury. Microstructural and Mechanical Characterization of a Concentrated FCC Cr-Co-Ni Matrix Containing Dispersed L12 Precipitates. In: **2nd World Congress on High Entropy Alloys (HEA 2021)**, Charlotte/EUA, 2021. Presented by: Diego Santana. Presentation format: in person oral presentation.

- **D. A. Santana**, K.R. Santos, C.S. Kiminami, F.G. Coury. Microstructural characterization of the $Cr_{29.7}Co_{29.7}Ni_{35.4}Al_{4.0}Ti_{1.2}$ precipitation-hardened multi-principal element alloy. In: **Congresso da Sociedade Brasileira de Microscopia e Microanálise (CSBMM) 2021**. Presented by: Diego Santana. Presentation format: virtual oral presentation.

- **D. A. Santana**, K.R. Santos, C.S. Kiminami, F.G. Coury. Design and characterization of $Cr_{29.7}Co_{29.7}Ni_{35.4}Al_{4.0}Ti_{1.2}$ precipitation hardened high entropy alloy. In: **Entropy 2021 – The Scientific Tool of the 21st Century. 2021.** Presented by: Diego Santana. Presentation format: virtual poster presentation.

TABLE OF CONTENTS

Page

LIST OF TABLES

Page

LIST OF FIGURES

Page

1 INTRODUCTION

The strategy for developing most alloys until the early 2000s was focused on the choice of a "solvent", based on the main property of interest, and the addition of alloying elements to impart secondary properties [1]. As of 2004 new alloys consisting of a mixture of several elements, but without the presence of a main element have been reported in the literature [2–6].

Yeh and coworkers named these new materials as High Entropy Alloys (HEA) [2,3,6]. These researchers theorized that when 3 or more elements were mixed in or near equiatomic compositions, due to the high configurational entropy of the mixture, the tendency to form intermetallic compounds would be reduced, since the product $-T\Delta S_{conf}$ could dominate with respect to the mixing enthalpy and other entropic contributions. Hence, single-phase alloys would be more likely to be formed. Furthermore, it was speculated that these alloys would have a high solid solution hardening component and that the elements would have a low diffusivity through the matrix [7,8]. At the same time, in another current of thought, where the main intention was to explore the central region of the compositional space of alloys formed by various elements, Cantor et. al [1,5] published a paper in which up to twenty elements were mixed in equiatomic proportions and called these alloys multicomponent alloys.

This work has attracted the interest of several researchers around the world and the number of papers related to the terms “high entropy alloys” and “multicomponent alloys” has been growing every year [9]. Specially because alloys with very interesting properties have also been reported in the literature, such as the CrCoNi alloy, which is one of the toughest materials ever discovered.

With significant academic and industrial interest in this new class of materials, new alloys have been reported, as well as theoretical models for predicting specific properties have been developed when concentrated solutions with three or more elements are analyzed [10–16].

Although there has been significant interest in these new alloys, most research has primarily focused on the development of single-phase materials. However, more recent studies have expanded to explore multi-phase

compositions to take advantage of precipitation hardening or other benefits of having multiple second phases in the microstructure.

In this context, two different approaches were used in this work to design precipitation-hardened high entropy alloys. In the first, the focus was to introduce $L1_2$ precipitates in a highly concentrated FCC Cr-Co-Ni matrix. In the second, a strategy to design new alloys with FCC matrix, $L1_2$ precipitates, and optimized yield stress in the Cr-Co-Ni-Al-Ti system was developed. To test the latter methodology, three alloys were selected. In both approaches, the alloys were produced, processed, and characterized by various microstructural and mechanical characterization techniques. Overall, the design strategy presents new opportunities for the development of precipitation-hardened alloys and can be extended to other systems.

2 OBJECTIVE

This dissertation aimed to employ a comprehensive approach to design, process, and characterize new high entropy alloys with FCC matrix, $L1_2$ precipitates, and optimized yield stress.

3 LITERATURE REVIEW

In this chapter, a literature review is presented on high entropy alloys as well as solid solution and precipitation hardening models in concentrated alloys with FCC/$L1_2$ microstructure. Furthermore, a section is dedicated to antiphase boundary energy, an essential parameter for the development of alloys hardened by ordered particles.

3.1 High Entropy Alloys

High Entropy Alloys (HEA) or Multi-Component Alloys (MA) are different names for a new class of materials composed of a mixture of several elements and without a single main element [7,9,17–19].

Cantor et al. [5] have proposed the term multi-component alloys to refer to this new class of materials. In their studies the main goal was to explore the central region of the compositional space of alloys formed by several elements.

The term High Entropy Alloys was coined by Yeh et. al [7,9]. These researchers defined specific criteria for classifying an alloy as a high entropy alloy:

- **Composition-based definition:** the composition of all the elements of the alloy must be within the range of 5 and 35 at. %;
- **Configurational entropy-based definition:** the configurational entropy of an ideal solid solution formed with the alloy composition must exceed 1.5 R.

Miracle e Senkov [9], in one of the most highly cited reviews on the subject of high entropy alloys, provided the following interpretation of the terms used in the literature over the last two decades:

- ***Multi-principal element alloys (MPEAs)*, *Complex Concentrated Alloys (CCAs)* or *Baseless Alloys*:** these terms should be used when the study's motivation is to investigate the central region of the compositional space of multi-component alloys;

- ***High Entropy Alloys*:** this term should be used when the study's focus is on the configurational entropy, or the objective is to produce single-phase alloys.

As can be observed, there are at least five terms that appear in the literature related to this new class of alloys: high entropy alloys, multicomponent alloys, multi-principal element alloys, complex concentrated alloys, and baseless alloys. However, as can be seen in Figure 3.1, the term "High Entropy Alloys" has become popular, and much of the work in the literature adopts this nomenclature, regardless of whether the motivation of the study is to produce single-phase alloys, or the definition of high entropy alloy proposed by Yeh is followed. Therefore, in this work, we use the different terms interchangeably.

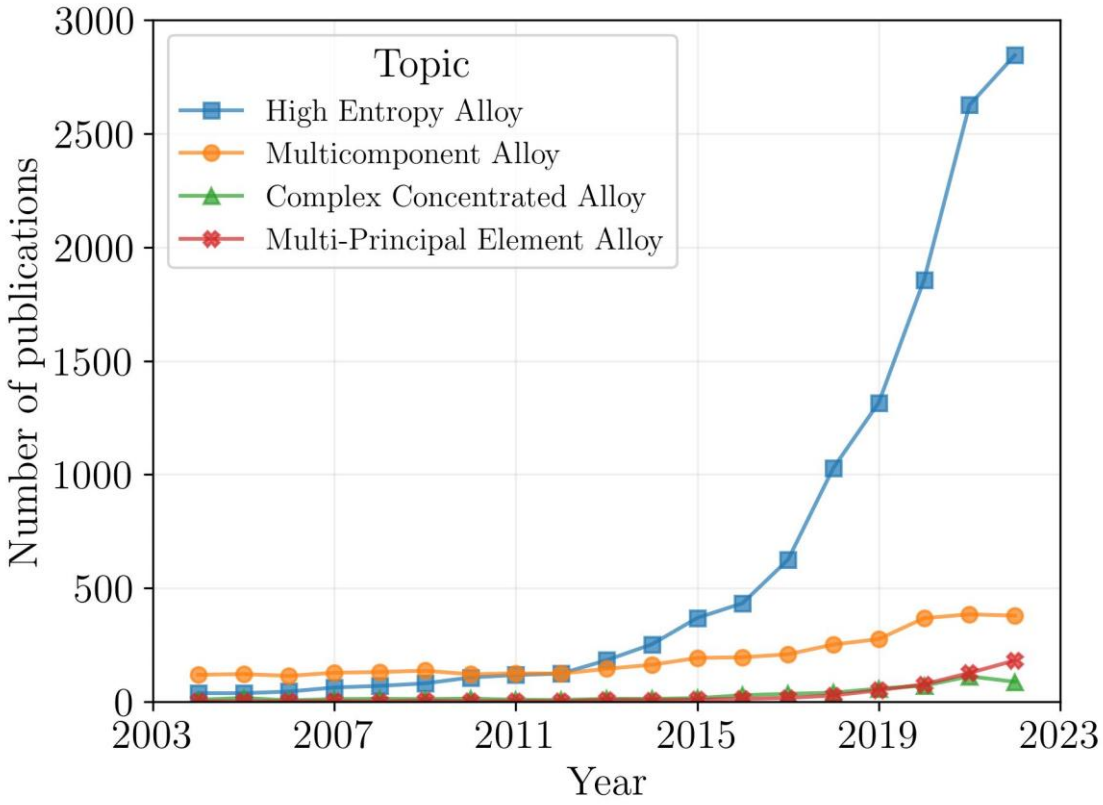

Figure 3.1: Number of publications per year since 2004 with the search topic "High Entropy Alloy", "Multicomponent Alloy", "Multi-principal Element Alloy" and "Complex and Concentrated Alloy". Data extracted from the Web of Science database.

Initially, HEAs were developed to have simple phases, such as body centered cubic (BCC) or face centered cubic (FCC). It was speculated that these phases would often be stable because of their high configurational entropies [20,21]. This has been proven false on several occasions, the phases in LAEs depend strongly on the elements that are mixed. For example, Borg and coworkers [22] compiled a dataset from various HEAs reported in the literature. Filtering out those alloys that were annealed, homogenized, or aged prior to microstructural characterization, only 51 out of 106 alloys (48.1%) exhibited a single-phase microstructure.

In addition, it was speculated that these alloys would inherently possess high solid solution component. As shown by Coury et. al. [23,24], this strengthening mechanism has no direct correlation with configurational entropy. A more detailed discussion on this topic is given in the next section of this chapter.

The Cantor alloy (CrMnFeCoNi) was discovered by a trial-and-error approach. Through the exploration sub-sets derived from the original Cantor alloy, Wu and coworkers [25] reported the tensile properties of all single-phase FCC equiatomic alloys in this system. As can be seen in Figure 3.2, the ternary CrCoNi alloy shows the best combination of yield strength and uniform elongation, over a wide temperature range. Besides that, its fracture toughness is one of the highest reported to date, even at cryogenic temperature [26,27].

The corrosion resistance in simulated seawater of ternary CrCoNi alloys and some of its variations were investigated by Koga and coworkers [28]. The authors showed that the studied alloys also present electrochemical corrosion properties comparable to or better than Inconel 625, a common choice for application in a marine environment. Accordingly, CrCoNi alloys might be suitable for applications in aggressive environments, where high damage tolerance and low corrosion rates are crucial.

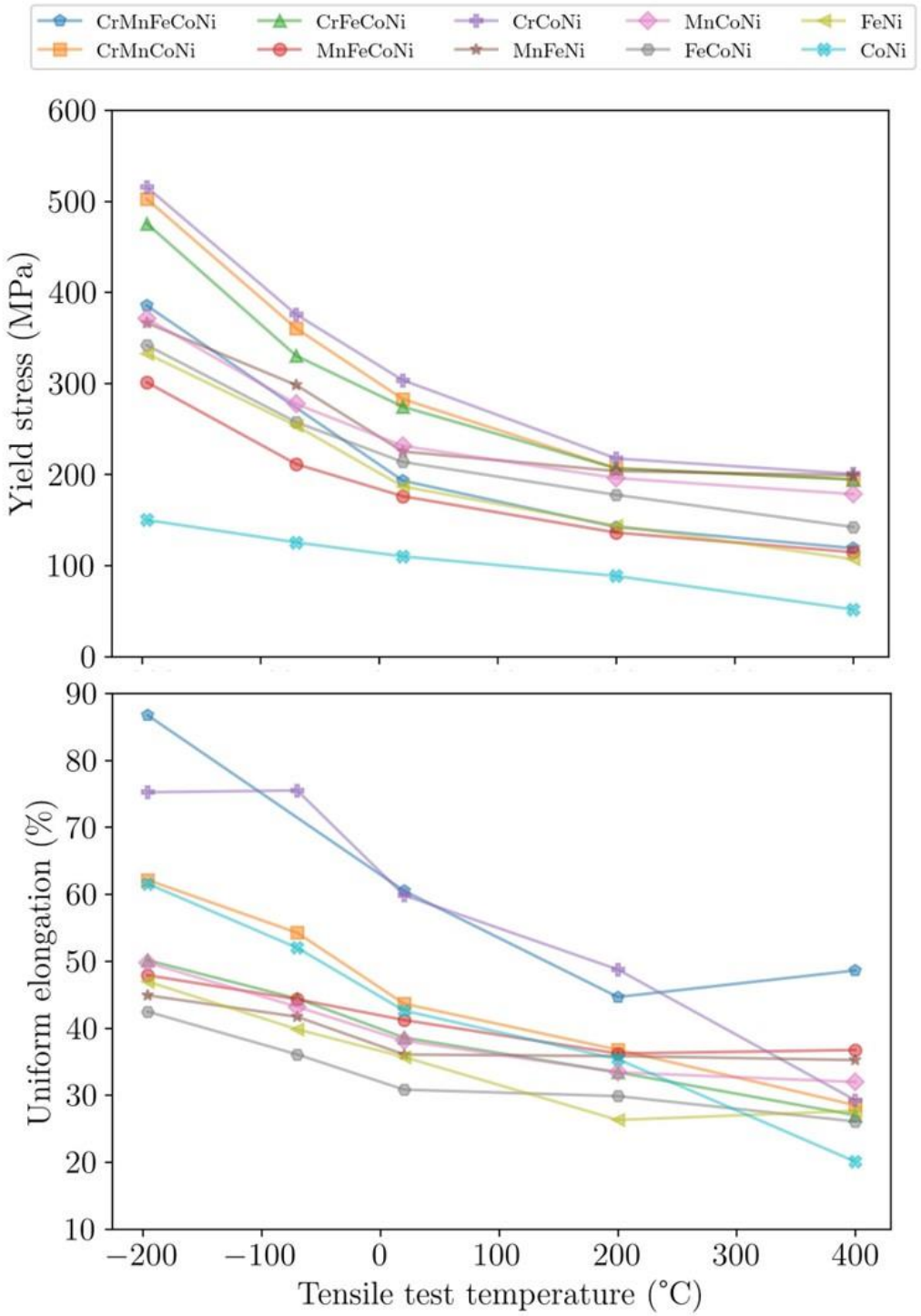

Figure 3.2: Tensile properties of Cantor alloy and their sub-system equiatomic alloys. Data were extracted from [25,29].

The fact that CrCoNi and other alloys with interesting properties have been discovered by trial and error is somewhat surprising, since they exist in a huge compositional landscape. To illustrate this vastness, Figure 3.3 shows the

number of distinct alloy compositions as function of the number of alloying elements (n) and the compositional step (Δx, in molar percentage). As can be seen, over hundreds of alloys can be designed when 3 or more elements are mixed in concentration step of ~10% or lower, which makes experimental investigation by trial and error a hard approach for finding MPEAs with promising properties.

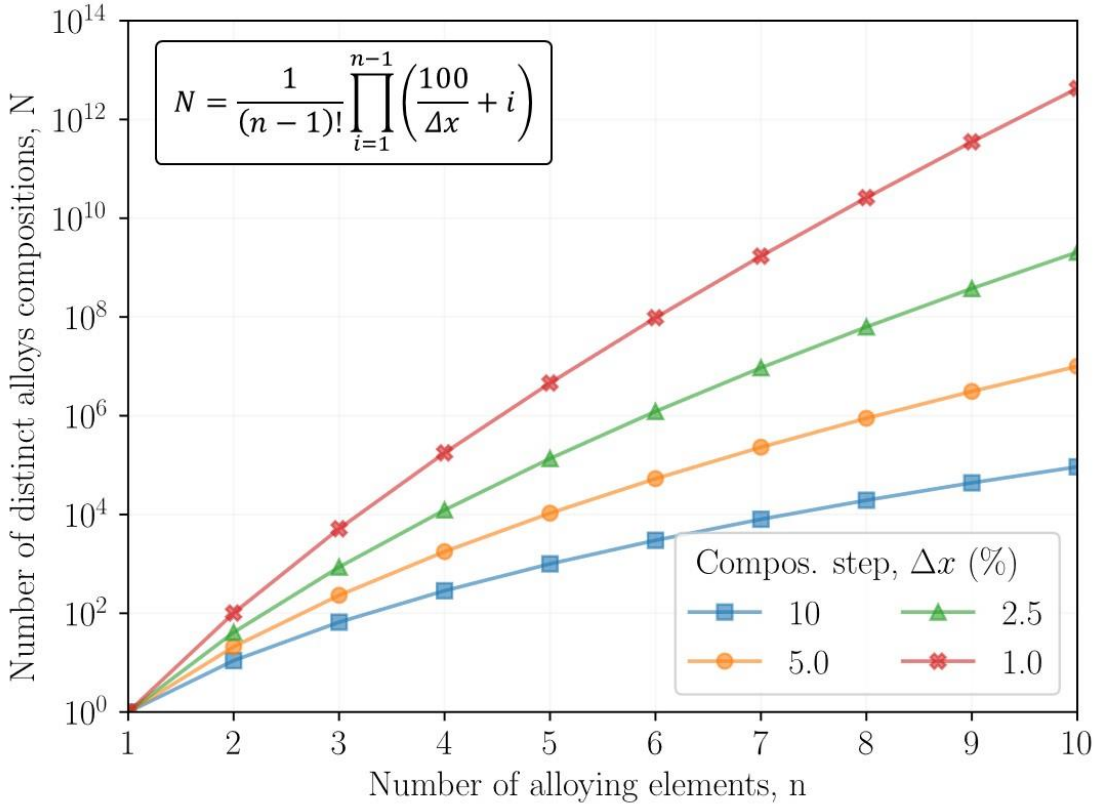

Figure 3.3: Number of alloys compositions (N) as function of the number of alloying elements (n) and the compositional steps (Δx). The inset equation is due to Gorsse et. al. [30].

Therefore, the huge range of possible compositions is a great advantage of HEA but also one of the challenges in the design of new materials with promising properties. In this sense, the use of computationally guided methodologies for the design of new high entropy alloys is crucial.

While the early studies focused on producing single-phase HEAs [25,26], the “second generation” of HEAs has been broadened to include multi-phase

compositions [31]. A particular case is that of alloys with an FCC matrix and $L1_2$ precipitates or with a BCC matrix and B2 precipitates, which are being developed to compete with traditional superalloys [32–36]. These alloys are often named high entropy superalloys (HESA) in the literature. The study of precipitation-hardened HEAs is relatively recent, and few alloys have been studied to date. Therefore, studies focused on designing new alloys with compositions of even greater potential to reconcile strength and ductility are promising.

3.2 Solid Solution Hardening in Concentrated Alloys

The introduction of a second element to a pure metal may lead to the following effects into the resulting crystal structure [37]:

- local distortion of the lattice, caused by the difference in atomic size of the solute-solvent in the case of a substitutional solute or distortion of the lattice around an interstitial solute;
- local difference in bonding strength between atoms, due to difference in bonding energy;
- in FCC alloys, when the solute has a preferential solubility in HCP structure, it may segregate to stacking fault regions (Suzuki effect);
- development of short-range order or clustering when there is a preferential bonding type between the atoms.

These different effects result in various forms of interactions of the solutes with the stress/strain field of dislocations that will cause a local elastic attraction or repulsion. In general, the movement of the dislocations is hindered by these interactions, requiring an additional work to initiate plastic deformation, although in some specific situations the opposite may occur [38].

The most studied types of interaction are those due to the atomic size difference and the difference in bond strength, elastic modulus between solute and solvent. Several models have been proposed to explain solid solution hardening in dilute solutions where the solute has a concentration of up to 20% and that consider the combination of these two effects [38].

With the great academic/industrial interest in high entropy alloys, theories for predicting the solid solution hardening component in concentrated solutions with three or more elements have been proposed [10,12,15,39].

The first paper to propose a mathematical model for solid solution hardening in FCC alloys was published by Toda-Caraballo and coworkers in late 2014 [12]. In this study, the authors started from Labush's model for solid solution [40] and extended it to concentrated multicomponent solutions. Although this model presents a good agreement with experimental data for some alloys, it estimates only the athermal component of the flow stress, the effect of temperature and the strain rate effect is neglected.

For FCC alloy, Varvenne et. al [15] proposed a mechanistic model in which each component of the solid solution can be considered as a "solute" in an "average solvent" that represents the average properties of the alloy. The solvent is then defined as an average matrix with the nominal alloy composition and each element is considered a solute embedded in this average matrix. The "solutes" lead to local compositional fluctuations with respect to the average solvent.

The yield stress of the alloy at 0K is determined by Equation 3.1. The activation energy for the movement of dislocation is given by Equation 3.2.

$$\tau_{y0} = 0.051\alpha^{-\frac{1}{3}}\mu\left(\frac{1+\nu}{1-\nu}\right)f_1(w_c)\left(\frac{\sum_{i=1}^{n} c_i\Delta\bar{V}_i^2}{b^6}\right)^{\frac{2}{3}} \tag{3.1}$$

$$\Delta E_b = 0.274\alpha^{\frac{1}{3}}\mu b^3\left(\frac{1+\nu}{1-\nu}\right)^{\frac{2}{3}} f_2(w_c)\left[\frac{\sum_{i=1}^{n} c_i\Delta\bar{V}_i^2}{b^6}\right]^{\frac{1}{3}} \tag{3.2}$$

where b is modulus of the Burgers vector, μ is the shear modulus and ν is Poisson's ratio. The terms $f_1(w_c)$ and $f_2(w_c)$ are functions related to the core structure of the dislocation, their values are approximately constant and 5.70 and 0.35, respectively. The terms c_i and ΔV_i are the concentration of "solute" *i* and the volume mismatch caused by element *i* in average matrix. The parameter α is a dimensionless constant related to the value of the dislocation line tension, which is given by $\Gamma = \alpha\mu b^2$. For several FCC metals, atomistic simulations show that $\alpha = 1/8$ is a good approximation.

The yield stress correction, due to the thermal contribution, is given by Equations 3.3 and 3.4.

$$\tau_{ss}(T,\dot{\varepsilon}) = \tau_{y0}\exp\left(-\frac{1}{0.51}\frac{kT}{\Delta E_b}\ln\frac{\dot{\varepsilon}_0}{\dot{\varepsilon}}\right) \qquad \frac{\tau_{ss}}{\tau_{ss,0}} \leq 0.5 \qquad (3.3)$$

$$\tau_{ss}(T,\dot{\varepsilon}) = \tau_{y0}\left[1-\left(\frac{kT}{\Delta E_b}\ln\frac{\dot{\varepsilon}_0}{\dot{\varepsilon}}\right)^{\frac{2}{3}}\right] \qquad \frac{\tau_{ss}}{\tau_{ss,0}} \geq 0.5 \qquad (3.4)$$

where k is the Boltzmann constant, T is the temperature, $\dot{\varepsilon_0}$ is the reference strain rate and $\dot{\varepsilon}$ is the experimental strain rate. In the range $0.3 \leq {}^{\tau_y}/_{\tau_{y,0}} \leq 0.6$, Equations 3.3 and 3.4 yield very close results.

As can be seen in the previous equations, to apply the model, some of the alloy's properties must be known in advance, such as the elastic constants and the lattice parameter, which makes it challenging for purposes of designing new alloys. To overcome this problem, a commonly used strategy is to estimate these parameters from available data reported in literature from different alloys. The rule of mixtures ($\bar{V} = \sum_n c_n V_n$) is widely used to estimate the unknown variables. However, it worth mentioning that the linear superposition assumed in this rule may be not followed in practice.

The volume mismatch caused by each element in solution is given by $\Delta\bar{V}_n = V_n - \bar{V}$, where V_n is the apparent volume of the n-th element in the solid solution and $\bar{V}$ is the average atomic volume of the matrix. The latter parameter is related to the lattice parameter of an FCC structure by the equation $\bar{V} = a^3/4$. Since there is no analytical or direct method to measure the V_n in a solid solution, one of the major challenges of applying this model is related to how to estimate V_n.

The simplest approach for estimating V_n involves calculating the atomic volume of the element *n* in its original structure. However, the metals of interest may have different structures in their pure form from that of the solution. For instance, among the metals in Cantor's alloy (CrMnFeCoNi) only Ni has an FCC structure at room temperature. To account for the different atomic packing factors between the structures of the metals and the solution, a conversion factor may be used to estimate V_n. For example, using the rigid sphere model the relationship between atomic volume in FCC and BCC structure can be established as $V_n^{FCC} =$

$\left(3\sqrt{6}/8\right) V_n^{BCC}$. For asymmetric structure, such as HCP with $c/a \neq \sqrt{8}/3$, a direct conversion factor is not possible to be established.

Another way to estimate the atomic volume of the elements in a solid solution is trough A*b initio* methods, as computed by Okamoto et. al. [41].

A better estimative of the apparent volume of a solute atom in a solid solution may be obtained by extrapolating experimental data to the solute axis the plot of the mean volume per atom within the phase of interest. The Figure 3.4 shows an example for simple binaries case, where the atomic volume of Cr, Mn, Fe, and Co in an FCC solid solution with Nickel is estimated. Extending this approach to the case of HEA is possible, but it poses some challenges due to the limited availability of lattice parameter data for concentrated alloys. Nonetheless, with further data collection and analysis, this approach can be adapted to suit the specific characteristics of HEAs.

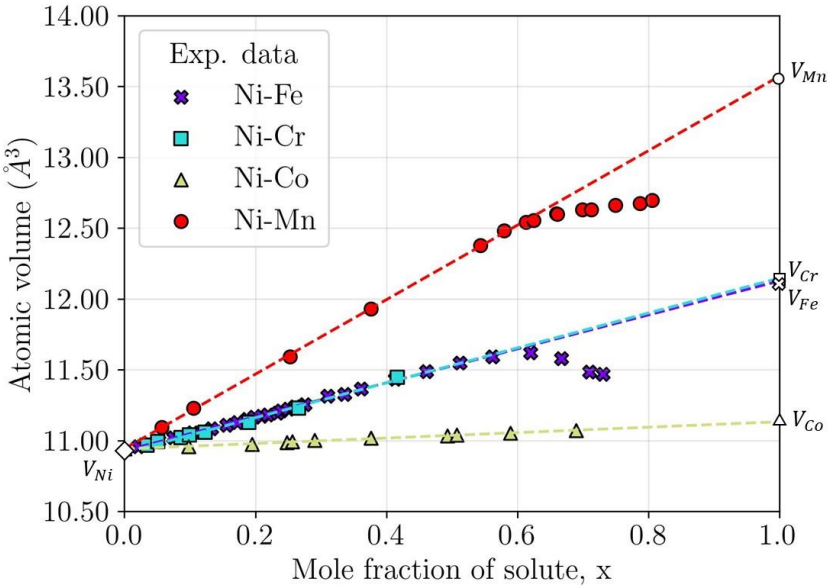

Figure 3.4: Average atomic volume of FCC alloys as a function of solute concentration for different species in solution with Ni. Experimental data were acquired at room temperature, and they were extracted from reference [42].

Assuming that Varvenne's model is accurate, Coury et al. [43] extracted the solid solution hardening component values of several high entropy alloys and employed them to determine the atomic radius of the constituent elements in the solid solution through a nonlinear least squares method. This method was named

Effective Atomic Radii for Strength (EARS). For the Cr-Mn-Fe-Co-Ni system, the EARS methodology proved promising, leading to the development of new alloys with the optimized solid solution hardening component.

Recently, the Varvenne's model was reassessed [44] for accounting elastic anisotropy in the solute-dislocation interaction in FCC solid solution alloys. Although the results calculated using this new model is argued be more accurate, the investigation showed that the isotropic model represents the full anisotropic results within a few percent.

3.3 Precipitation Hardening in FCC/$L1_2$ Alloys

Nanometric obstacles, mainly in the form of precipitates, distributed homogeneously in the matrix of a metallic alloy, can interact with the dislocations and act as effective barriers to the slip of these linear defects, significantly increasing the yield stress of a material [38].

Throughout this section the main concepts, models and simplifications assumed in the development of precipitation hardening models are discussed, with a major focus on alloys with A1/FCC (γ) matrix and $L1_2$ (γ') precipitates.

3.3.1 Introduction to precipitation-hardening modeling

Before starting the review of precipitation hardening, it is important to define certain parameters that assist in interpreting the mechanism of precipitation hardening and in developing mathematical models that estimate the strength contribution of this mechanism to an alloy's yield strength.

Precipitates are particles that typically exhibit a range of sizes and are commonly dispersed homogeneously throughout the material. Additionally, they often have a non-spherical shape. These facts can introduce significant complexities into the mathematical treatment of precipitation hardening [45]. Consequently, some simplifications are necessary to make the problem tractable. In alloys with FCC matrix and nanometric $L1_2$ precipitates, which are the focus of this work, the particles are typically spherical, simplifying the analysis. Therefore, this thesis will not address the issue of non-spherical precipitates any further.

The distribution of precipitate sizes during the coarsening stage has been a subject of debate in the literature, with several theories proposed [46–50], but no clear consensus has been reached. To address this issue, one potential approach is to treat the precipitates in a material as a monodisperse system of spheres, with each having the same radius, denoted by r_0. This radius is taken to be equal to the average radius of particles in the actual (polydisperse) system, denoted by $\langle r \rangle$. A schematic representation of this approach is shown in Figure 3.5.

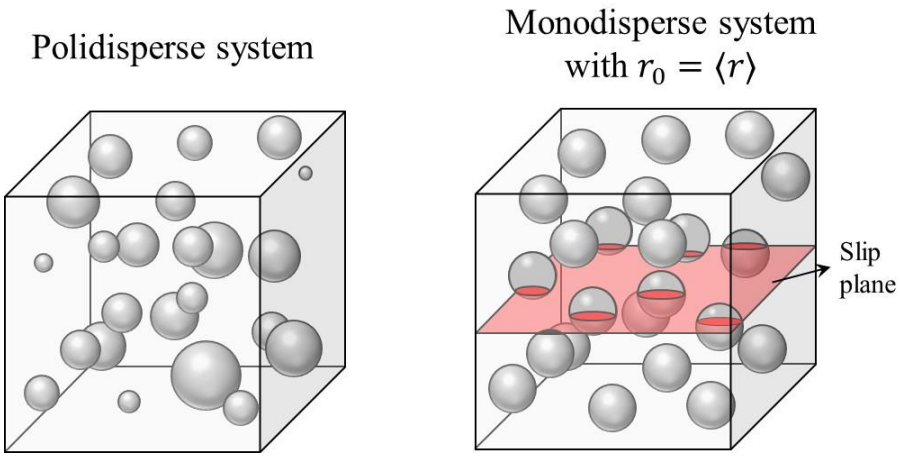

Figure 3.5: Schematic illustration of a polydisperse and a monodisperse systems of spheres.

As depicted in the drawing, even in this case, the dislocations may interact with various planar sections of the precipitates along their slip planes. A detailed schematic illustration of the dislocation-precipitate interaction is shown in Figure 3.6. In this drawing, the **planar** radius of a given obstacle is denoted by r_s, while the center-to-center distance between two obstacles in the plane is indicated by l. Additionally, the average segment length between two adjacent obstacles along the dislocation line is represented by λ.

Therefore, for the treatment of precipitation hardening, it is necessary to determine the average values of r_s, l, and λ. These values will be denoted as $\langle r_s \rangle$, $\langle l \rangle$ and $\langle \lambda \rangle$, respectively, in the subsequent analyses.

The expected planar radius of a precipitate of spatial radius r_0 can be easily calculated through geometric probability principles and it is given by Equation 3.5 [51,52].

$$\langle r_s \rangle = \frac{\pi}{4} r_0 \tag{3.5}$$

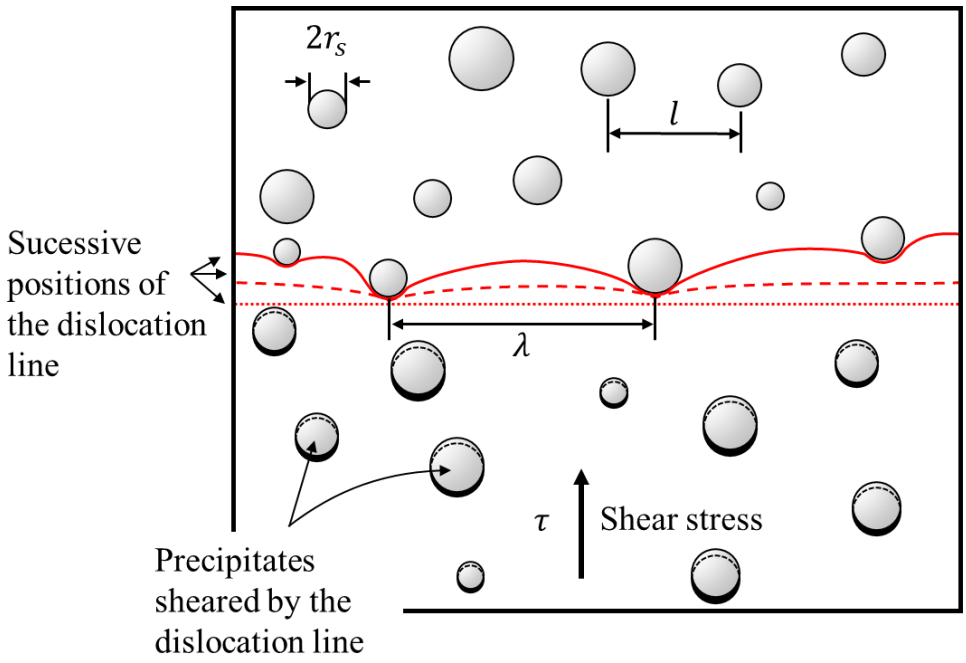

Legend:

$\boldsymbol{r_s}$**:** planar radius of a precipitate;

$\boldsymbol{l}$**:** center-to-center distance between two precipitates on the slip plane;

$\boldsymbol{\lambda}$**:** center-to-center distance between two adjacent precipitates along the dislocation line.

Figure 3.6: Schematic illustration of precipitates-dislocation interaction on the slip plane.

For the sake of comparison, the expected planar radius of precipitates that follow the Lifshitz-Slyozov-Wagner (LSW) size distribution is given by $\langle r_s \rangle = 0.82\langle r \rangle$ [53]. Since most precipitation hardening equations exhibit a square root

dependence on $\langle r_s \rangle$, the assumption of a monodisperse system does not introduce significant errors in the results.

To estimate the average spacing among the precipitates in the slip plane, $\langle l \rangle$, a common method is to assume that the particles are arranged in a simple square lattice. In this case, the average spacing between the particles is equal to the length of the lattice and is denoted by $l_{sq.}$,

$$\langle l \rangle \approx l_{sq.} = \frac{1}{\sqrt{N_A}} = r_0 \sqrt{\frac{2\pi}{3f}} \tag{3.6}$$

where N_A is the number of particles per unit area and f is the volume fraction of precipitates in the alloy. Several other parameters have been proposed in the literature to estimate $\langle l \rangle$. In general, they are in the range of $0.75 l_{sq.} \leq \langle l \rangle \leq 1.25 l_{sq.}$. Given the simplicity for calculating $l_{sq.}$, this parameter is usually assumed as the average spacing among the precipitates in most precipitation hardening models. It should be noted that $\langle l \rangle$ is different from the average spacing between adjacent obstacles along the dislocation line, $\langle \lambda \rangle$, which will be discussed in detail later in this text.

3.3.2 Force balance between dislocation and precipitate

When a shear stress is applied to a material, exerting a force per unit length (τb) on a dislocation line, it advances, make contact with obstacles, and start to bend between them in its slip plane. If these obstacles are coherent precipitates and the work applied exceeds the energetic barrier offered by the precipitate field, the dislocation shears the particle [38,52].

A balance between the resistive force of an obstacle (F) and the dislocation line tension Γ, as shown in Figure 3.7, yields the first relationship in Equation 3.7. Additionally, considering that the average distance between the neighboring precipitates along the discordance line is $\langle \lambda \rangle$, the total force acting on this average segment, $\tau b \langle \lambda_c \rangle$, can be transferred to the central obstacle, leading to the second relationship presented in Equation 3.7.

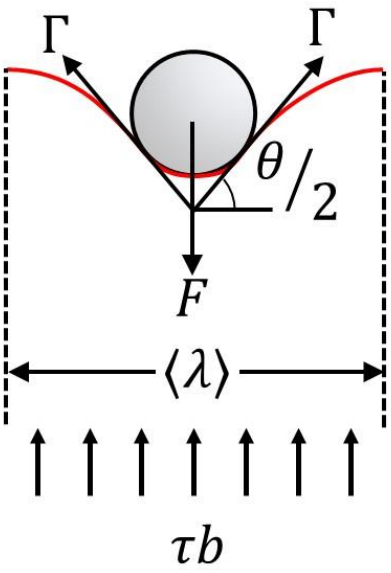

Figure 3.7: Schematic drawing of dislocation-precipitation force balance.

$$\begin{cases} 2\Gamma \sin(\theta/2) = \mathrm{F} \\ \tau b\langle\lambda\rangle = F \end{cases} \tag{3.7}$$

where $\theta/2$ is the dislocation bow-out angle. Solving the system for τ, results in Equation 3.8.

$$\tau = \frac{2\Gamma}{b\langle\lambda\rangle}\left(\frac{F}{2\Gamma}\right) \tag{3.8}$$

In the case of incoherent particles or particles with a high resistive force, so that dislocations cannot shear them (impenetrable particles), this linear defect bypasses the obstacles, leaving a dislocation ring around them. This mode of interaction is known as the Orowan mechanism [38], and it is represented schematically in Figure 3.8. In this drawing the successive dislocation configuration is indicated by the numbers from 1 to 5.

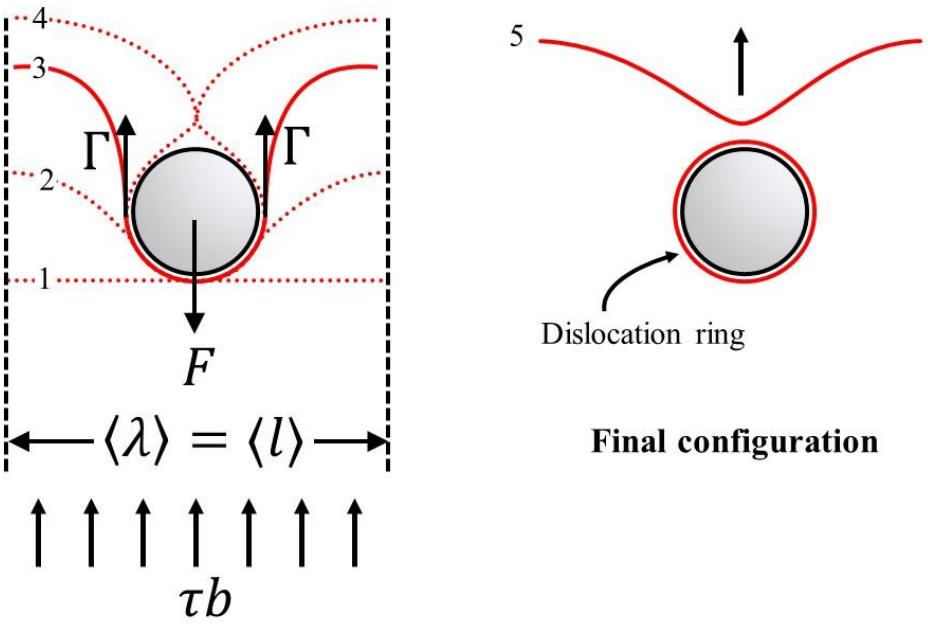

Figure 3.8: Schematic drawing of the dislocation-precipitation interaction for the case of impenetrable particles.

At the critical configuration, represented by the number 3, the shear stress can be estimated by Equation 3.8, where $^{F}/_{2\Gamma} = 1$ and $\langle\lambda\rangle$ is replaced the mean free path among the particles $\langle l\rangle - 2\langle r_s\rangle$ [51], as will be discussed in the next section. From these considerations, Equation 3.9 is obtained,

$$\tau_c^{Orowan} = \frac{2\Gamma}{b(\langle l\rangle - 2\langle r_s\rangle)} \tag{3.9}$$

When the distance between the precipitates is much larger than the radius of the particles, which is observed for $f \to 0$, it turns out that $\langle l\rangle - 2\langle r_s\rangle \approx \langle l\rangle$. Therefore, the denominator of Equation 3.9 becomes $b\langle l\rangle$. As can be seen from previous equation, once the Orowan mechanism becomes the dominant mechanism, the radius and the volume fraction of particles that controls the precipitation hardening contribution to yield strength.

Better predictions for τ_c^{Orowan} can be obtained by considering the interaction between the adjacent arms of the dislocation when bypassing the particles, which results in a decrease in the line tension and hence the value of τ_c^{Orowan}. Since the peak stress in alloys hardened by ordered particles is not

achieved by the intersection between shear and Orowan mechanism, further details are not discussed in this work.

3.3.3 Spacing between adjacent precipitates along the dislocation line

As the shear stress increases, the dislocation line tends to bend more between two adjacent precipitates, which increases the probability of the dislocation encountering a new precipitate. Consequently, the average center-to-center spacing between adjacent precipitates along the dislocation line, ⟨λ⟩, may change as a function of τ and/or F. This was schematically illustrated in Figure 3.6.

Therefore, one of the major challenges in modeling the precipitation hardening component is to establish the correlation between the shear stress at the critical moment (τ_c), the maximum precipitate resistive force (F_m), and the average distance between the precipitates along the dislocation line at that moment $\langle\lambda_c\rangle$. The critical moment refers the condition for the dislocation to break free of the obstacles. In the field of precipitation hardening, two theories are proposed for estimating this correlation, which are presented below:

- *Fleisher-Friedel theory*

A theory to try to solve this problem was proposed independently by Friedel and by Fleisher and Hibbard [38]. The main premises of this theory are [52]:

i. Precipitates are point defects;
ii. The precipitates can be considered arranged in a simple square lattice;
iii. All precipitates have the same resistive force;

In their approaches, the way the dislocation bends between precipitates is idealized as an arc of a circle, and as soon as the dislocation shears a precipitate, it sweeps an area that contains, on average, one obstacle, in a stationary process of dislocation-precipitate anchoring and unanchoring. Thus, the area swept by the dislocation after shearing the precipitates (S_{FF}) times the number of particles per unit area (N_A) is equivalent to unity, which is translated into Equation 3.10.

$$S_{FF} \cdot N_A = 1 \tag{3.10}$$

Starting from Equation 3.10, by means of elementary geometric considerations and the mathematical approximation $\sin x \approx x$ for values of *x* close to zero, the value of λ_c is possible to be determined by Equation 3.11.

$$\lambda_c^{FF} = \left(\frac{2\Gamma}{\tau_c b N_A}\right)^{\frac{1}{3}} \tag{3.11}$$

where $N_A^{-1/2} = l_{sq.}$ and the superscript FF is inserted to identify that this is the spacing obtained by Fleisher-Friedel theory. Substituting λ_c^{FF} into the relations presented in Equation 3.8 and by simple algebraic manipulations establish the relations presented in Equations 3.12 and 3.13.

$$\tau_c^{FF} = \left(\frac{F_m}{2\Gamma}\right)^{\frac{3}{2}} \frac{2\Gamma}{b l_{sq.}} \tag{3.12}$$

$$\lambda_c^{FF} = \frac{l_{sq.}}{\left(F_m/2\Gamma\right)^{1/2}} \tag{3.13}$$

where F_m is the maximum resistive force of the obstacle.

Therefore, for shear stresses greater than τ_c^{FF}, the movement of the dislocations is no longer hindered by the precipitates in the slip plane and can be considered the precipitation-hardening contribution to yield strength. The term in parentheses in Equations 3.12 and 3.13 is called hereafter as specific strength and, as can be observed from relation 3.7, it ranges from 0 to 1. Equation 3.13 also shows that as the specific resistance of obstacles increases, the critical spacing between obstacles along the dislocation line decreases. This spacing can reach a minimum value of $l_{sq.}$, when $F_m/2\Gamma = 1$. In addition, when the specific strength of precipitates exceeds one, dislocations are no longer able to shear them, and instead, the precipitates are bypassed, as shown in Figure 3.8.

- *Computational simulations*

Since the precipitates are not arranged in a periodic manner, a "random" arrangement of the particles would be more suitable to represent a real system.

Studies with this approach, maintaining the condition of point obstacles, were performed by graphical methods [33], computer simulations [34], and analytically [35]. The results showed that indeed there is a well-defined stress at which the dislocations can move over long distances through the crystal without being hindered by the obstacles. Furthermore, these studies showed that the Fleisher-Friedel relation proves to be a very good approximation when the obstacles are relatively weak (specific resistance $\lesssim 0.4$). However, as $F_m/2\Gamma$ increases, the dislocation advances by finding paths of easier motion, where the spacing between obstacles along the dislocation line is greater than λ_c^{FF}. Consequently, the value of the critical shear stress (τ_c) falls below the prediction established by the Friedel-Fleisher relation, as shown in the results in Figure 3.9.

By an empirical fitting of simulation data, Ardell [51] proposed the Equation 3.14 to represent the precipitation hardening contribution to yield stress over the whole range of precipitates specific strength.

$$\tau = 0.956\left(\frac{2\Gamma}{b\langle l\rangle}\right)\left(\frac{F_m}{2\Gamma}\right)^{3/2}\left[1-\frac{\left(F_m/2\Gamma\right)^2}{8}\right] \tag{3.14}$$

As can be seen in Figure 3.9, the simulation results predict a normalized critical shear stress for $F_m/2\Gamma = 1$ between 0.81 and 0.84. Commonly in the literature, therefore, Equation 3.9 is reported multiplied by a factor between 0.81 and 0.84 [51]. These works also reveals that $\langle\lambda_c\rangle$ for a random configuration of obstacles with specific strength equals unity is given by $\langle\lambda_c\rangle = l_{sq.}/0.81$, which can be easily derived taking into consideration Equation 2.8.

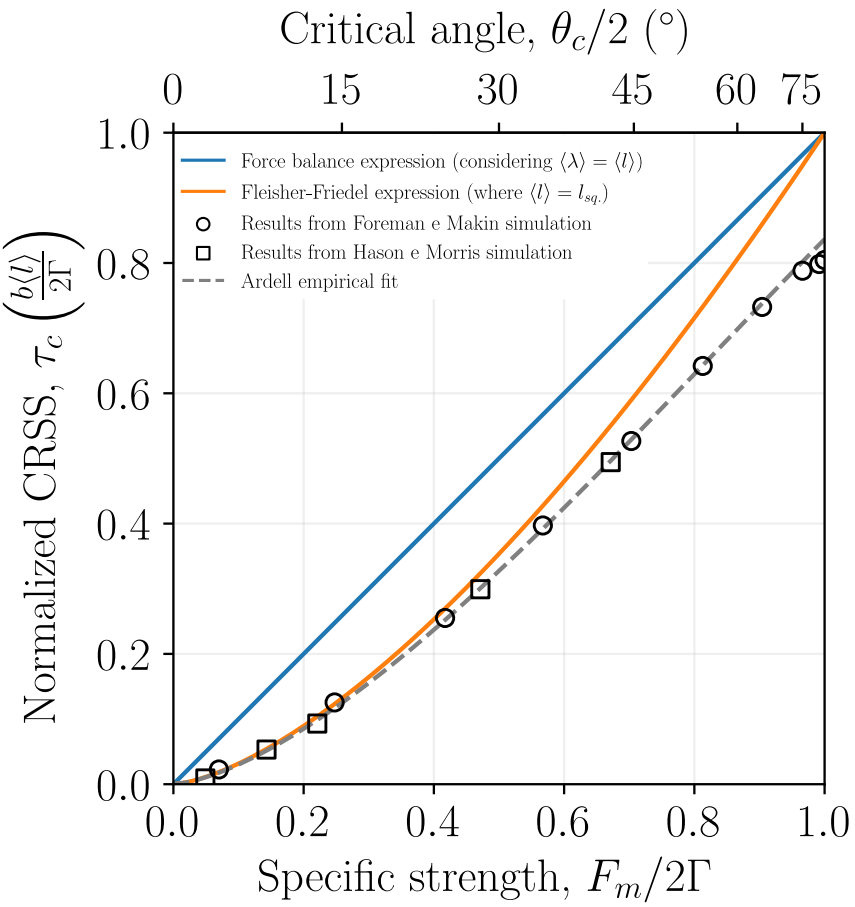

Figure 3.9: Normalized critical shear stress estimated by Fleisher-Friedel theory and computer simulation results from Foreman e Makin, and Hason e Morris.

3.3.4 Precipitate shearing resistance

There are five main mechanisms that contribute to the shearing resistance of coherent/semi-coherent precipitates by dislocation lines, controlling F_m and, consequently, hindering the motion of a dislocation [38,45,51,52].

- **Chemical hardening:** when a dislocation shears a precipitate, a new matrix/precipitate interface is created. Theoretical models indicate that the creation of this interface decrease the precipitation hardening contribution as the radius of the precipitates increases, i.e., $\tau_c^{Chem.} \propto {\chi_s}^{3/2} f^{1/2} r_0^{-1}$, where χ_s is the interfacial energy between precipitate and matrix phase. Since, in practice, the increase of the precipitates size tends to increase the mechanical strength of an alloy, it is assumed that this mechanism exerts little influence on precipitation hardening;

- **Coherency hardening:** a precipitate with a lattice parameter different from the matrix causes a local distortion in the matrix lattice, producing a dilatational stress that interacts elastically with the dilatational components of the dislocation stress field, hindering the dislocation motion;
- **Modulus hardening:** the line energy of a dislocation is different within the precipitates and in the matrix. Consequently, the dislocation line is locally attracted or repelled by the precipitate;
- **Stacking-fault strengthening** in FCC alloys containing FCC precipitates, a significant difference between the stacking fault energy of the precipitate and the matrix can hinder the movement of dislocations. When the stacking fault energy is greater in the precipitate than in the matrix, penetration of a dislocation into the precipitate increases the line energy locally, so that repulsive interactions develop in contact with the precipitate. On the other hand, if the stacking fault energy is lower in the precipitate, the dislocation is attracted towards the center of the precipitate;
- **Order strengthening:** an interfacial defect called antiphase boundary, with energy per unit area χ_{APB}, is created when ordered particles is sheared by a matrix dislocation. The creation of this defect offers a resistance to the movement of the dislocations due to the increase of the energy of the system. Since in this work the development of alloys hardened by ordered particles is carried out, this last hardening mechanism is further detailed throughout this section.

It is noteworthy that in alloys with FCC/$L1_2$ microstructure, lattice misfit is generally small, in the order of ~ 0.01 [52,54]. Therefore, for these alloys the contribution of coherency hardening is argued to be negligible. The modulus difference between these phases is also of small magnitude, being less than 0.05 in Ni-Al system in a wide temperature range [55]. Therefore, the contribution of modulus hardening is also often neglected.

Unlike alloys hardened by non-ordered precipitates, dislocation moves in groups of two or more dislocations in alloys hardened by ordered particles [56–61]. The number of dislocations in the group depends on how many dislocations

are needed to restore the long-range order in the precipitate after the precipitate is sheared by the first dislocation in the group [45]. In the case of alloys with FCC matrix and $L1_2$ precipitates, the dislocations move in pair along the slip planes. Since this microstructure is the focus of the present work, only the interaction mechanisms related only to this type of microstructure is detailed below.

The first dislocation of the pair, which is referred herein as D1, creates an antiphase boundary in the {111} plane of the $L1_2$ phase after its passage. This first dislocation experiences a repulsive force to its motion, due to the creation of the antiphase boundary within the precipitate. The trailing dislocation, named as D2 throughout the text, experience the influence of an attractive force, associated with the restoration of order within the $L1_2$ precipitates. These repulsive and attractive forces are translated into Equation 3.15.

$$|F| = \chi_{APB}\xi \tag{3.15}$$

where ξ is the length of dislocation within the precipitate, which range from zero to $2r_s$, and χ_{APB} is the antiphase boundary energy (APB) of (hkl) crystallographic planes. For a spherical precipitate of spatial radius r_0, therefore, the maximum force of attraction/repulsion is given by $|F_{max}| = 2r_s\chi_{APB}$.

Upon application of a shear stress, in addition to the forces due to resistance/attraction associated with the antiphase boundary creation/annihilation, both dislocations also experience a mutual repulsion force per unit length (F_R). By means of a force balance performed under each dislocation in the pair it is possible to establish the system given in equation 3.16.

$$\begin{cases} \boldsymbol{D1}\text{: } \tau b\langle\lambda_1\rangle + F_R\langle\lambda_1\rangle - \chi_{APB}\langle\xi_1\rangle = 0 \\ \boldsymbol{D2}\text{: } \tau b\langle\lambda_2\rangle - F_R\langle\lambda_2\rangle + \chi_{APB}\langle\xi_2\rangle = 0 \end{cases} \tag{3.16}$$

where $\langle\lambda_1\rangle$ and $\langle\lambda_2\rangle$ are the average spacing between precipitates along D1 and D2, respectively. The variables $\langle\xi_1\rangle$ and $\langle\xi_2\rangle$ are the average length of dislocation line within the precipitates along D1 and D2, respectively. Solving the previous system for τ, lead to Equation 3.17.

$$\tau = \frac{\chi_{APB}}{2b}\left(\frac{\langle\xi_1\rangle}{\langle\lambda_1\rangle} - \frac{\langle\xi_2\rangle}{\langle\lambda_2\rangle}\right) \tag{3.17}$$

3.3.4.1. Underaged condition - Weak pair coupling

At the beginning of aging, when the precipitates are very small and numerous, the average distance $\langle w \rangle$ between D1 and D2 is relatively large with respect to the particle size. Thus, the dislocations are unlike to reside within the same precipitate and the dislocation pair is said to be weakly coupled. Moreover, since the resistive force of a precipitate is proportional to the particle size (Equation 3.15), it follows that the precipitate resistance is relatively low under this condition and, consequently, the dislocation bows out slightly between the particles. The motion of the pair of dislocations in the slip plane is represented schematically according to Figure 3.10.

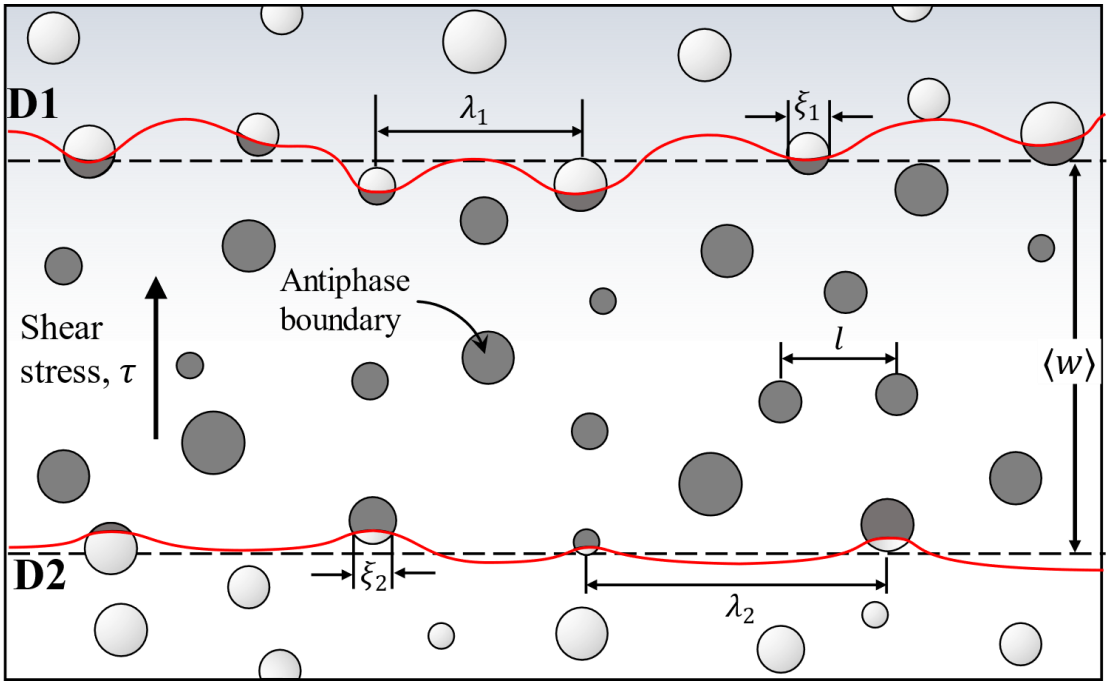

Figure 3.10: Schematic illustration of the motion dislocation pair D1/D2 in the slip plane of an alloy with microstructure FCC/L12 on the weak pair coupling regime.

For alloys with a low volume fraction of ordered precipitates, where the Fleisher-Friedel statistics is a reasonable approximation, Brown and Ham approximated $\langle \lambda_1 \rangle$ at the critical moment by λ_c^{FF}. Furthermore, they considered that D2 advances roughly as a straight line. Consequently, $\langle \xi_2 \rangle / \langle \lambda_2 \rangle$ was taken as the volume fraction of precipitates in the alloy, f. From these considerations, making appropriate substitutions in the Equation 3.17, the critical shear stress can be estimated by Equation 3.18 [29].

$$\tau_c = \frac{\chi_{APB}}{2b}\left[\left(\frac{3\pi^2}{32}\frac{\chi_{APB} f r_0}{\Gamma}\right)^{\frac{1}{2}} - f\right]. \quad (3.18)$$

Ardell [62] extended the Fleisher-Friedel theory to finite obstacles, based purely on the geometry of the dislocation-precipitate interaction, resulting in Equation 3.19. This model is argued to be applicable for alloys with volume fractions of precipitates up to 0.4.

$$\tau_c = \frac{\chi_{APB}}{2b}(u - f),$$
$$u = \frac{-3B \pm \sqrt{3B^2 + 36B}}{6 - B}, \quad (3.19)$$
$$B = \frac{3\pi^2}{32}\frac{\chi_{APB} f r_0}{\Gamma}.$$

Another interpretation of trailing dislocation configuration is that it is completely pulled through the faulted precipitates once the dislocation interacts with them [45]. According to this definition, $\langle \xi_2 \rangle$ equals zero and the right-side term in parenthesis in Equations 3.18 and 3.19 vanishes. However, there is no conclusive experimental evidence for either of the two proposed configurations in the literature, and this remains an open topic of investigation.

Other models have been proposed to describe the contribution of ordered precipitates to the yield stress under the weak-couple regime [52,62,63], but they are not detailed here. In general, they follow equations of the type shown in 3.20:

$$\tau_c = \frac{\chi_{APB}}{2b}\left[A_1\left(\frac{\chi_{APB} f r_0}{\Gamma}\right)^{\frac{1}{2}} + A_2 f\right] \quad (3.20)$$

where A_1 e A_2 are constants that depends on simplifications assumed to solve the Equation 3.17.

As can be seen in the previous equations, the critical shear stress in the underaged condition increases as the size of the precipitates increases for a fixed volume fraction of precipitates.

3.3.4.2. Overaged condition - Strong pair coupling

As aging proceeds, the precipitates coarsen and the spacing between the dislocations become comparable to the size of the precipitates. Once the average distance between the dislocations in the pair is smaller than the mean planar diameter of the precipitates ($\langle w \rangle < 2\langle r_s \rangle$), D2 starts to penetrate the precipitate and remove the antiphase boundary created by D1 before D1 leaves the particle.

From a given precipitate size, the distance between the dislocations in the pair becomes smaller than the average planar radius of the precipitates ($\langle w \rangle < \langle r_s \rangle$). From this moment on, D1 has its motion no longer hindered by the maximum resistive force of a precipitate. Figure 3.11 illustrates the different force profiles of the dislocations-precipitate interaction for different values of $\langle w \rangle / \langle r_s \rangle$. As can be seen, for values of $\langle w \rangle > \langle r_s \rangle$, D1 has its motion hindered by the maximum resistive force that the precipitate can offer before the trailing dislocation starts to enter the particle. However, for distances $\langle w \rangle < \langle r_s \rangle$, the maximum resistance force offered by the ordered particles decays monotonically as $\langle w \rangle / \langle r_s \rangle$ decreases. Furthermore, in this case the point of maximum resistive force is always the one at which D2 starts to penetrate the precipitate [64].

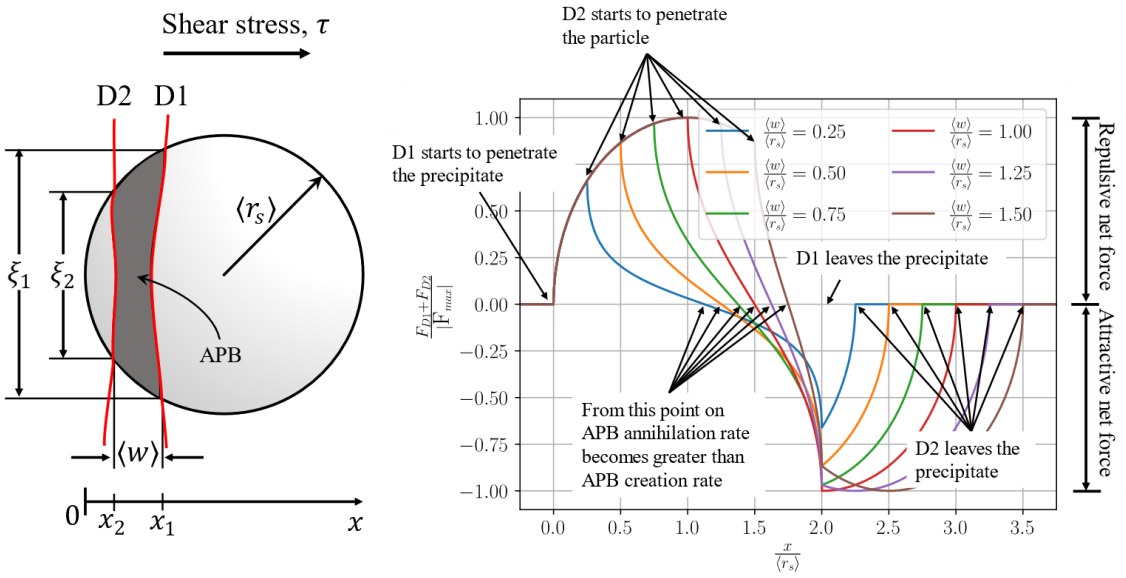

Figure 3.11: Profiles of normalized net force versus normalized distance of the pair of D1/D2 dislocations shearing an ordered spherical particle of $L1_2$, assuming that the average distance between the dislocation is given by $\langle w \rangle$.

The regime in which $\langle w \rangle < \langle r_s \rangle$ is referred to in the literature as strong pair coupling. Figure 3.12 presents a schematic drawing of the dislocation-precipitate interaction at the critical shear stress condition under this regime. Assuming $\langle \lambda_1 \rangle = \langle \lambda_2 \rangle = l_{sq.}$, considering $\langle w \rangle$ equivalent to the equilibrium distance between two edge dislocations of the same sign, and by simplifications and manipulations Equations 3.17, the critical shear stress for the cases where $\langle w \rangle < \langle r_s \rangle$ can be estimated by

$$\tau_c = \left(\frac{3}{2\pi}\right)^{\frac{1}{2}} \frac{k}{\pi} \frac{Gbf^{\frac{1}{2}}}{r_0} \left(\frac{\pi^2}{2k} \frac{\chi_{APB} r_0}{Gb^2} - 1\right)^{\frac{1}{2}} \tag{3.21}$$

where k is an adjustable parameter related to the elastic repulsion between the dislocations within the precipitate, being of the order of unity [64].

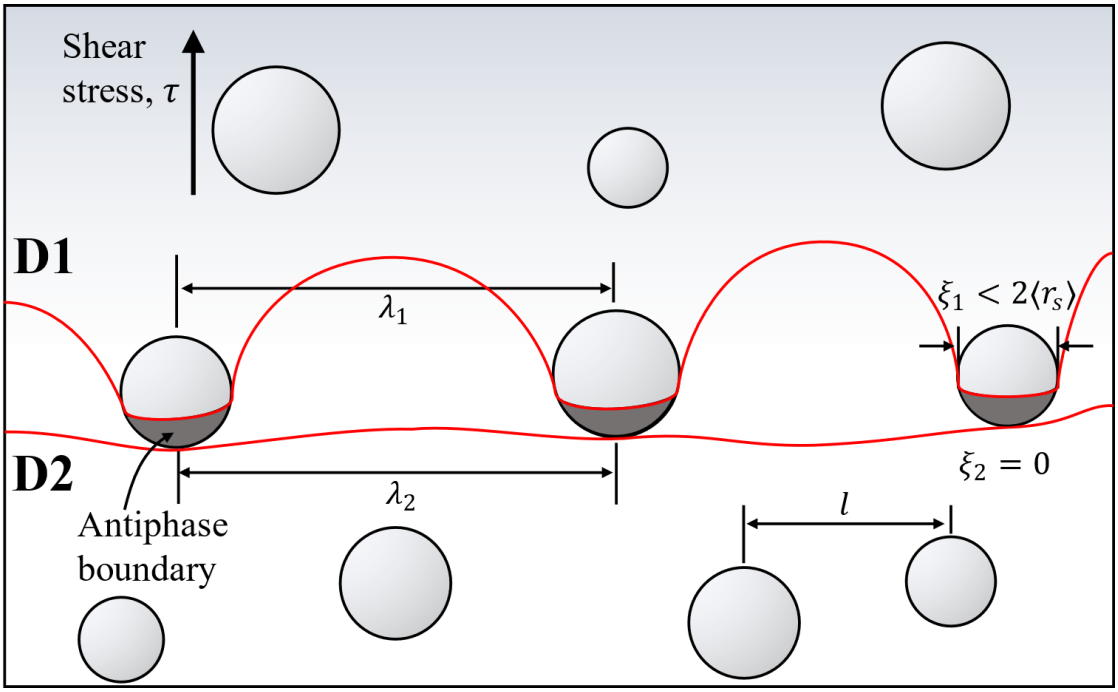

Figure 3.12: Schematic drawing of the precipitate-dislocation interaction at the critical shear stress in the strong-couple regime.

As can be seen from Equation 3.21, under the strong pair coupling regime the contribution to yield stress due to ordered particles decrease as the size of the precipitates increases. Like the case of weak-pair coupling, other models have been proposed in the literature to estimate the critical shear stress of over-aged alloys [38,62,63,65].

3.3.4.3. Peak aged condition

In alloys hardened by ordered particles, the peak stress is not attributed to the transition from the particle shearing mechanism to the Orowan mechanism, as occurs in the other precipitation hardening cases. Rather, it occurs in a transition region between the weak coupling and strong coupling regimes.

At peak aging condition, $\langle \lambda_1 \rangle$ reaches its minimum value. According to Fleisher-Friedel theory, under this condition $\langle \lambda_1 \rangle$ is given by $l_{sq.}$. On the other hand, computational simulation by Foreman and Makin suggests that $\langle \lambda_1 \rangle$ is given by $l_{sq.}/0.81$. It should be noted that theses approximations are only valid for highly dispersed precipitates, where the point obstacle assumption is reasonable. As discussed previously, the maximum force offered by a single particle occurs when

the dislocation length within the precipitate ($\langle\xi_1\rangle$) equals $2\langle r_s\rangle$. Furthermore, at the critical moment D2 is about to enter the precipitate, hence $\langle\xi_2\rangle = 0$. Substituting these values in Equation 3.17 yields the result,

$$\tau_c = 0.81\frac{\chi_{APB}}{2b}\sqrt{\frac{3\pi f}{8}}. \tag{3.22}$$

As argued by Ardell [45], the previous equation is not particularly accurate for predicting quantitatively the peak strength of most alloys. One possible reason suggested by this author is the influence of finite particle size in the precipitate-dislocation interaction, which is not taken into account in the previous derivation.

3.4 Antiphase Boundary in $L1_2$ Structure

As shown in the previous chapter, the resistive force of an isolated $L1_2$ precipitate is directly proportional to the antiphase boundary energy in the {111} planes of the ordered phase. Furthermore, the superior high temperature strength of alloys with FCC matrix and $L1_2$ precipitates is attributed to the anomalous flow stress behavior which is associated with a complex movement and interaction of the dislocations in the ordered $L1_2$ phase, involving Kear-Wilsdorf locks [64]. Therefore, an understanding of this parameter is paramount for the development of new alloys with optimized mechanical properties. However, despite its importance, most of the available experimental and computational data on the effect of composition on APB energy are limited to binary or ternary alloys, and only a very few works attempted to estimate the APB energy in a multicomponent $L1_2$ phase.

3.4.1 Description of $L1_2$ structure and fault energies

A schematic illustration of unit cell of $L1_2$ structure (A_3B) is shown in Figure 3.13a. This structure has a primitive cubic lattice with four atoms per lattice point, and its space group is $\mathrm{Pm\bar{3}m}$. This structure is better described using sublattice concept. Either two sublattices or four sublattices may be assigned to $L1_2$ structure, as shown in Figure 3.13b. In this work, the former definition is used since it is crystallographic accurate. Furthermore, most nickel-superalloys, which

are composed mainly of a FCC matrix and $L1_2$ precipitates, have the Ni_3Al as the prototype structure for $L1_2$ phase, hereafter the sublattice I is named Al-sublattice, whereas sublattice II is called the Nickel-sublattice.

Figure 3.13c presents the consecutively stacking of three packed atomic planes in $L1_2$ structure along [111] direction. As can be seen, an atom occupying atomic site B has as first nearest neighbors (FNN) only atoms occupying atomic site A (see the neighboring atomic sites of the circle indicated by the number 1). On the other hand, atoms in atomic site B have four atoms that occupy the atomic site B and 8 atoms occupying the atomic site A as FNN (see the neighboring atomic sites of the circle indicated by the number 2).

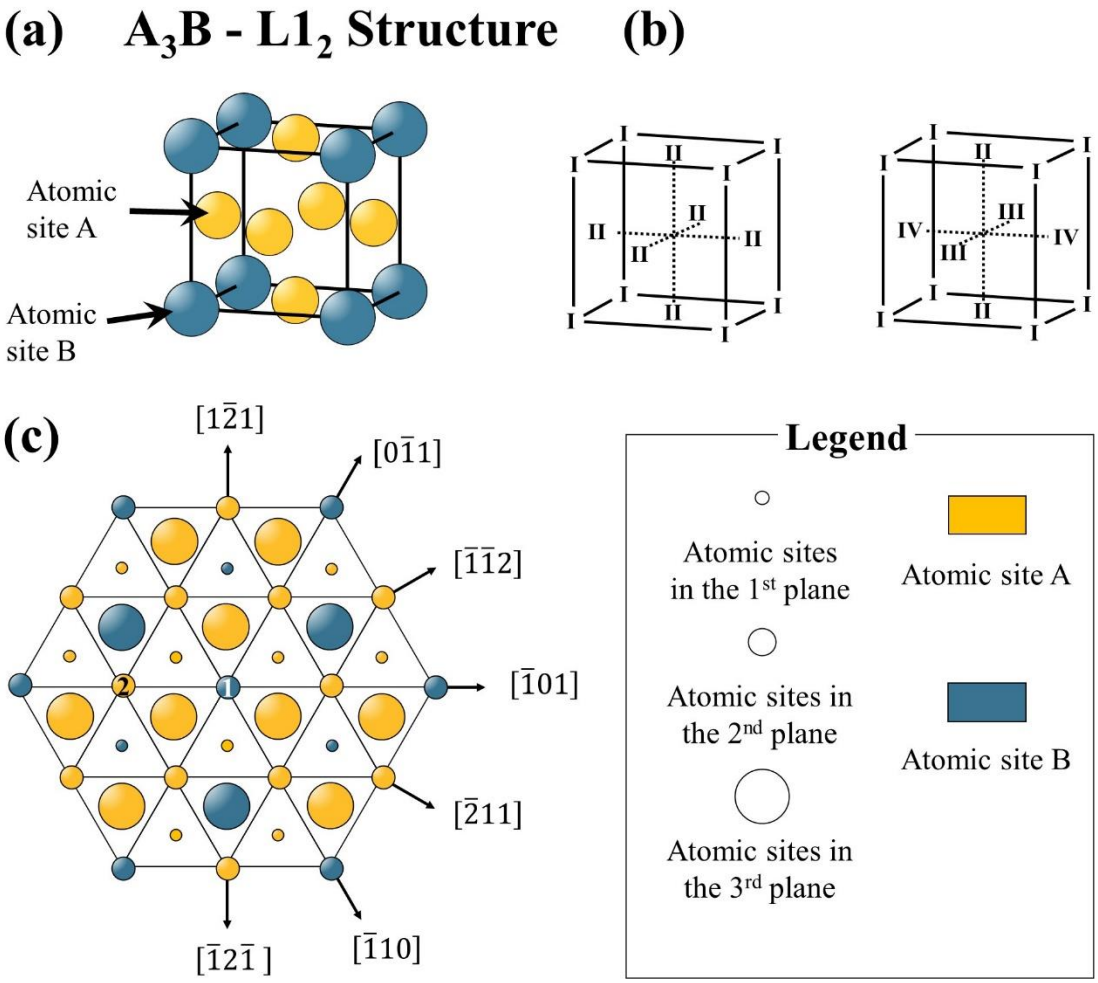

Figure 3.13: Schematic illustration of a) $L1_2$ structure; b) sublattice definitions for $L1_2$ structure, and c) staking sequence of (111) type of planes in $L1_2$ structure.

Note that a perfect dislocation Burgers vectors in the FCC matrix is not a lattice vector in $L1_2$ structure. Thus, the shearing of the ordered precipitate by a matrix dislocation creates an APB. The creation of the fault does not change the stacking sequence but change the bonding environment. A schematic illustration of the configuration of the atoms in the (111) planes prior and after the passage of a matrix dislocation with a Burgers vector $a/2[\bar{1}01]$ is shown in Figure 3.14. As can be seen, “forbidden bonds” are created upon shearing, illustrated by the dashed lines.

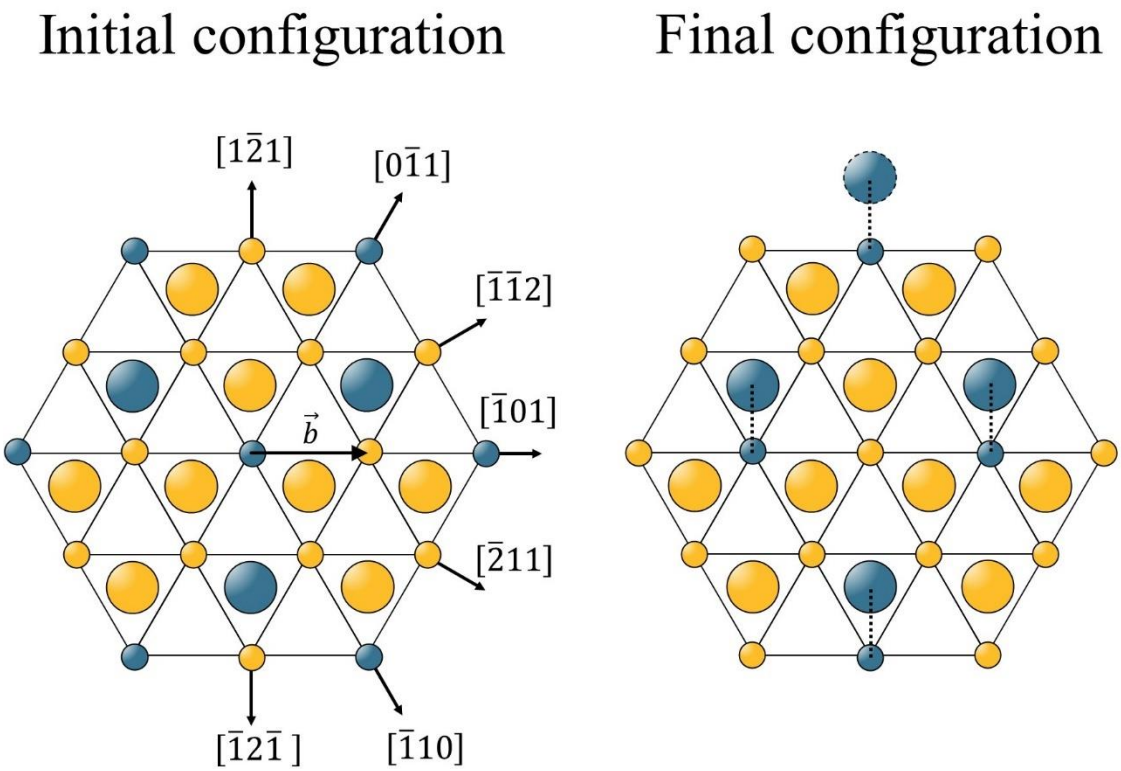

Figure 3.14: Schematic drawing of APB formation on (111) type of plane upon shearing of $L1_2$ structure by an FCC perfect dislocation.

The understanding of how the composition affect the fault energy, however, is challenging. Once this is rationalized, strategies for adjusting the relative fractions of the alloying elements in the A_3B structure, seeking a maximization of APB energy, may be developed. Basically, three points need to be addressed for χ_{APB} optimization purposes.

- What is the composition of the $L1_2$ phase?

- Does a given atom have a preferential sublattice site? If so, what sublattice it tends to occupy?
- What is the effect of a given alloying element on APB energy?

The common experimental method to acquire information about chemical composition of $L1_2$ is through chemical composition of precipitates. Experimental techniques such as SEM-EDS or TEM-EDS are the usual method to get such information. Another experimental method is performing chemical analyses of precipitates extracted from aged samples. For design purposes, the $L1_2$ composition is often calculated by computational thermodynamics using CALPHAD method. The reliability of this methodology would depend on the accuracy of the utilized database. The two other questions are discussed in more detail in the following paragraphs.

3.4.2 Sublattice occupation

In the case of nickel-based superalloys, the $L1_2$ prototype structure is Ni_3Al. The addition of a third element X may occupy the Ni sublattice, the Al sublattice or have no preferential atomic site. The distribution of atoms in the sublattices can be predicted through the study of $L1_2$ solubility field in Ni-Al-X ternary phase diagrams, where X is a ternary addition. Ochiai et al. [66] published a compilation of the relevant parts of such phase diagrams in the range between 850 and 1060 °C, which is shown Figure 3.15. For example, for Cu, Co, and Pt elements, the $L1_2$ phase stability field tends to increase parallel to the Ni-X side of the ternary diagram, indicating that these elements tend to replace Ni in its sublattice. On the other hand, for Ti, V, Ta, Nb, Mo, W elements, the $L1_2$ phase stability field tends to increase parallel to the Al-X side of the ternary diagram, indicating that these elements tend to replace Al in its sublattice. For other elements such as Fe, Cr and Mn, they seem to have no preferential sublattice.

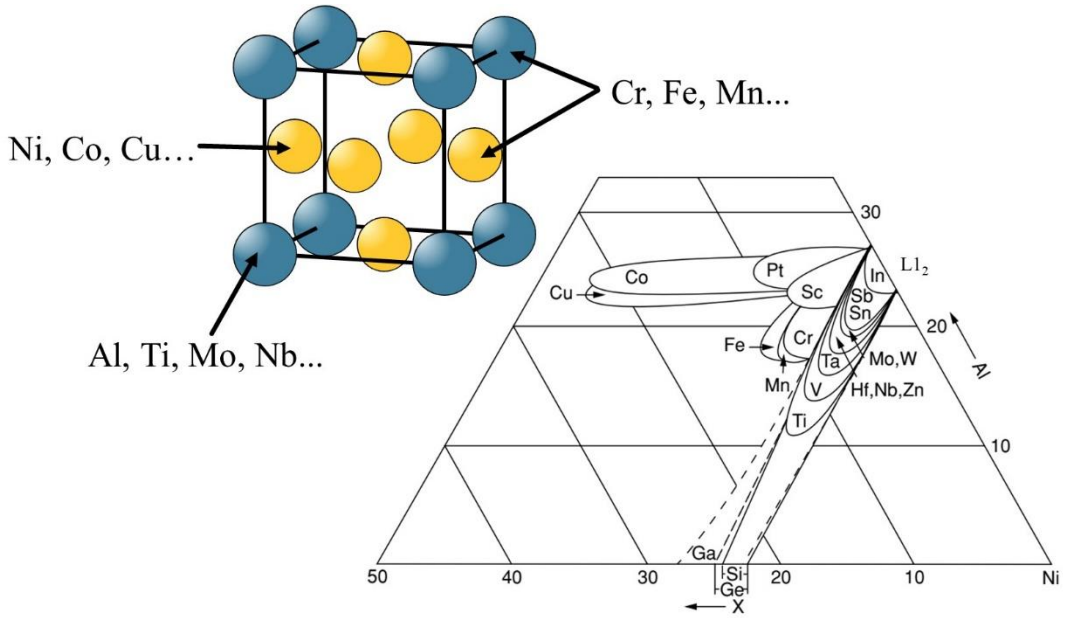

Figure 3.15: Solubility contour of $L1_2$ phase for different X metals in the Ni-Al-X systems. Figure adapted from reference [64].

In a recent work, Chen et. al [67] used DFT method to estimate the sublattice preference of several solutes when added to Ni_3Al structure. Their study considered a fixed concentration of 1 at.% of the ternary species and the temperature was fixed at T = 727 °C. The solute sublattice preference is summarized schematically in Figure 3.16.

As shown by this investigation, most elements in groups IX, X, and XI tend to occupy the Ni-sublattice. On the other hand, Fe, Ir, Zn, Cd, and Hg have a site preference that depends on the Al concentration in the $L1_2$ structure. For low Al concentration, these elements tend to partition to Al-sublattice, whereas, for a higher concentration of Al, they are likely to replace atoms in Ni-sublattice. The great majority of elements tend to occupy the Al-sublattice. The author argued that most elements replace Al due to the higher size of Al atoms compared to Ni atoms.

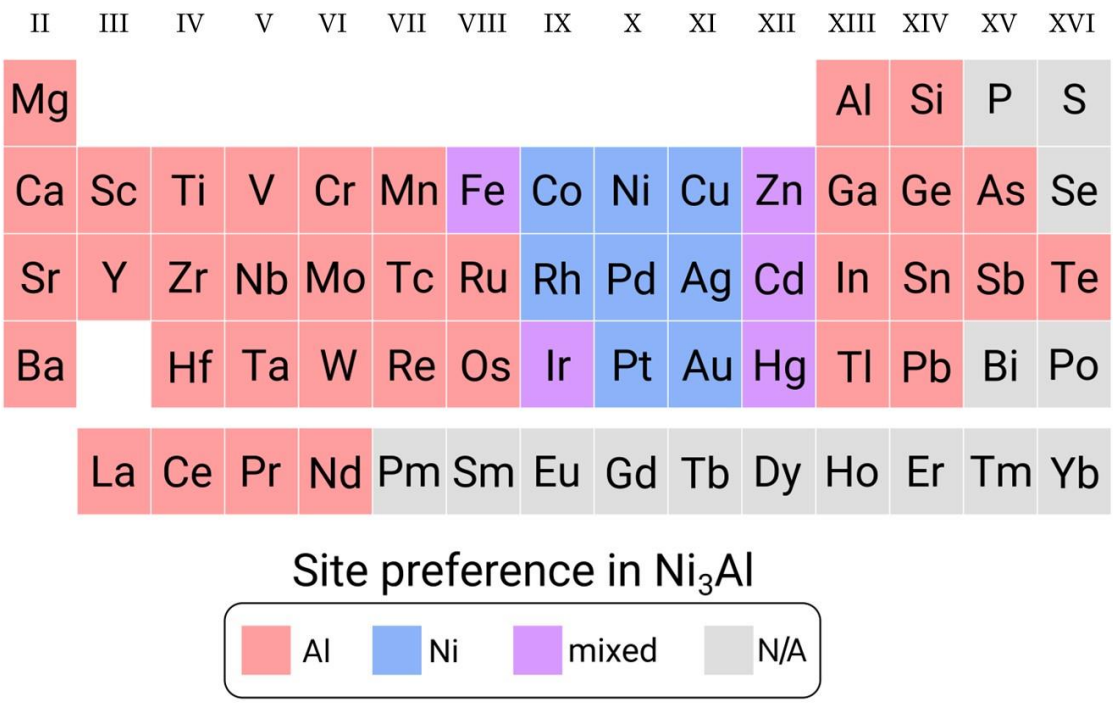

Figure 3.16: Solute sublattice preference calculated at 727 °C through grand canonical, dilute-solution model (DSM) [67]. Elements in red prefer the Al sublattice, elements in blue prefer Ni sublattice, elements in purple exhibit a mixed preference, and elements in gray were not tested. Figure adapted from reference [67].

Probably, the most used technique to acquire information about sublattice occupation for a given structure is through CALPHAD method, where the Compound Energy Formalism (CEF) is the general formalism used to model each phase in a given system. The ordered solution model allows each component to occupy two or more sublattices [68,69]. In this case, the Gibbs free energy of the ordered phase is expressed as a function of the site fraction $y_i^{(s)}$, which represents the mole fraction of component *i* in the sublattice *s*. The sublattice occupation follows the conditions given by Equation 3.23.

$$\sum_i y_i^{(s)} = 1,$$
$$x_i = \frac{\sum_s n^{(s)} y_i^{(s)}}{\sum_s n^{(s)}(1 - y_{VA})}. \tag{3.23}$$

where $n^{(s)}$ is the number of sites on sublattice *s*, x_i is the mole fraction of element *i* in the ordered phase, and y_{VA} is the vacancy fraction in each sublattice. Then, by means of Gibbs free energy minimization of all the phases in a system, information about the sublattice occupation is acquired. It goes without saying that the accuracy of this methodology depends on the accuracy of the used CALPHAD database.

As will be detailed in the chapter 4.2.2 (2nd Method), CALPHAD method was used to assess the sublattice occupation in the $L1_2$ phase in the present work.

3.4.3 Antiphase boundary energy

Although understanding the effect of each element on the χ_{APB} of the $L1_2$ phase is highly desirable, obtaining such knowledge has proven to be challenging experimentally, analytically, and computationally [50].

Experimental techniques

Experimentally, the most used technique to estimate the value of χ_{APB} is through the measurement of the distance between two superdislocations, referred herein as Δ. By using anisotropic elasticity theory, the APB energy can be calculated by the Equation 3.24 [70],

$$\chi_{APB} = \frac{g(\theta, C_{ij})}{\Delta} \tag{3.24}$$

where $g(\theta, c_{ij})$ is the interaction force function between the dislocations. This is an intricate function that depends on the dislocations character (θ) and the stiffness constants (C_{ij}) of $L1_2$ structure. It is worth mentioning that the use of simplified isotropic elastic theory for predicting χ_{APB} trough the measurement of Δ is argued to lead to erroneous results [45].

Due to the high energy associated with this defect (over 150 mJ/m² in most cases), the superdislocations tend to be very close to each other. Besides that, the overlapping of the partials and superdislocations strain fields produces an asymmetrical profile of their positions on TEM images. Hence considerable errors may be introduced in the determination of Δ [71–74]. Usually, TEM image

simulation is coupled with the experimental observation to reduce the errors of the measurements [75,76].

Aside from the challenges associated with the measurement of dislocation width, one of the major disadvantages of this method is the need to produce the alloy with the composition of the $L1_2$ phase of interest to carried out the analysis. An additional complication arises when the precipitates metastable in their “original” composition, making the alloy production impracticable and, consequently, the determination of the APB energy.

Because of experimental difficulties, most data of χ_{APB} determined by the aforementioned technique is limited to simple binaries compounds and for few ternaries with small additions of the third species [77]. The antiphase boundary energy for some alloys is presented in the Figure 3.17 together with the errors associated with the measurements. For some compositions, their correct and uncorrected values are reported. As can be seen, in most alloys the APB energy is higher than 150 mJ/m^2, and the values without correction are underestimated. Besides that, a scatter in the values of APB can be observed even for alloys with similar compositions.

Another way of estimating the value of χ_{APB} is by fitting the experimental precipitation's contribution to yield stress to previously described precipitation hardening models. As discussed in Section 3.3.4, the peak-aging equation may not accurately quantify the contribution of precipitation hardening at the peak aging condition, and the overaged equation includes an adjustable parameter that prevents a precise estimation of χ_{APB}. Therefore, the fitting process is often performed using the data of underaged alloys [51,78,79]. However, for the application of this method a great experimental effort is needed. The alloy must be produced, aged for different times, and characterized. This latter step involves the determination of lattice parameter of the matrix, volume fraction of the precipitates, and the average radius of the precipitates. Furthermore, the yield stress of the alloy aged for different times needs to be assessed and the solid solution contribution to yield strength should be subtracted from the measured values. Table 3.1 shows the values estimated by Nembach and Neite [52] and by

Ardell [45] using this approach for different alloys composed of an FCC matrix and $L1_2$ precipitates.

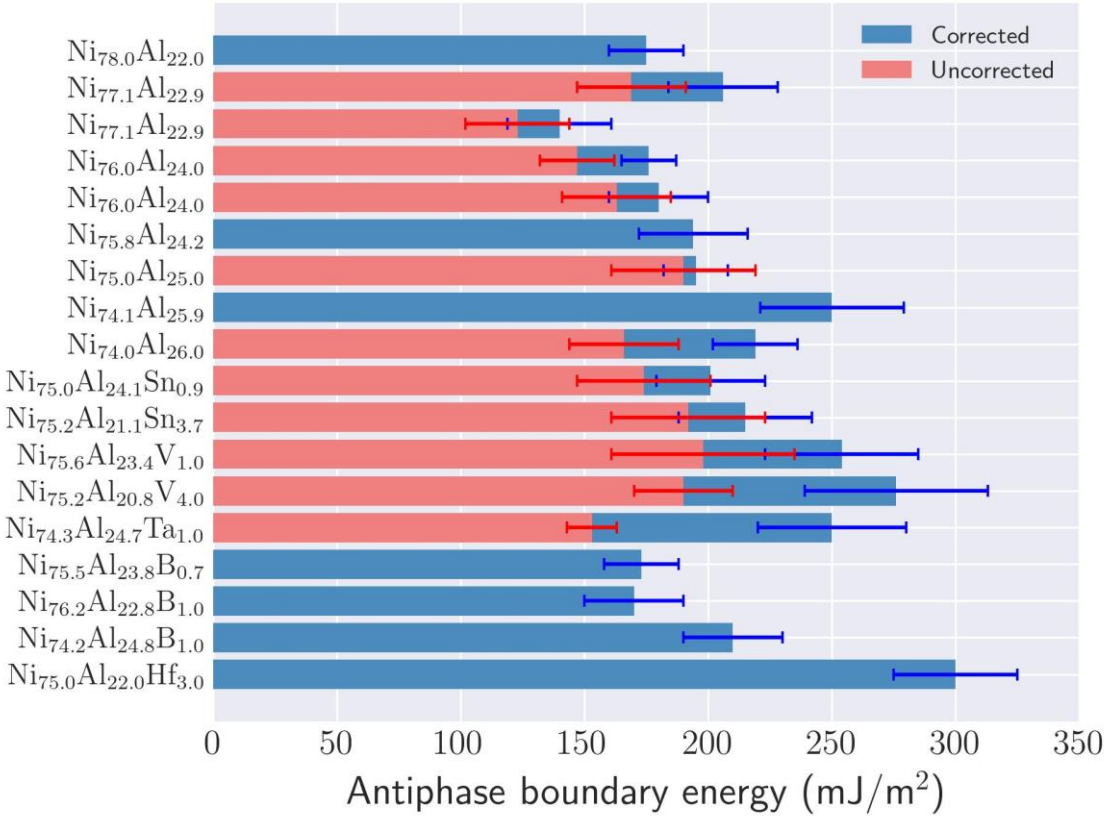

Figure 3.17: Antiphase boundary energy determined experimentally through the measurement of superdislocation distance by TEM. The compositions of the alloys are specified in atomic percentage. Data extracted from reference [77].

Table 3.1: Antiphase boundary energy values estimated by fitting experimental data of yield stress with theoretical models of precipitation hardening contribution.

Alloy	**Antiphase boundary energy (mJ/m²)**	
	Nembach-Neite [52]	Ardell [45]
Ni-Al	192-345	185
A286	320	257
Nimonic 80A	310	193
Nimonic 105	-	134
Nimonic PE 16	89-258	162

Analytical models

A nearest-neighbor bonding model was developed by Flinn [80] to estimate the antiphase boundary energy in the $L1_2$ structure. The antiphase boundary energy per unit area for burgers vector $^{a}/_{2}\,[\pm1,\pm1,0]$ and crystallographic plane (h,k,l), with $h \geq k$ and all $h,k,l \geq 0$, is given by

$$\chi_{APB}^{a/2[n\bar{n}0](111)} = \frac{W^{(1)}}{a^2}\frac{h}{\sqrt{h^2+k^2+l^2}}, \qquad W^{(1)} = 2\phi_{AB} - (\phi_{AA} - \phi_{BB}). \tag{3.25}$$

where ϕ_{ij} is the pairwise interaction energy between atoms *i* and *j*.

Although it is well known that the APB energy is anisotropic and that APB energy in {001} planes are lower than APB energy in {111} planes, experimental evidence show that their values are of the same order of magnitude [77]. However, the previous equation predicts a zero energy for APB in the (001) plane. While forbidden bonds in the nearest neighbor distance are created after dislocation passage on the {111} planes, this is not observed for shearing along the $^{a}/_{2}\,[\pm1,\pm1,0]$ direction on {001} planes. This can be easily realized by noting that {002} planes are occupied solely by atoms on atomic site A. Therefore, it is suggested that for more reliable estimation of APB the interaction energy at least up to 4th nearest neighbor distance needs to be accounted for [64].

More generalized models for APB energy estimation were later developed [81–83]. The energy for interaction with nth neighbor atom is accounted for by the terms W^i. The eight first terms for APB energy in {111} and {001} types of planes are show in Equation 3.26,

$$\begin{aligned}\chi_{APB}^{a/2[n\bar{n}0](111)} &= \frac{1}{\sqrt{3}a^2}\left(W^{(1)} - 3W^{(2)} + 4W^{(3)} - 6W^{(4)} + 6W^{(5)} - 3W^{(6)}\right.\\ &\left. + 12W^{(7)} - 6W^{(8)} + \cdots\right)\\ \chi_{APB}^{a/2[n\bar{n}0](001)} &= \frac{2}{a^2}\left(-W^{(2)} + 4W^{(3)} - 4W^{(4)} - 4W^{(6)} + 8W^{(7)} - 2W^{(8)}\right.\\ &\left. + \cdots\right)\end{aligned} \tag{3.26}$$

where $W^{(n)}$ are the nth neighbour ordering energies.

Miodownik and Saunders [84] proposed a model to calculate the APB using the Equation 3.26 accounting for the interaction up to 3rd nearest neighbor distance. In their model, the interaction parameters ($W^{(1)}$, $W^{(2)}$, and $W^{(3)}$) are estimated from the values of enthalpy of mixing of FCC solid solution and the ordering enthalpy ($\Delta H_{ord}^{FCC \rightarrow L1_2} = \Delta H_{mix}^{L1_2} - \Delta H_{mix}^{FCC}$), which are calculated through CALPHAD method. Strictly speaking, the Miodownik and Saunders's model is applicable only for binaries alloys, since it only accounts for A-A, A-B, and B-B interactions. However, it is frequently extrapolated for high-order systems in the literature [85–87].

Computational methods

The use of computational methods that allow predicting the χ_{APB} in advance proves to be extremely relevant in the context of developing new alloys. These methods, in general, consist of calculating the total energies of the primitive structure of interest (E_{prim}) and the energy of the same structure after the introduction of the antiphase boundary (E_{APB}). The overall strategy is described as follows:

1. $L1_2$ structure is usually created with their $[\bar{1}01]$, $[1\bar{2}1]$, and [111] crystallographic directions parallel to x, y, z axis, respectively, as shown schematically in Figure 3.18a.
2. The energy of the system in the latter configuration is calculated. The resulting energy is defined as E_{prim}.
3. The atoms in upper/lower half are shifted along the $[\bar{1}01]$ direction with a magnitude equal to $a/\sqrt{2}$, where a is the lattice parameter of the structure. The cell after atoms displacement is shown in Figure 3.18b.
4. The energy of the system in the new configuration is calculated. The resulting energy is defined as E_{APB}.

The energy difference between these two structures is presumed to be exclusively due to the interfacial defect. From this consideration, the χ_{APB} can be expressed according to Equation 3.27 [88].

$$\chi_{APB} = \frac{E_{APB} - E_{prim}}{A} \tag{3.27}$$

where A is the area of the interfacial defect in the computational cell. When periodic boundary condition is assumed in the computational technique, the area of the defect is multiplied by a factor of two.

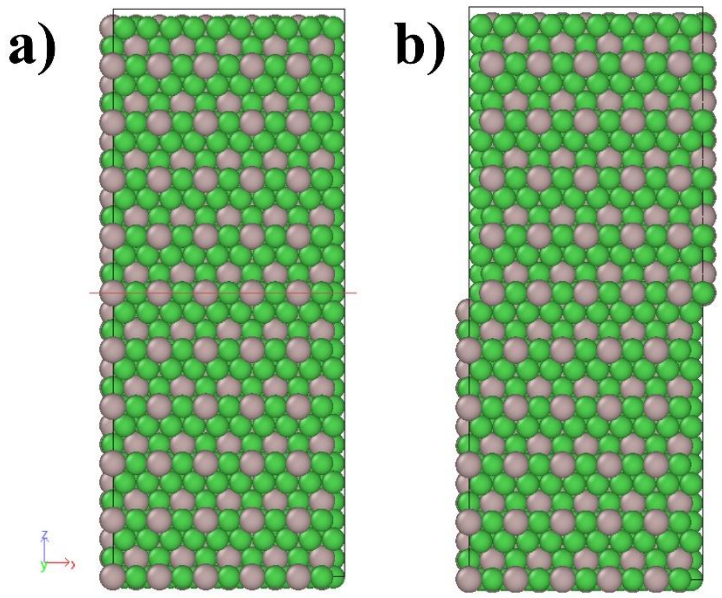

Figure 3.18: a) $L1_2$ structure with their $[\bar{1}01]$, $[1\bar{2}1]$, and [111] crystallographic directions parallel to x, y, z axis, respectively; b) cell shown in a after antiphase boundary creation.

For statistically consistent estimation in alloys containing three or more species, the calculation for a given composition should be performed several times with atoms distributed randomly throughout the cell, or sampling techniques should be used instead. As shown by Vamsi and coworkers, the influence of a given atom on APB energy may change drastically as a function of its distance from the interfacial defect [89]. Therefore, not only the alloying element but also its position from the fault plane affects the APB energy. Computational techniques have certain drawbacks, such as their time-consuming nature and limited ability to evaluate dilute additions, given that the computational cells generally consist of only about 100 atoms. Additionally, when constructing supercells, one must assume the sublattice preference of each atom beforehand.

A compilation of some works [67,77,88,90] that investigated the influence of a third specie addition in the Ni_3Al structure by computational methods is shown in Figure 3.19. Here, only the effect of those elements most used in commercial

superalloys is presented, albeit these studies cover the influence of other metals. For sake of comparation between the different investigations, the y axis is normalized by the APB energy of $Ni_{75}Al_{25}$ calculated in each work, i.e., $\Delta\chi_{APB} = \chi_{APB} - \chi_{APB}^{Ni_{75}Al_{25}}$, so that the influence of the third species M on Ni-Al-M system can be better understood.

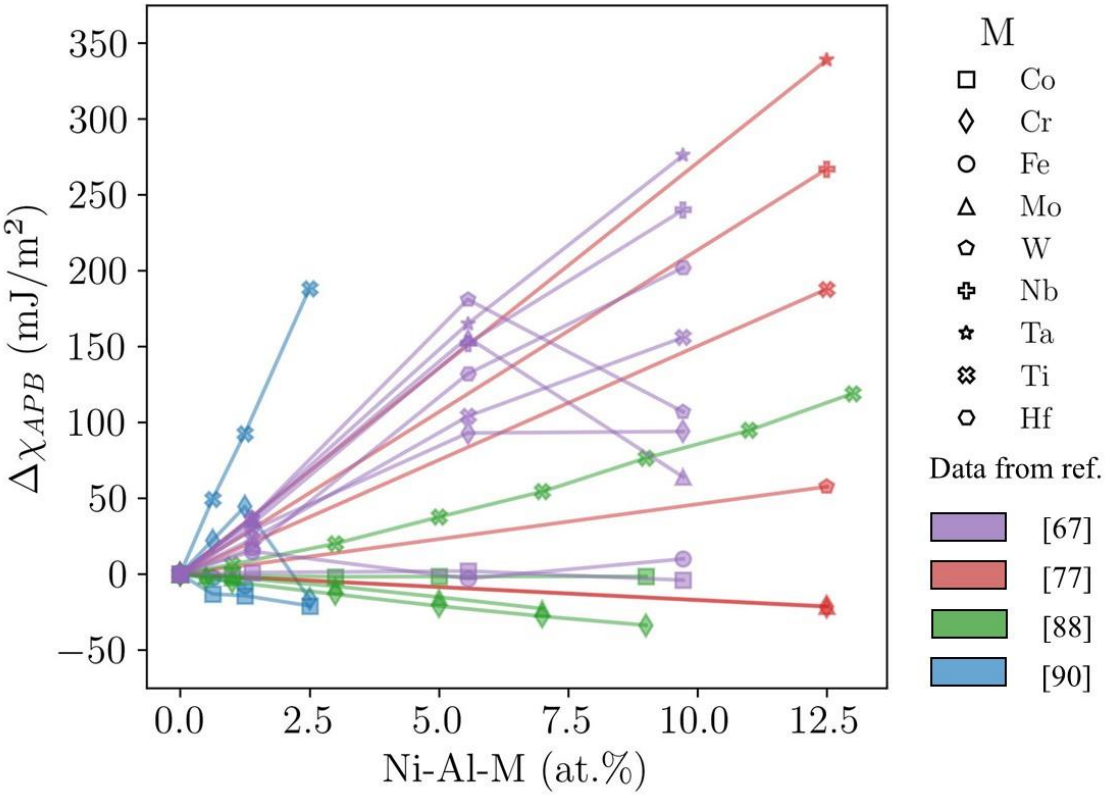

Figure 3.19: Effect of ternary addition in the APB energy in Ni_3Al structure investigated by computational methods. Each color indicates the results extracted from a given study in the literature [67,77,88,90].

As can be observed, Co tends to decrease the APB energy. However, the magnitude of this change is minimal. The effect of Cr is controversial. While some studies predicts that this metal decrease the APB energy in a wide range of concentration, other studies shows that Cr has a beneficial effect up to certain amount. All the works [90,91] agree that Ti and Nb increase the antiphase boundary energy of the $L1_2$ phase. However, excessive additions of the former increase the propensity for the formation of the Ni_3Ti compound, also known as η phase [91], Strukturbericht designation $D0_{24}$ (space group $P6_3/mmc$), which is

generally considered deleterious to mechanical properties. On the other hand, excessive addition of Nb increase the propensity of formation of γ" phase, Strukturbericht designation $D0_{22}$ (space group $I4/mmm$), lowering the content of Nb in $L1_2$ structure. Nonetheless, $D0_{22}$ phase has a beneficial effect to yield stress and is one of the major strengthening phases on commercial Inconel 718 alloy, which is a benchmark for high temperature applications.

Since DFT calculations are time consuming, Crudden et. al. suggested the use of an empirical coefficient (k_i) to translate the contribution of each element to the value of χ_{APB}. The k_i values were determined by the authors from their DFT calculations, and they are presented in Table 3.2. To determine the χ_{APB} in multicomponent $L1_2$ structures, Crudden and coworkers suggest a linear superposition of the contribution of each element, i.e., synergistic effects are not considered. Accordingly, the antiphase boundary energy can be determined by Equation 3.28.

Table 3.2 Contribution coefficients for antiphase boundary energy of the different elements studied by Crudden et al. in mJ/m².%at.

Element	k_i (mJ/m².at. %)
Cr	-1.7
Mo	-1.7
W	4.6
Ta	27.1
Nb	21.4
Ti	15

$$\chi_{APB} = \chi_{APB}^{Ni_{75}Al25} + \sum_{i=1}^{n}(k_i x_i) \tag{3.28}$$

where $\chi_{APB}^{N75Al25}$ is the value of the antiphase boundary energy of the $Ni_{75}Al_{25}$ structure, *n* is the number of "solutes" in the $L1_2$ phase and x_i is the concentration of the "solute" *i* in the $L1_2$ phase, in atomic percentage. Crudden et al suggest the use of the value of $\chi_{APB}^{N75Al25}$ determined experimentally by TEMs (195 ± 13 mJ/m²).

Dodaran et al. [88] carried out atomistic calculations to systematically assess the alloying effects of Ti, Cr, Co on multicomponent Cr-Co-Ni-Al-Ti system. The effect of these elements on APB was studied at different temperatures (227 °C – 1027 °C). Following Crudden et al. [77], an empirical equation was proposed to calculate the antiphase boundary energy of the $L1_2$ phase.

$$\chi_{APB} = \chi_{APB}^{Ni_3Al} + \sum_{i=1}^{n} K_i x_i + F_1 x_{Ti} x_{Cr} + F_2 x_{Ti} x_{Co} + F_3 x_{Cr} x_{Co} + H x_{Ti} x_{Cr} x_{Co} \quad (3.29)$$

where x_i is the atomic percentage of element *i* in the $L1_2$ structure, and K_i, F_1, F_2, F_3, and H are empirical coefficients. As can be noted, interaction terms between the species are also included in this equation. The values of the coefficients for the different temperatures are presented in Table 3.3. These values were determined by least square minimization method using the Equation 3.29 and the computational data.

Table 3.3: Contribution coefficient for antiphase boundary energy at different temperatures for each element (ki) and interaction factors between different solutes (Fi). Coefficients have units in mJ/m².

Coefficients (mJ/m²)	**227 °C**	**427 °C**	**627** °C	**827** °C	**1027** °C
k_1(Ti)	8.862	8.196	8.011	7.795	7.56
k_2(Cr)	-4.497	-4.793	-5.256	-6.184	-7.962
k_3(Co)	-1.229	-1.423	-1.574	-1.838	-2.41
F_1(Ti-Cr)	0.8166	0.6286	0.5223	0.6641	0.8702
F_2(Ti-Co)	0.0916	0.0954	0.0628	0.0634	0.1109
F_3(Cr-Co)	-4.337	-4.44	-5.266	-5.681	-5.532
H(Ti-Cr-Co)	0.3211	0.3724	0.4626	0.4975	0.4792

Recently, Vamsi and Karthikeyan [89] proposed an environment dependent nearest neighbor bond (EDNNB) model for estimating the APB energy

on {111} planes in multicomponent Ni-base superalloys. Using CALPHAD calculations, the authors showed that the nickel sublattice is primarily composed of Ni and Co atoms. They also argued that previous DFT studies have shown that substituting Ni with Co has a minimal effect on APB (111) energies. Therefore, they proposed that the composition of the Al sublattice controls the overall APB energy. Since Al-Al, Al-Ta, Al-Cr, Ti-Cr, Ti-Ti, and Ta-Ta interactions accounts for about 80% of violations encountered in Al-sublattice in most Ni-superalloys, the authors proposed the following empirical equation to calculate the APB energy in these multicomponent systems,

$$\chi_{APB} = \alpha \left[\begin{pmatrix} x_{Al}^2 & x_{Ti}^2 & x_{Ta}^2 & 2x_{Al}x_{Ti} & 2x_{Al}x_{Ta} & 2x_{Al}x_{Cr} & 2x_{Ti}x_{Cr} \end{pmatrix} \begin{pmatrix} \Gamma_{AlAl} \\ \Gamma_{TiTi} \\ \Gamma_{TaTa} \\ \Gamma_{AlTi} \\ \Gamma_{AlTa} \\ \Gamma_{AlCr} \\ \Gamma_{TiCr} \end{pmatrix} \right], \quad (3.30)$$

$$\Gamma_{ij} = \Gamma_{ij}^0 + \begin{pmatrix} x_{Ti} & x_{Ta} & x_{Cr} & x_{Mo} & x_{Nb} & x_{Ni} & x_W \end{pmatrix} \begin{pmatrix} \eta_{ij,Ti} \\ \eta_{ij,Ta} \\ \eta_{ij,Cr} \\ \eta_{ij,Mo} \\ \eta_{ijl,Nb} \\ \eta_{ij,Ni} \\ \eta_{ij,W} \end{pmatrix},$$

$$\alpha = \frac{1}{\sum p_{ij}}.$$

where x_k is the concentration of species k in the Al-sublattice, while Γ_{ij} represents the APB energy on {111} plane with a specific combination of interaction across the APB. Here, *ij* denotes the type of bonding that is gained upon the creation of APB. Additionally, Γ_{ij}^0 is a penalty term that arises due to a specific bonding type in Ni_3Al structure. The coefficient $\eta_{ij,k}$ is a resultant coefficient that accounts for the effect of k at different distances from the fault, and α is a scaling factor used to account for any violations that are ignored in the calculation. The probability of having a violation of type *ij* across the fault is denoted by p_{ij}, and $\sum p_{ij}$ represents the summation of probabilities of the seven Γ_{ij} terms. The values of Γ_{ij}^0 and $\eta_{ij,k}$

were determined using DFT calculation and they are summarized in the Table 3.4.

Since there is no experimental data for APB energy in multicomponent systems available in the literature, the authors of the latter work evaluated the predictions of the models based on the yield stress of several superalloys, and a pleasing correlation was found. However, it seems to overpredict strength.

The evaluation of APB energy in multicomponent alloys is a complex topic, as discussed in this chapter. A deep understanding of χ_{APB} is crucial for designing alloys with optimized properties, and this has been the focus of considerable attention in recent literature [67,88,89]. However, it is important to note that optimizing the APB energy alone is not sufficient for effective alloy design. As previously demonstrated, certain elements can have a beneficial effect on APB anergy, but excessive addition may result in the formation of other phases that can be detrimental to mechanical properties. Therefore, developing models that integrate both antiphase boundary energy and phase equilibrium predictions shows promise for advancing alloy development.

Table 3.4: Penalty terms (Γ_{ij}^{0}) and environment strength coefficients ($\eta_{ij,\mathrm{k}}$) for ij violation in the Al-sublattice. All terms are given in units of mJ/m².

ij	Γ_{ij}^{0}	$\eta_{ij,\mathrm{Ti}}$	$\eta_{ij,\mathrm{Ta}}$	$\eta_{ij,\mathrm{Cr}}$	$\eta_{ij,\mathrm{Mo}}$	$\eta_{ij,\mathrm{Nb}}$	$\eta_{ij,\mathrm{Ni}}$	$\eta_{ij,W}$
AlAl	189.0	97.2	163.9	82.6	216.5	162.6	-23.6	247.5
AlTi	353.9	96.1	224.2	116.9	312.7	197.1	-109.5	367.0
AlTa	511.8	129.4	159.4	-36.0	132.5	92.6	-222.0	212.7
AlCr	259.8	50.5	49.0	114.5	-14.6	35.7	-108.8	29.2
TiTi	521.5	221.3	284.9	286.4	263.8	271.2	139.3	317.6
TiCr	390.9	17.0	-46.8	50.5	-151.3	-82.4	-76.8	-124.2
TaTa	688.8	111.7	1.3	13.9	-121.9	8.3	99.5	-161.6

In this work, two different models were employed to estimate the APB energy of the newly designed alloys, namely the Dodaran and Vamsi models. As previously shown, the Dodaran model is based on the $L1_2$ composition, while the Vamsi model is dependent on the concentration of elements present in the Al-

sublattice of the $L1_2$ structure. These compositions were assessed through the CALPHAD method.

4 MATERIALS AND METHODS

4.1 Materials

Chromium, Cobalt, Nickel, and Aluminum of commercial purity (> 99 wt.%) were used to produce the alloys in this work. Two types of Titanium were used as raw material: for the first alloy produced in this work, $Cr_{29.7}Co_{29.7}Ni_{35.4}Al_{4.0}Ti_{1.2}$, Titanium sponge (Sigma Aldrich, 99.5% metal basis) was utilized, whereas Titanium rods (Alfa Aesar, 99.7% metal basis) were used to produce the remaining alloys, namely $Cr_{20}Co_{12.5}Ni_{60}Al_{2.5}Ti_5$, $Cr_{22.5}Co_{10}Ni_{60}Al_5Ti_{2.5}$, and $Cr_{20}Co_{17.5}Ni_{50}Al_{12.5}$.

4.2 Methods

In this work, two distinct approaches were utilized for designing precipitation-hardened HEAs. In the first, referred as 1st Method hereafter, the focus was to introduce $L1_2$ precipitates into a highly concentrated Cr-Co-Ni matrix. In the other approach, the CALPHAD method was used to screen a large compositional field of Cr-Co-Ni-Al-Ti system. The alloys with a two-field FCC+$L1_2$ at 750 °C had their solid solution and precipitation-hardening contribution estimated using models detailed in literature review chapter. This second method is referred to as 2nd Method. Details of each approach such as design strategy, production, processing, and characterization are described in the following paragraphs. To make it easier for the reader, this section and the following chapter (Results and Discussion) are split in two parts, where each one is concerned to present and discuss the distinct approaches used in this work.

4.2.1 1st Method

- **Design strategy**

As detailed in literature review chapter, the ternary CrCoNi is one of the strongest and toughest face-centered cubic (FCC) single-phase material discovered to date. In this sense, the aim of this first approach was to introduce nanometric $L1_2$ precipitates in a concentrated Cr-Co-Ni matrix by means of aging treatment at high temperatures. Through CALPHAD calculations, the

composition was adjusted by replacing some Ni, Cr, and Co with Al, and Ti, so that the following criteria were met:

- An FCC field was stable at high temperatures;
- An FCC+$L1_2$ field was stable in the temperature interval between ~650 and 850 °C;
- The FCC phase in this two-phase region presented a highly concentrated Cr-Co-Ni composition;

The $Cr_{29.6}Co_{29.6}Ni_{35.2}Al_{4.0}Ti_{1.5}$ alloy was chosen as a potential candidate. As will be detailed in the results section, the produced alloy presented titanium-rich inclusions in its microstructure, which lowered the Ti on the alloy. The final composition used on this work had therefore less Ti, namely $Cr_{29.7}Co_{29.7}Ni_{35.4}Al_{4.0}Ti_{1.2}$ (at. %).

- **Production**

An ingot of approximately 3 kg of the $Cr_{29.7}Co_{29.7}Ni_{35.4}Al_{4.0}Ti_{1.2}$ alloy was prepared using commercially pure elements (purity of 99% or above). The material was induction melted in a mullite ($3Al_2O_3$-$2SiO_2$) crucible under an air atmosphere and cast into a graphite mold with four veins of ~20mm diameter and ~200mm height. During the melting, argon gas was blown through a quartz nozzle into the alloy to accelerate the slag formation and improve alloy cleanliness.

- **Processing**

Slabs were cut from the ingot, homogenized at 1200 °C for 4h, and water-quenched. This material was cold-rolled in multiple passes until 50% reduction was achieved, which was then followed by recrystallization heat treatment at 1100 °C for 1h. For rolling purposes, a FENN rolling mill with rotational speed of 51 rpm and rolls with diameter of 101.6 mm was used. The procedures were repeated until the initial 20 mm in diameter slabs were reduced to 2 mm thickness sheets. Later, the samples were solution-treated at 1200 °C for 1h, water-quenched, and aged at 850°C for different times.

- **Characterization**

Structural and Microstructural Characterization: The crystalline phases were characterized by X-ray diffraction (XRD) in a Bruker D8 ADVANCE diffractometer operating with Cu-Kα radiation. The diffraction angle (2θ) was evaluated in the range of 30-90° with a step size of 0.019° and a time per step of 0.28s.

The microstructural characterization was performed by optical microscopy after chemical etching with aqua regia (3HCl+1HNO_3, in volume), by a scanning electron microscope (SEM), using an FEI Inspect S 50 operating under 20 kV, and by a transmission electron microscope (TEM), using a TECNAI G2 F20 operating at 200 kV. Both electron microscopes were equipped with energy-dispersive x-ray (EDS).

TEM foils were prepared by mechanical grinding the samples with SiC paper down to a thickness of ~100μm. Then they were electro-polished in a solution of 25% perchloric acid in ethanol, at room temperature, using a voltage of 30V. Since precipitates presented a spherical morphology on all conditions evaluated, TEM dark-field (DF) images were acquired near an arbitrary low index zone axis using the superlattice reflections of the $L1_2$. To enhance the diffraction contrast on DF images, the samples were tilted 3-5° near the zone axis to a two-beam condition, making one of the superlattice reflections from $L1_2$ precipitates strong.

For determining the volume fraction of precipitates, the TEM foil thickness was firstly measured through the electron energy-loss spectrometry (EELS) method [35], which establishes that

$$t = \lambda \ln \frac{I_t}{I_0} \tag{4.1}$$

where I_0 is the intensity in the zero-loss plasmon peak, I_t is total intensity in the low-loss spectrum out to 50eV, including I_0, and λ is the average mean free path for these low-energy losses. The accuracy of this method is reported to be ~20 %. Then a relation for projected images considering the truncation of particles by the foil surface was used [36],

$$f = A_A \left(1 + \frac{3t}{2\langle d \rangle}\right)^{-1} \quad (4.2)$$

where *f* is the volume fraction of precipitates, A_A is the area fraction of precipitates on the projected image, $\langle d \rangle$ is the mean diameter of the particles, and t is the foil thickness in the analyzed region.

Thermal analysis: thermal analysis of the sample in the 10h aged condition was performed using a differential scanning calorimetry (DSC) Netzsch 404 under an argon flow atmosphere of ~ 1bar. The sample was heated up to 1000 °C with a constant heating rate of 40 °C/min. A Pt-Rh crucible was used for increased sensibility.

Hardness curve: A Vickers diamond indenter Shimadzu HVM-G20ST was used to measure the hardness as a function of aging time. Hardness measurements were performed at room temperature following the ASTM-E384 standard [37]. Ten measurements were made on each sample. A load of 500g and a dwell time of 15 s were used during the tests.

Tensile tests: Standardized ASTM-E8 subsize specimens [92] were cut from the cold-rolled sheets by electrical discharge machining (EDM) with their longitudinal axes parallel to the rolling direction. The specimens were given a final solution-treatment at 1200°C for 1h, quenched into water, and aged for 0.5, 2, 4, 22, and 166 hours at 850 °C. Tensile tests were performed at room temperature in an Instron machine at a strain rate of $10^{-3}\ s^{-1}$. A contact extensometer was used for strain measurements. Duplicate tests were performed on specimens aged in the same condition. The yield strength of the alloys was determined as the stress at which 0.2% plastic strain occurs, often called 0.2% offset yield strength.

4.2.2 2nd Method

Design strategy

Most alloys developed to date using computational thermodynamics to find promising compositions in a system consisting of four or more species were designed based on pseudo-binary or pseudo-ternary diagrams. In these approaches, two or more elements must be fixed in a pre-selected ratio due to

limited degrees of freedom (DF). While this strategy is valuable and has aided the design of alloys with interesting properties, there is always a region of compositional space that is missed using these methods. For example, consider a system A-B-C-D. If a pseudo-ternary diagram is constructed, the user must select two species to form a component in a pre-selected ratio. The corners of pseudo-ternary diagram may be (A_iB_j), C, and D, where *i* and *j* are arbitrary numbers that translate the ratios between the species A and B. The compositional degrees of freedom in this pseudo-ternary are only two, whereas the system has three DF in practice. Therefore, all compositions lying in a region of compositional space outside the pre-selected ratio are neglected during the calculations.

In this context, a method was developed to efficiently explore the multidimensional compositional space of the Cr-Co-Ni-Al-Ti system and design alloys with enhanced mechanical properties. Specifically, equilibrium solidification calculations were performed using the CALPHAD method through HTC module of Pandat software. This module has the capability to automatically perform calculations based on user-defined compositional limits, concentration steps for each element, and a specified temperature range. The PanHEA2021 database was used to carry out the thermodynamics calculations. This database presents a complete description of all binaries and ternaries systems explored in this work. The concentration ranges and steps used during calculations for each element are presented in the following series of inequalities, all in atomic percentage.

$$\begin{cases} 0 \leq x_{Cr} \leq 40, \Delta x_{Cr} = 2.5 \\ 0 \leq x_{Co} \leq 40, \Delta x_{Co} = 2.5 \\ 0 \leq x_{Al} \leq 15, \Delta x_{Al} = 2.5 \\ 0 \leq x_{Ti} \leq 15, \Delta x_{Ti} = 2.5 \\ 0 \leq x_{Ni} \leq 60, \Delta x_{Ni} = - \end{cases}$$

where Nickel was set as a balance element.

The previous region of compositional space yielded a total of 11235 different compositions. For each alloy, the calculation was conducted between the *liquidus* and 500 °C. In total, CALPHAD minimization was performed over 3.5

million points. All the data generated by the calculations were then processed and analyzed using Python programming language.

Three criteria were employed to filter the alloys, namely:

- The alloy should have a two-phase field FCC/A1+$L1_2$ (γ+γ') at 750 °C. Most nickel superalloys are commonly applied around this temperature;

- The *solvus* temperature (T_{Solvus}) should be less than or equal to 1100 °C. This upper limit was chosen to reduce the challenges during the processability of the alloys;

- The solidification interval ($\Delta T_{Solidification}$) should be less than or equal to 100 °C. This upper limit for the solidification interval was defined to minimize chemical segregation during solidification and prevent solidification defects such as porosity and cracks.

The Venn diagram presented in Figure 4.1 provides a summary of the number of alloys that fulfilled each of the aforementioned criteria, as well as their intersections. It can be observed that out of the initial 11235 alloys, only 374 (~3%) satisfied all the criteria.

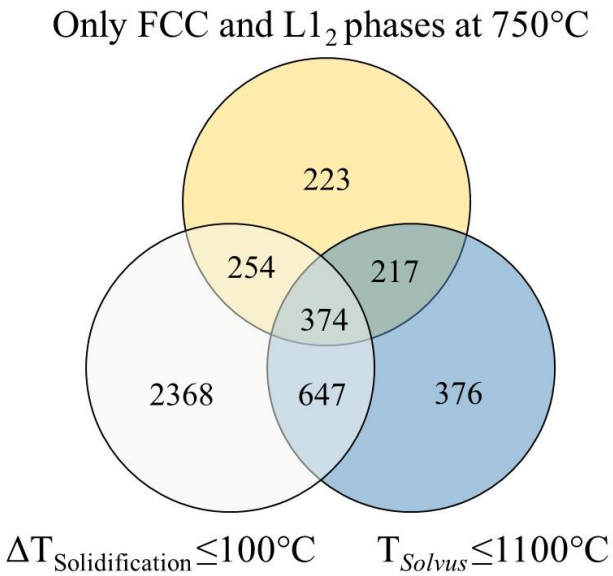

Figure 4.1: Venn diagram showing the number of alloys that met each of the three filtering criteria and the intersections between them.

Then the composition of FCC phase at 750 °C was used as input in Varvenne's solid solution strengthening model [15]. The elastic constants of the alloys were calculated using the Equations 4.3 and 4.4. The effect of titanium on the elastic properties was neglected, but this is reasonable since titanium strongly partitions to $L1_2$ phase. For instance, the maximum titanium concentration in the FCC phase at 750 °C in the filtered alloys was of only 3.7%. The atomic volume of the elements used in the calculations is given in Table 4.1. These equations and inputs were previously proposed during the mathematical modeling of the yield stress of the alloy designed using the 1st approach in this work. They will be discussed in detail in the "Results and Discussion" chapter.

$$G = (76c_{Ni} + 92c_{Co} + 93c_{Cr})(1 - 1.51c_{Al}) \quad (4.3)$$

$$v = 0.31c_{Ni} + 0.27c_{Co} + 0.32c_{Cr} + 0.2c_{Al} \quad (4.4)$$

Table 4.1: Atomic volume of Cr-Co-Ni-Al-Ti used for calculating the solid soliton hardening contribution in this work.

Element	**Ni**	**Cr**	**Co**	**Al**	**Ti**
Atomic volume(Å^3)	10.94	12.86	11.52	13.52	14.48

To estimate the precipitation hardening contribution to yield strength, firstly antiphase boundary energy was calculated using Dodaran and Vamsi's models. As suggested by these authors, the composition of the $L1_2$ phase at 750 °C was used as input in the former, whereas the Al-sublattice composition was used as input in the latter. Dodaran's model predicts unrealistic negative values for χ_{APB} when the alloys are Ti-absent. This is mainly justified by a strong penalty term due to Cr-Co interaction and by the fact that the reported coefficients were estimated only for composition of the $L1_2$ phase with Ti concentration in the range of ~10-30 at.%. Therefore, for Ti-free alloys, the Cr-Co cross term in Dodaran's model was neglected. As shown in Figure 4.2, the correlation between the two models is good, but the χ_{APB} calculated by Vamsi's model tend to be ~125 mJ/m² higher than those predicted by Dodaran's model for the filtered alloys.

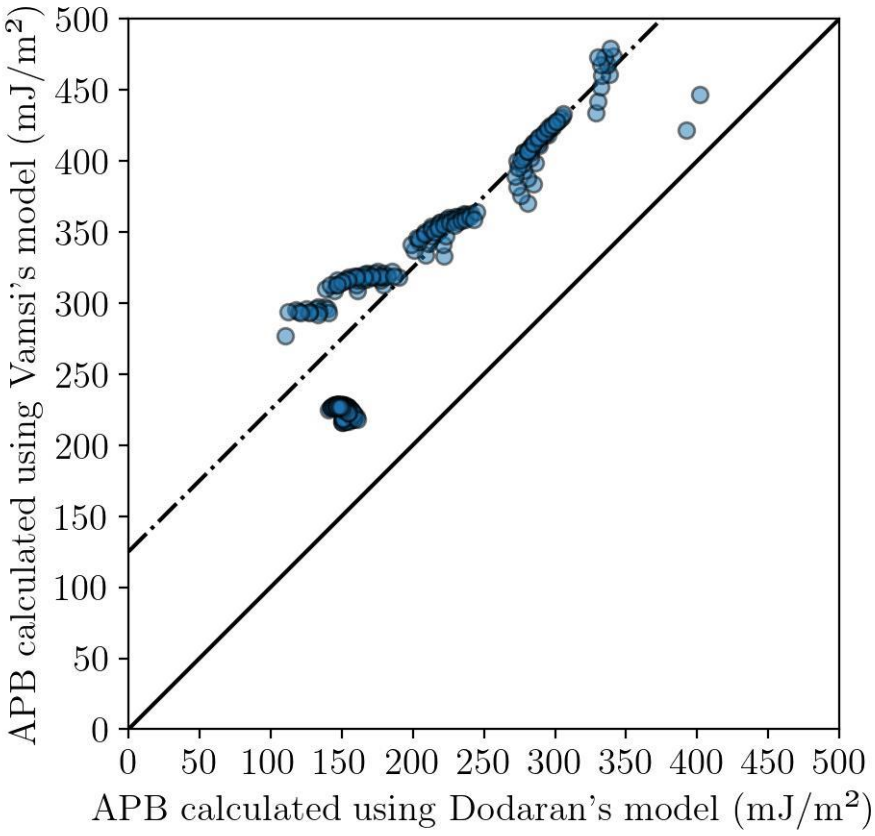

Figure 4.2: Antiphase boundary energy calculated for the filtered alloys using Dodaran and Vamsi's models.

Using the antiphase boundary energy estimated previously by Dodaran's model and the volume fraction of $L1_2$ phase at 750 °C, calculated by the

CALPHAD method, the precipitation hardening contribution to yield strength was calculated at peak-aged condition using Equation 3.22, which is repeated here for sake of clarity.

$$\tau_c = 0.81 \frac{\chi_{APB}}{2b} \sqrt{\frac{3\pi f}{8}} \tag{3.22}$$

As mentioned previously, this simplified equation might fail to quantitatively predict the precipitation hardening contribution at peak aged condition, but experimental data from mechanical tests shows excellent correlation between $\Delta\tau_{c,max}/f^{1/2}$ and χ_{APB} [45], where $\Delta\tau_{c,max}$ is the maximum precipitation hardening contribution to yield stress measured experimentally. Therefore, for design purposes the previous equation should be satisfactory.

After mathematical modeling of solid-solution and precipitation hardening strengthening, the alloys were ranked in descending order of the summation $\sigma_{SS} + \sigma_{pp}$. To evaluate the effectiveness of the proposed methodology, three alloys were selected. One with the most promising yield stress and two others to test the proposed model: one with a similar volume fraction of precipitates but distinct antiphase boundary energy of the most promising alloy, and the other with a much higher volume fraction of precipitates but much lower antiphase boundary energy. Table 4.2 summarize information related to the selected alloys with FCC and $L1_2$ phases as equilibrium phases at 750 °C.

Table 4.2: Equilibrium molar fraction of $L1_2$ phase at 750 °C (f_{L12}), solid solution hardening contribution to yield strength (σ_{ss}), and precipitation hardening contribution to yield strength (σ_{pp}) for $Cr_{20}Co_{12.5}Ni_{60}Al_{2.5}Ti_5$, $Cr_{22.5}Co_{10}Ni_{60}Al_5Ti_{2.5}$, and $Cr_{20}Co_{17.5}Ni_{50}Al_{12.5}$ alloys.

Alloy	σ_{ss} (MPa)	f_{L12} at 750 °C	χ_{APB} (mJ/m²)	σ_{pp} (MPa)	$\sigma_{ss} + \sigma_{pp}$ (MPa
$Cr_{20}Co_{12.5}Ni_{60}Al_{2.5}Ti_5$	216	0.35	329	1035	1251
$Cr_{22.5}Co_{10}Ni_{60}Al_5Ti_{2.5}$	211	0.34	209	645	856
$Cr_{20}Co_{17.5}Ni_{50}Al_{12.5}$	206	0.49	158	583	790

Production

For production of the selected alloys, the raw materials were melted in a non-consumable arc-melter furnace, manufactured by Arcast Inc., model Arc 200, and the molten alloy was poured into a copper mold of 12.6 mm diameter and ~90 mm length.

Processing

The as-cast cylindrical ingots were homogenized at 1200 °C for 12h in a resistance furnace fabricated by Carbolite Gero, model CWF 13, and water quenched. These samples were then cold rolled in multiple passes of ~5% reduction until a thickness of 4.9 mm (total reduction of ~ 60%) was achieved. This was followed by a recrystallization treatment at 1200 °C for 1 hour. The recrystallized sheets were then cold rolled again until a final thickness of about 1 mm (total reduction of ~90%) was achieved. For rolling purposes, a Stanat rolling mill, model CX-100, with rotational speed of 48 rpm and rolls with diameter of 38.1 mm was used.

Characterization

Structural and Microstructural Characterization: The crystalline phases were characterized by X-ray diffraction (XRD) in a PANalytical Multi-Purpose Diffractometer, model X'Pert PRO MPD, operating with Cu-Kα radiation. The 2θ diffraction angle was evaluated in the range of 30-110°. A time per step of 0.31s and step-size of 0.017° were used for the diffraction experiments.

A Light Optical Microscope (LOM), LECO Olympus DSX100, was used for acquiring optical micrographs of the samples under the different conditions. Glyceregia etchant (3HCl+1HNO_3+1Glycerine) was used to etch the samples and reveal their microstructure. Image processing and image analysis were performed using ImageJ software.

For characterization of precipitates size and morphology as well as the grain boundary microstructure either a Scanning Electron Microscope (SEM) TESCAN S8252G or a FEI Magellan 400L was used. Both equipment uses a field emission gun (FEG) as electron source. Nanoscale compositional analysis were performed with an EDAX Octane Elect Plus energy dispersive X-ray spectroscopy (EDS) system.

A transmission electron microscope TECNAI G2 F20 operating at 200 kV was employed for TEM characterization. TEM foils were prepared by mechanical grinding the samples with SiC paper down to a thickness of ~100µm. Then they were electro-polished in a solution of 20% perchloric acid in ethanol, at room temperature, using a voltage of 60V. The output current as measured as 0.6 A.

High-Energy X-Ray Diffraction: High energy X-ray diffraction (HEXRD) measurements were conducted to identify the phase constitution and lattice parameters at the P07beam line of the synchrotron radiation facility PETRA III by the Helmholtz-Zentrum Geesthacht at the Deutsches Elektronen-Synchrotron (DESY) in Hamburg/Germany. The X-ray beam had a cross section of 1x1 mm^2 and a photon energy of 87.1 keV (0.14235 Å).

Thermal analysis: thermal analysis of the sample in the aged condition was performed using a differential scanning calorimetry (DSC) Netzsch 404 under an argon flow atmosphere of ~ 1bar. The samples were heated up to 1000 °C with a constant heating rate of 10 °C/min.

Interstitials Analysis: the concentration of nitrogen, oxygen, and carbon in the samples was measured by the combustion method using the Leco TCH 600 and LECO CS 230 analyzers.

Hardness curve: Samples from the cold-rolled sheets were solution-treated at 1200 °C for 1h and aged at 750 °C for 0.5, 2, 4, 10, 25, 50, 100, and 200h. All samples were quenched to room temperature into water. For heat-treating, the samples were wrapped in stainless steel foils to reduce the superficial oxidation. The samples were metallography prepared using an automated grinding and polishing LECO PX500 system. The Vickers hardness as a function of aging time was measured at room temperature using a Leco AMH55 micro indentation hardness testing system following the ASTM-E384 standard [37]. Sixteen measurements were made on each sample. A load of 500g and a dwell time of 10 s were used during the tests.

Tensile tests: Tensile test specimens with geometry shown in Figure 4.3 were cut from the cold rolled sheets by electrical discharge machining (EDM) with their longitudinal axes parallel to the rolling direction. The specimens were given a final solution-treatment at 1200°C for 1h, quenched into water, and aged for

100h at 750 °C. This aging time was determined based on hardness measurements. Following 100 hours of aging, all samples were found to have reached the peak aging condition. Tensile tests were performed at room temperature, 650, 750 and 850 °C in a Material Testing System (MTS) Landmark® Servohydraulic Test System at strain rate of 10^{-3} s^{-1}. The samples were induction heated to the target temperatures using a Ultraflex Power Technologies SM-5/200 induction heating system. A high temperature contact extensometer, manufactured by Epsilon Technology corp, model 3648, was used for strain measurements. Triplicate tests were performed in each temperature. The yield strength of the alloys was determined as the stress at which 0.2% plastic strain occurs, often called 0.2% offset yield strength.

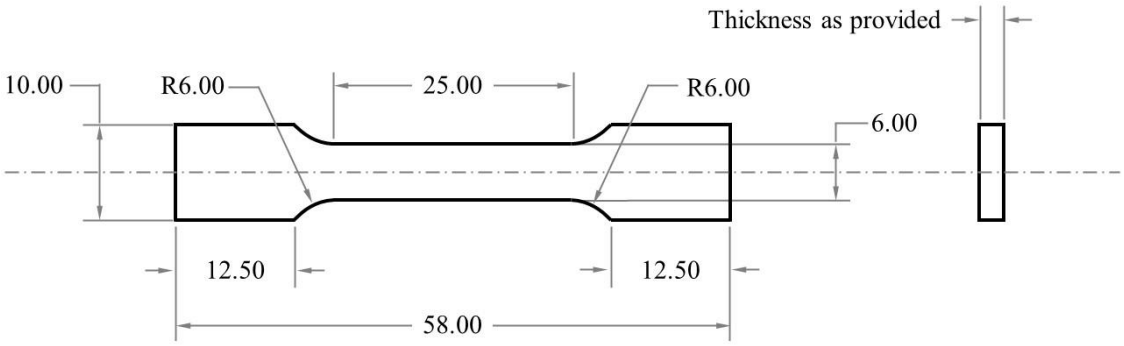

Figure 4.3: Specimen geometry used for tensile test in this work. All dimensions are reported in millimeters.

5 RESULTS AND DISCUSSION

5.1 1st Method

Throughout the section 4.1, the results solely of the alloy designed using the first approach are presented.

Figure 5.1a shows the result of thermodynamic calculations for $Cr_{29.7}Co_{29.7}Ni_{35.4}Al_{4.0}Ti_{1.2}$ (at. %) alloy, where the molar fraction of the stable phases is plotted as a function of temperature. At high temperatures, only the FCC phase is stable, whereas an FCC+$L1_2$ field can be observed between ~705-880°C. Within this temperature interval, the FCC phase presents a highly concentrated Cr-Co-Ni composition, as shown in Figure 5.1 b.

Figure 5.2 presents an optical micrograph of the designed alloy after aging treatment for 166h at 850 °C followed by water quenching. An equiaxed grain structure with annealing twins can be seen. The mean intercept length ($\langle l \rangle$) in the solution-treated and aged conditions were determined to be ~70 µm. Inclusions, which appear as small dark spots at lower magnifications, show a polygonal morphology and an orange color at higher magnifications, as can be observed inset in Figure 5.2. This color and morphology are typically observed in TiN inclusions in conventional superalloys [93].

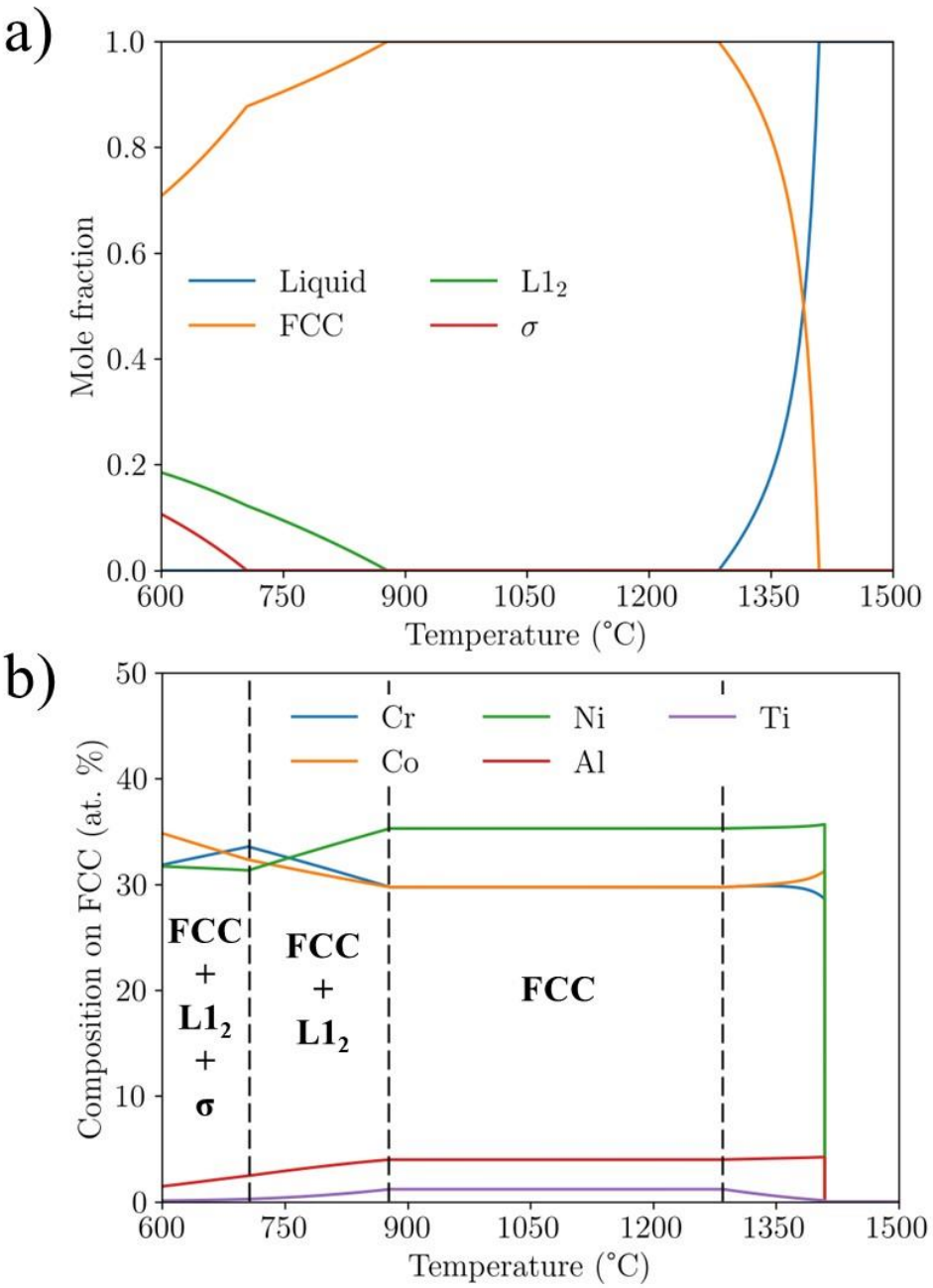

Figure 5.1: Results of the thermodynamic calculation for the $Cr_{29.7}Co_{29.7}Ni_{35.4}Al_{4.0}Ti_{1.2}$ alloy displaying a) the mole fraction of the equilibrium phases as a function of temperature; b) the equilibrium composition of the FCC phase as a function of temperature. The calculations were performed using the CALPHAD method via software Pandat™ and PanHEA2020 database.

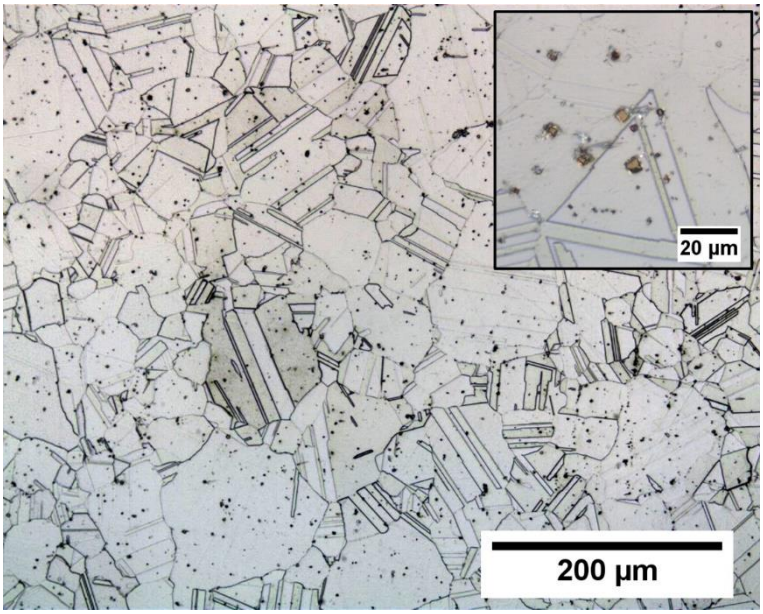

Figure 5.2: Optical micrograph of the Cr-Co-Ni-Al-Ti alloy after chemical etching using aqua regia (3HCl + 1 HNO3). The inset figure shows the small dark spots at higher magnifications.

An SEM image formed with backscattered electrons (BSE) of the Cr-Co-Ni-Al-Ti alloy in the aged condition is shown in Figure 5.3. The average and standard deviation of EDS measurements in five different regions of matrix+precipitates and inclusions are also presented in this figure. The EDS results indicate that the alloy composition was close to the nominal one ($Cr_{29.6}Co_{29.6}Ni_{35.2}Al_{4.0}Ti_{1.5}$). The highest deviation occurs to titanium, most likely because the inclusions are Ti-rich, as shown by EDS analyses. Their orange color in OM micrographs [93] plus the EDS measurements indicate a titanium nitride inclusion.

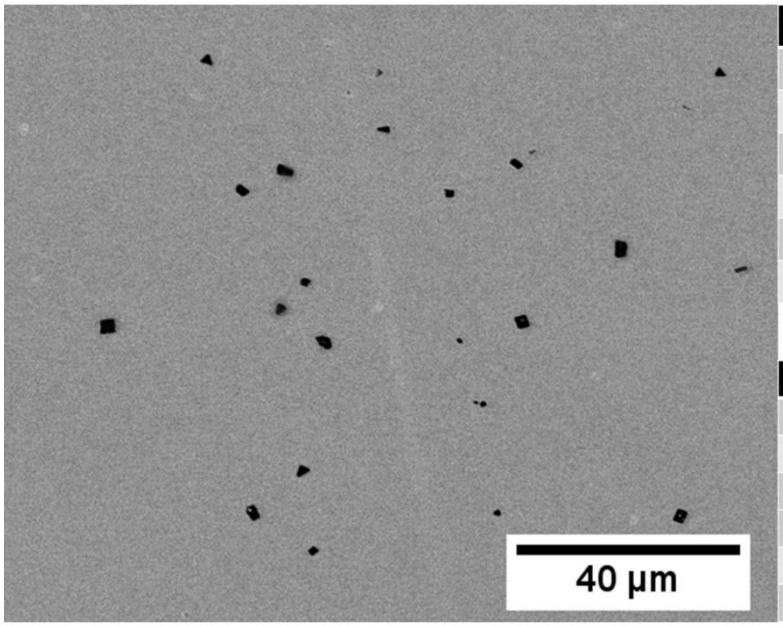

Matrix + Precipitates	
Element	µ±σ (%at.)
Cr	29.0 ± 0.2
Co	30.0 ± 0.3
Ni	36.2 ± 0.1
Al	3.6 ± 0.2
Ti	1.2 ± 0.0

Inclusions	
Element	µ±σ (%at.)
N	35.2 ± 2.5
Ti	54.0 ± 4.4
Ni	3.3 ± 1.5
Cr	4.0 ± 1.7
Co	2.7 ± 1.3

Figure 5.3: SEM image of the Cr-Co-Ni-Al-Ti alloy acquired using BSE detector. The darkest region is ascribed to TiN inclusion, and the gray area is related to the matrix plus precipitates. The average chemical composition was determined by EDS measurements taken in four different regions. It should be noted here that nitrogen (N) was quantified in the inclusions only to show qualitatively that this element is present since the quantification of light elements is inaccurate.

Quantitative analysis of the inclusions was performed at 30 different fields of view. The inclusion shows a mean equivalent planar diameter of 5.9±0.8 µm and a volume fraction of 0.6±0.1%. The main consequence of the inclusions in the current work is lowering the Ti content in the alloy, which impacts the $L1_2$ fraction. Figure 5.1 already presents the expected phase equilibria for the current alloy after this compositional adjustment. The inclusions are small, have a low volume fraction to contribute significantly to the hardness, and have no reason to change the growth kinetics of the $L1_2$ precipitates. From a mechanical property's standpoint, they might have some impact on the late stages of deformation, decreasing the ductility of the alloy [94]. To avoid such inclusions, the use of vacuum induction furnaces and higher purity materials is probably necessary.

The XRD analysis of solution-treated and solution-treated plus aged at 850 °C samples are shown in Figure 5.4. Since both phases have similar lattice parameters their 111, 200, and 220 diffraction peaks, around 2θ = 44, 51, and

75° respectively, are overlapped. Furthermore, due to background noise and low scattering factor, the superlattice diffraction peaks of $L1_2$ phase cannot be observed.

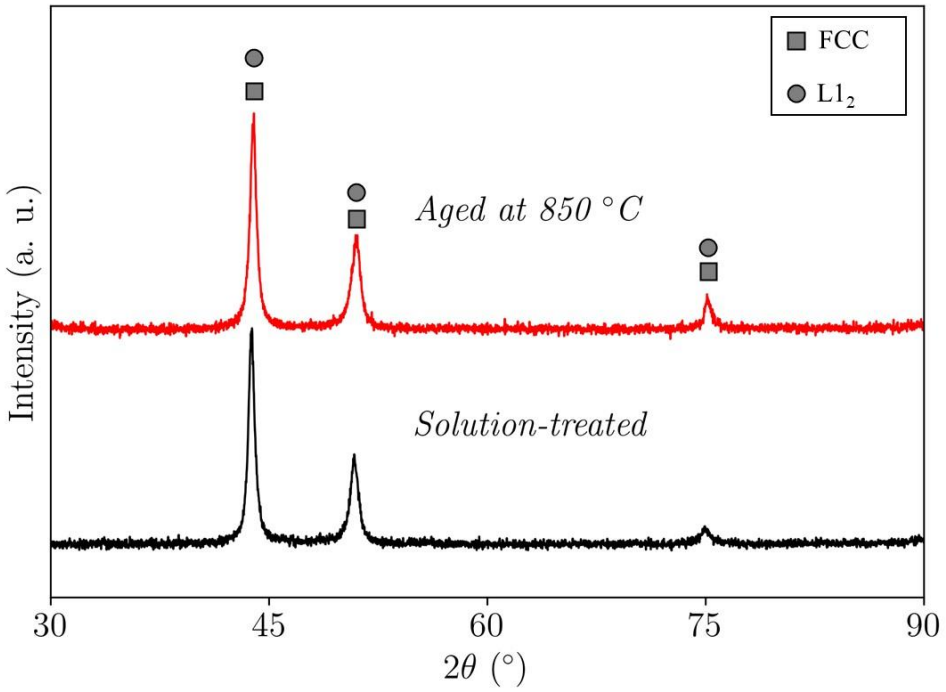

Figure 5.4: X-ray diffraction pattern of $Cr_{29.7}Co_{29.7}Ni_{35.4}Al_{4.0}Ti_{1.2}$ alloy in the solution-treated and solution-treated + aging at 850 °C for 10h conditions.

The DSC curve of $Cr_{29.7}Co_{29.7}Ni_{35.4}Al_{4.0}Ti_{1.2}$ alloy after an aging treatment at 850 °C can be seen in Figure 5.5. Through this analysis is possible to observe the dissolution reaction FCC+$L1_2$ → FCC. As indicated by the thermodynamic calculation presented in Figure 5.1, the volume fraction of the $L1_2$ phase decreases with the increase of temperature. In other words, this reaction starts at a low temperature and continues until the $L1_2$ phase be completely dissolved. The whole reaction is endothermic, but since it occurs over a wide temperature range, the endothermic peak is not well defined in a DSC curve. However, the end of this reaction can be easily detected through thermal analysis since it presents an inflection point followed by a baseline with a constant slope. From the curve in Figure 5.5, the $L1_2$ solvus temperature was determined to be ~895°C. This value is close to the ~880°C calculated by the CALPHAD method.

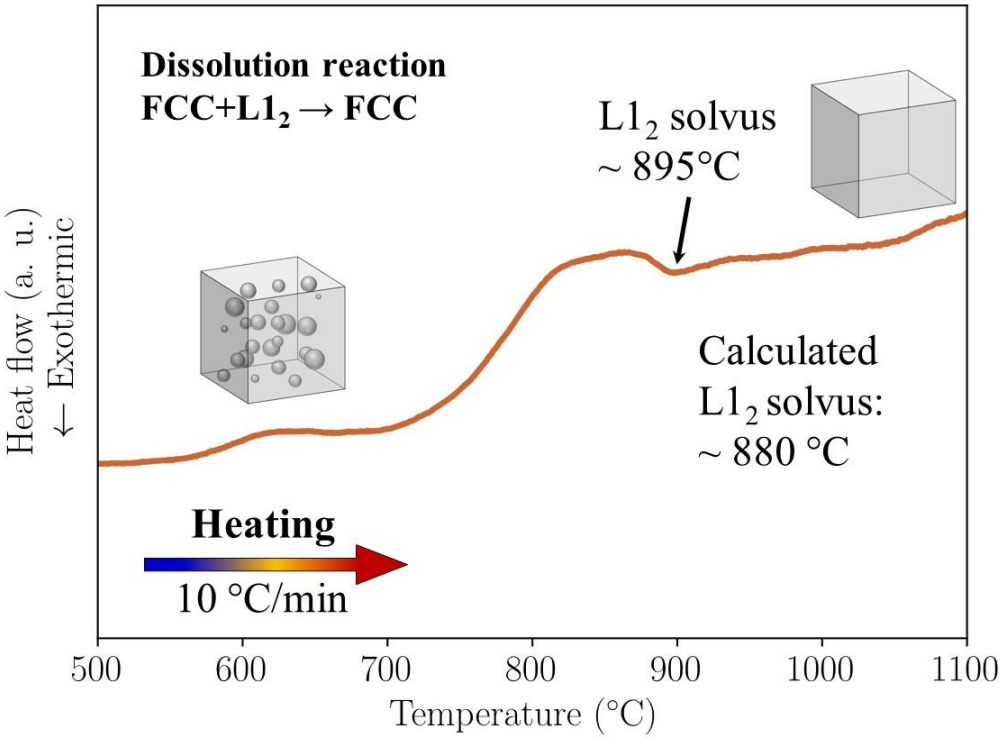

Figure 5.5: DSC curve of $Cr_{29.7}Co_{29.7}Ni_{35.4}Al_{4.0}Ti_{1.2}$ alloy after aging treatment at 850°C. A broad endothermic peak can be seen at 800-900 °C. The end of this peak was estimated as the solvus temperature, which matches the calculated solvus temperature using the PanHEA2020 thermodynamic database.

Precipitates were nearly spherical in all samples analyzed. Thus TEM-dark field images were acquired using superlattice reflection of the $L1_2$ phase close to arbitrary low index zone axis. Figure 5.6a-d shows the microstructure of $Cr_{29.7}Co_{29.7}Ni_{35.4}Al_{4.0}Ti_{1.2}$ alloy aged at 850°C for 2, 4, 10, and 166h, respectively. The mean precipitate radius and the standard deviation of the particle radius measurements are shown inset each image. A selected-area diffraction pattern (SADP) in the [001] zone axis of the alloy in the aged condition is shown in Figure 5.6e. A schematic illustration of the SADP is presented in Figure 5.6f, where the diffraction pattern is indexed. The same kind of pattern was observed in all conditions investigated, i.e., only reflections from FCC and $L1_2$ phases were present.

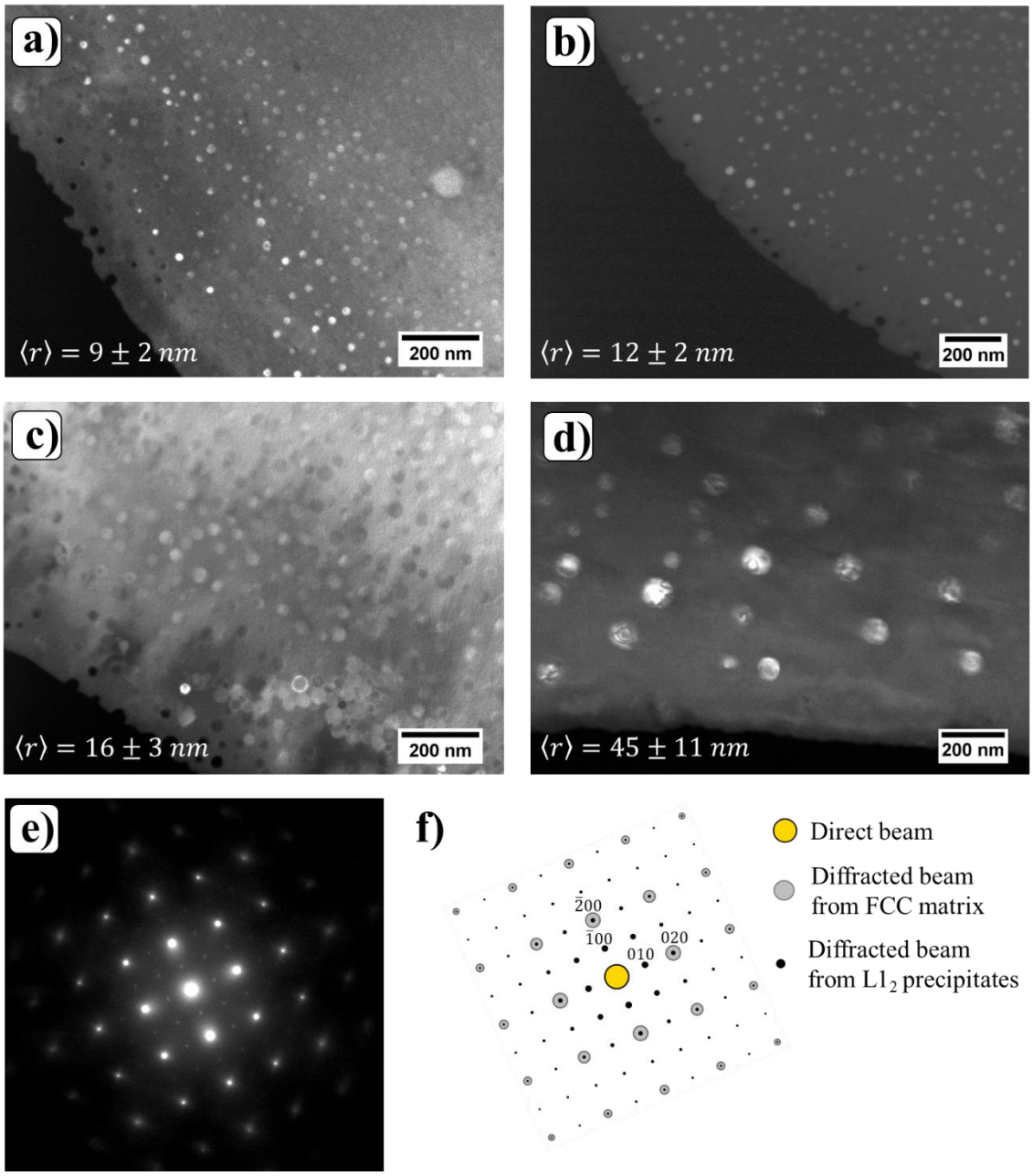

Figure 5.6: TEM dark-field images of $Cr_{29.7}Co_{29.7}Ni_{35.4}Al_{4.0}Ti_{1.2}$ alloy aged at 850°C for (a) 2, (b) 4, (c) 10 and (d)166h; (e) Selected area diffraction pattern showing the superlattice and matrix reflections; (f) schematic illustration of diffraction pattern. The dark field images were acquired using the superlattice reflection of $L1_2$ phase.

As can be noted in Figure 5.6 a-d, the $L1_2$ particles are uniformly distributed, and their morphology remains spherical during aging. The composition of the FCC and $L1_2$ phases calculated using the CALPHAD method

and measured by EDS on sample aged at 850°C for 166h are summarized at Table 5.1. It is worth mentioning that EDS analyses were performed only at this latter condition since the precipitates are much coarser and, therefore, the matrix contribution is minimized. This contribution is unavoidable when the precipitates are smaller than the sample thickness. It was observed that the absolute values of the chemical composition of FCC and $L1_2$ phases were close to those calculated by CALPHAD. Since chemical composition agrees, the lever rule principle in a two-phase field also guarantees that the volume fraction at that temperature is well predicted, this occurs given the alloy is in a two-phase tie-line, so the volume fraction of phases depends only on the composition of the two phases.

TEM foil thickness of sample aged for 166h was measured to be 39 ± 8 nm, yielding a volume percentage of 3.70 ± 1.6 %. Therefore, the volume fraction measured experimentally was similar, within experimental uncertainties, to the calculated one, 2.3%.

Table 5.1: Composition of FCC and $L1_2$ phases calculated using the CALPHAD method and measured by EDS for $Cr_{29.7}Co_{29.7}Ni_{35.4}Al_{4.0}Ti_{1.2}$ alloy aged at 850°C for 166h.

	FCC Phase		**$L1_2$ Phase**	
	EDS (at. %)	**Pandat (at. %)**	**EDS (at. %)**	**Pandat (at. %)**
Cr	34.4 ± 0.3	30.4	7.2 ± 0.2	2.1
Co	28.9 ± 0.3	30.1	10.5 ± 0.2	13.1
Ni	34.5 ± 0.3	34.7	63.8 ± 0.5	61.6
Al	1.5 ± 0.1	3.8	10.9 ± 0.1	12.4
Ti	0.7 ± 0.1	1.0	7.6 ± 0.2	10.8

The precipitation process can be divided into three stages: nucleation, growth, and coarsening [52]. Firstly, $L1_2$ precipitates nucleate on the supersaturated FCC matrix. Following nucleation, $L1_2$ particles grow by solute diffusion from the supersaturated matrix towards the precipitates. In the latter stage of precipitation, namely coarsening or Ostwald ripening, small particles shrink and disappear while large particles grow [49,50]. This competitive growth leads to an increase in the average size of the precipitates ($\langle r \rangle$) over time and a

concomitant decrease in the number of particles per unit volume in the system (N_V). This can be seen clearly in Figure 5.6. Since mechanical properties are related to these parameters, a fact of practical relevance is the knowledge of coarsening kinetics. Diffusion controlling theories, such as the classical theory of Lifshitz, Slyozov, and Wagner (LSW) [49,50], predict that the cube of mean precipitate radius varies linearly with time, as shown in Equation 5.1.

$$\langle r\rangle^3 - \langle r_0\rangle^3 = kt \tag{5.1}$$

where $\langle r\rangle$ is the average particle radius at time t and $\langle r_0\rangle$ is the average particle radius at the onset of coarsening. The coarsening rate constant, k , in the LSW theory is given by Equation 5.2:

$$k = \frac{8}{9}\frac{\sigma D c_e \Omega^2}{RT} \tag{5.2}$$

where σ is the precipitate-matrix interfacial energy, D is the coefficient of solute diffusion in the matrix, c_e is the equilibrium concentration of solute in the matrix, Ω is the molar volume of the precipitate, R is the gas constant, and T is the temperature.

Strictly speaking, LSW theory was developed to be applicable on binary-alloys and for a volume fraction of dispersed phase near to zero. Recently, new diffusion controlling coarsening models were developed for non-diluted multicomponent systems [46,95]. The coarsening kinetic equation in these new theories also follows the cube dependence of mean precipitate radius with time as indicated by Equation 5.1.

In the cases where interface or diffusion through the interface controls the coarsening, some theories have determined that the square of the mean precipitate radius is proportional to the time [48,50].

During quantitative analysis on projected images, care must be taken due to the difference between the average spatial precipitate radius ($\langle r\rangle$) and the average projected precipitate radius ($\langle r\rangle_{proj.}$), which is measured experimentally by TEM. This occurs due to truncation of particles by foil surface and overlapping among particles on the projected image. Considering only the former situation,

$\langle r \rangle_{proj.} \leq \langle r \rangle$. On the other hand, $\langle r \rangle_{proj.} \geq \langle r \rangle$ when only the overlapping of particles is assumed. Since no indication of overlapping was observed on all samples analyzed in this work, the main statistical error might be assigned to the truncation of particles. As demonstrated by Goldsmith [96], for a monodisperse system of spherical particles of radius r, when only the truncation is considered, $\langle r \rangle_{proj.}$ and r are related by Equation 5.3:

$$\langle r \rangle_{proj.} = \left(\frac{\pi/2\, r + t}{2r + t} \right) r \tag{5.3}$$

Thus, the correction of particle radius becomes more critical as the ratio r/t increases. In the present work, considering a foil thickness of ~40 nm, and that r can be approximate by $\langle r \rangle$, the mean precipitate radius changes from 38 nm to 45 nm after correction in the worst case, i.e., for the largest aging time. This value is equivalent to a relative error of 15%. For the other aging conditions, the relative error is ≤10%. Furthermore, when calculating the coarsening rate constant by fitting the experimental data to Equation 5.1, samples aged for longer times have a greater impact on the determination of slope by the least square method since $k \propto \langle r \rangle^3$. Therefore, the correction was applied only for sample aged for 166h, and the measurement of foil thickness in the other conditions was not considered a critical point for determining the coarsening rate constant.

Linearization of Equation 5.1 and fitting of the experimental data yields a rate constant of $k = 5.56 \times 10^{-10} m/s^{1/3}$ ($1.72 \times 10^{-28} m^3/s$). The goodness of fit ($r^2$) is shown inset in the Figure 5.7. The coarsening rate constant of traditional wrought superalloys and non-commercial multi-principal precipitation hardening alloys extracted from literature are shown in Figure 5.8. All alloys were aged at temperatures close to that used in the present work, 850 °C. The value of k for the $Cr_{29.7}Co_{29.7}Ni_{35.4}Al_{4.0}Ti_{1.2}$ alloy is smaller than all alloys analyzed.

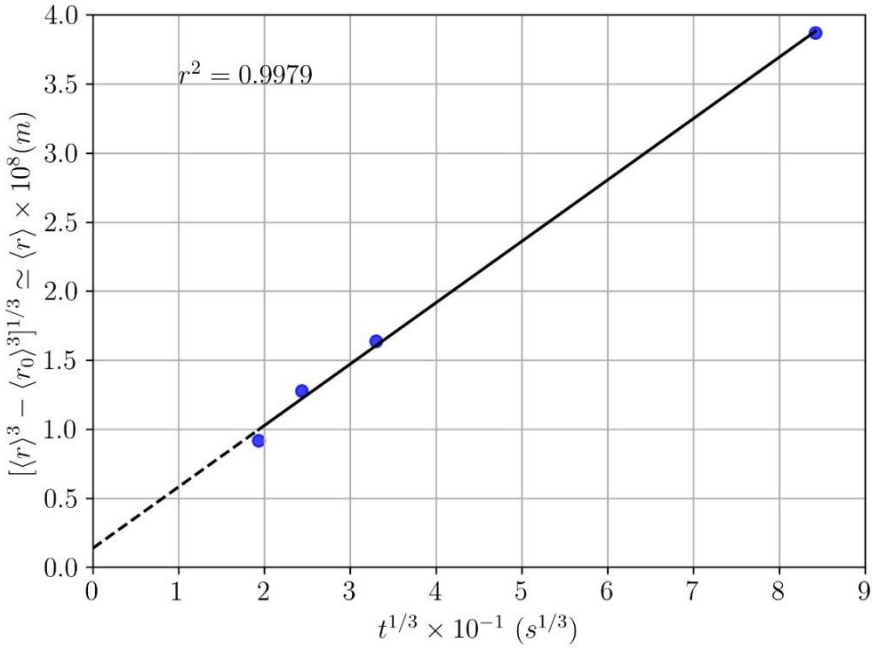

Figure 5.7: Fitting of the cube of mean precipitate radius, $\langle r\rangle^3$, versus aging time for $Cr_{29.7}Co_{29.7}Ni_{35.4}Al_{4.0}Ti_{1.2}$ alloy aged at 850 °C.

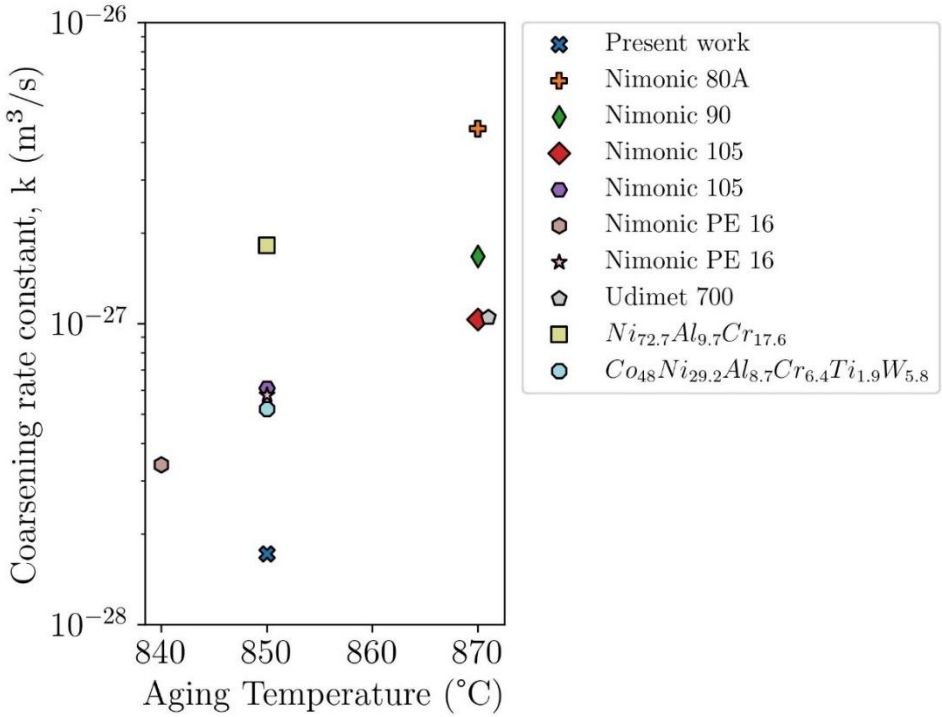

Figure 5.8: Coarsening rate constant of $Cr_{29.7}Co_{29.7}Ni_{35.4}Al_{4.0}Ti_{1.2}$ alloy, traditional wrought superalloys, and non-commercial alloys extracted from literature [97–103].

Besides the coarsening kinetics, the particle size distribution (PSD) is also of great relevance for material properties. During coarsening, the particle size distribution (PSD) of normalized particles radius, $h(\rho = r/r_c)$, does not change with time, i.e., the PSD is self-similar. The probability density function (PDF) of the PSD predicted by the theory of LSW is given by Equation 5.4 [49,50].

$$G_{LSW}\left(\rho = \frac{r}{r_c}\right) = \begin{cases} \frac{4}{9}\rho^2 \left(\frac{3}{3+\rho}\right)^{\frac{7}{3}} \left(\frac{3/2}{3/2-\rho}\right)^{\frac{11}{3}} \exp\left(-\frac{\rho}{3/2-\rho}\right), & \rho < 3/2 \\ 0, & \rho \geq 3/2 \end{cases} \quad (5.4)$$

Histograms of experimental data and curves of the probability density function of the PDS predicted by the theory of LSW are shown in Figure 5.9 a-d. The mean particle size in each condition is indicated on the upper-left corner of each histogram. Since the PSD is self-similar, a cumulative histogram of scaled-particle sizes is also shown in Figure 5.9 e.

The PSD shows a good correlation with LSW theory, but a few particles with scaled-size large than $\rho_{max} > 1.5$ were observed, in contradiction with the maximum allowable value predicted by LSW. Strictly speaking, the theory of LSW is applicable only when $f \to 0$, but how small f must be is not precisely defined. Theories that account for the effect of volume fraction on particle size distribution predict that PSD should broaden as f increase. For instance, for a volume fraction of 3%, Ardell's theory for binary alloys [47] predicts that $\rho_{max} = 1.79$, while Wang's theory [46] for multicomponent alloys predicts $\rho_{max} = 1.60$.

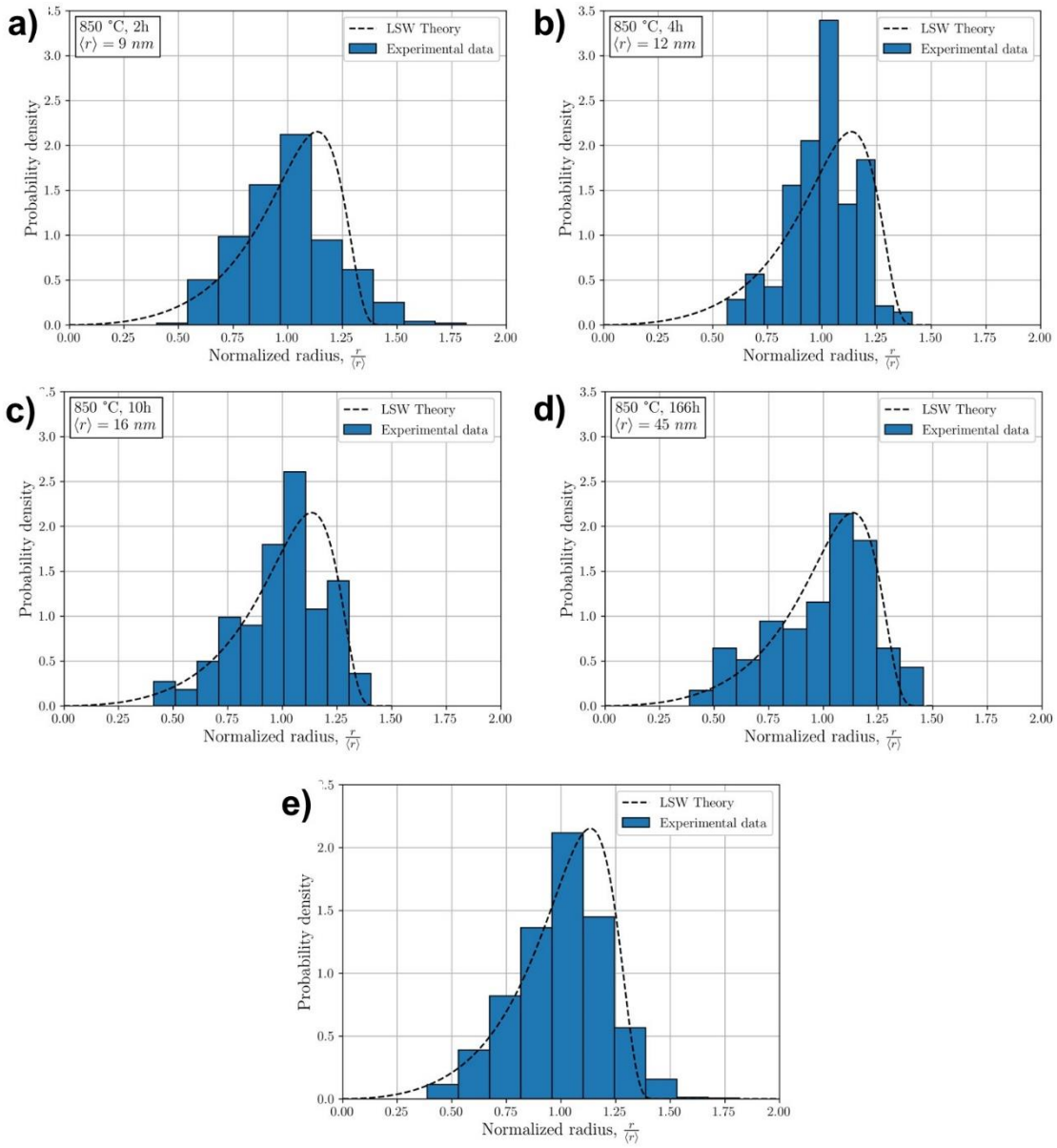

Figure 5.9: Histograms of experimental data and curves of PDF predicted by LSW theory for the current MPEA.

The Vickers hardness of $Cr_{29.7}Co_{29.7}Ni_{35.4}Al_{4.0}Ti_{1.2}$ alloy at solution-treated condition was 178±3 HV 0.5. The evolution of the microhardness as a function of aging time at 850 °C is shown in Figure 5.10. The uncertainties are expressed as the 95% confidence interval of the measurements. As can be noted, the hardness values remain relatively constant in ~284 HV 0.5 between the aging time of 10 and 48h.

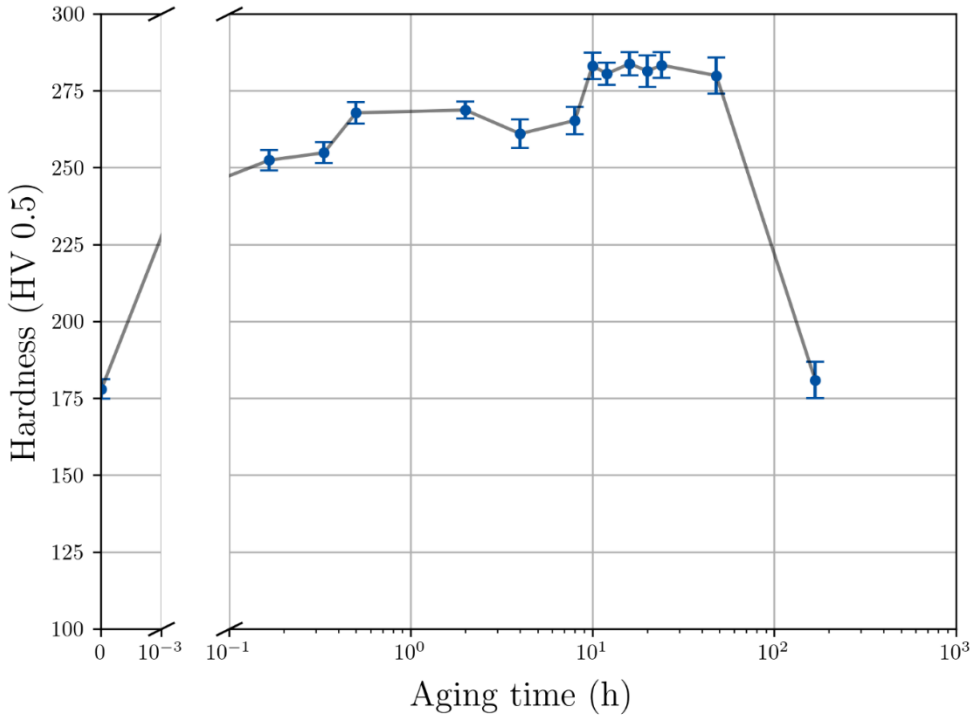

Figure 5.10: Vickers microhardness as a function of aging time at 850 °C for $Cr_{29.7}Co_{29.7}Ni_{35.4}Al_{4.0}Ti_{1.2}$ alloy.

The hardness of $Cr_{29.7}Co_{29.7}Ni_{35.4}Al_{4.0}Ti_{1.2}$ alloy in the solution-treated condition was 178±3 HV. For the same grain size, $\langle d \rangle = 105\ \mu m$, the hardness predicted for $Cr_{33}Co_{33}Ni_{33}$ alloy [104] is 153 HV. This hardness difference can be attributed to an increase in the solid solution component due presence of Al and Ti atoms, which strains the lattice locally and cause a local change on elastic modulus [15,23,24,105].

From here on, the modeling of yield stress of FCC HEAs containing nanometric ordered particles is proposed. Classical grain boundary is coupled with Varvenne's model to predict all the independent contributions to the yield strength of the $Cr_{29.7}Co_{29.7}$ $Ni_{35.4}Al_{4.0}Ti_{1.2}$ (at. %) alloy. As will be shown later, the results can be easily extrapolated to other alloys of the Cr-Co-Ni-Al-Ti system.

The yield strength of a polycrystalline alloy (σ_{ys}) was considered to be given by Equation 5.5:

$$\sigma_{ys} = \sigma_{gs} + \sigma_{ss} + \sigma_{p}. \qquad (5.5)$$

where σ_{gs}, σ_{ss}, and σ_p are the grain size, solid solution, and precipitation hardening contributions to the yield strength, respectively.

The grain size contribution is established by Equation 5.6:

$$\sigma_{gs} = \frac{k}{\sqrt{d}}. \tag{5.6}$$

where *d* is the mean grain size and *k*, also called locking parameter, is a composition and temperature dependent constant [106]. For instance, the composition effect on *k* can be assessed from the work of Yoshida et. al.[107], which different HEAs alloys were processed similarly and tested at room temperature. While $Co_{20}(CrNi)_{80}$ alloy showed a locking parameter of $168\ \mathrm{MPa}\cdot\sqrt{\mu\mathrm{m}}$, the FeMnNi alloy had a value of $381\ \mathrm{MPa}\cdot\sqrt{\mu\mathrm{m}}$. The influence of temperature on the locking parameter can be analyzed from another work [108]. The *k* value of CrMnFeCoNi alloy decreased from 645 to 306 $\mathrm{MPa}\cdot\sqrt{\mu\mathrm{m}}$ when the testing temperature changed from -196 to 600 °C. These results are in good agreement with those reported for the same alloy by [29], showing that *k* is also a function of temperature.

In the present work, the adopted locking parameter of the $Cr_{29.7}Co_{29.7}Ni_{35.4}Al_{4.0}Ti_{1.2}$ alloy, in both supersaturated and aged condition, was from the similar $(CrCoNi)_{97}Al_3$ (at. %) alloy, i.e., 665 $\mathrm{MPa}\cdot\sqrt{\mu\mathrm{m}}$ [109]. The mean grain size (*d*) was estimated from the mean intercept length, using the stereological relationships $d = 1.571\bar{l}$ [110,111].

The solid solution hardening contribution was modeled using Varvennes's model. For sake of clarity, Equations 3.1-3.4 are repeated here for the polycrystalline case.

$$\tau_{y0} = 0.051\alpha^{-\frac{1}{3}}\mu\left(\frac{1+\nu}{1-\nu}\right)f_1(w_c)\left(\frac{\sum_{i=1}^{n} c_i\Delta\bar{V}_i^2}{b^6}\right)^{\frac{2}{3}}, \tag{3.1}$$

$$\Delta E_b = 0.274\alpha^{\frac{1}{3}}\mu b^3\left(\frac{1+\nu}{1-\nu}\right)^{\frac{2}{3}} f_2(w_c)\left[\frac{\sum_{i=1}^{n} c_i\Delta\bar{V}_i^2}{b^6}\right]^{\frac{1}{3}}, \tag{3.2}$$

$$\sigma_{ss}(T,\dot{\varepsilon}) = M\tau_{ss,0}\left[1-\left(\frac{k_B T}{\Delta E_b}\ln\frac{\dot{\varepsilon}_0}{\dot{\varepsilon}}\right)^{\frac{2}{3}}\right]. \qquad \frac{\sigma_{ss}}{M\tau_{y,0}} < 0.5 \tag{3.3}$$

$$\sigma_{ss}(T,\dot{\varepsilon}) = M\tau_{ss,0}\exp\left(-\frac{1}{0.51}\frac{k_B T}{\Delta E_b}\ln\frac{\dot{\varepsilon}_0}{\dot{\varepsilon}}\right). \qquad \frac{\sigma_{SS}}{M\tau_{y,0}} \geq 0.5 \qquad (3.4)$$

As can be noted, the elastic constants of the alloy are some of the input variables in the latter model. For estimating the elastic moduli of $Cr_{29.7}Co_{29.7}Ni_{35.4}Al_{4.0}Ti_{1.2}$ alloy, the composition of the FCC phase in the solution treated and the aged condition were firstly approximated as $(CrCoNi)_{95.7}Al_{4.3}$ and $(CrCoNi)_{98.5}Al_{1.5}$, respectively. Then, the shear modulus and Poisson's ratio of these alloys were estimated using the empirical relationships proposed by Varvenne [112] in the cases of dilute doping HEAs of Cr-Co-Ni-Mn-Fe family with Al, i.e. $G = G(T)(1 - 1.51c_{Al})$ and $\nu = \nu\ (T) + 0.2c_{Al}$, where $G(T)$ and $\nu(T)$ are the shear modulus and Poisson's ratio at temperature T of the base HEA that was dopped with Al. In this work, the CrCoNi alloy was the base HEA for the calculation of the elastic properties. The values of *G* and *v* at room temperature for this ternary alloy were determined by Wu et. al.[25] as 87 GPa and 0.3, respectively. The final elastic constants for the alloy in the different conditions are summarized in Table 5.2. The effect of Ti in the elastic properties of Cr-Mn-Fe-Co-Ni alloys has not been reported in the literature to the best of our knowledge. However, since this element is very diluted in the alloy of the present work, it is reasonable to assume that its effect on elastic properties is minimal.

Table 5.2: Elastic constant calculated for $(CrCoNi)_{95.7}Al_{4.3}$ and $(CrCoNi)_{98.5}Al_{1.5}$ alloys using empirical relationships proposed by Varvenne [112].

Condition	**Approximated Alloy**	**G (GPa)**	**ν**	**E=2G(1+ν) (GPa)**
Homogenized	$(CrCoNi)_{95.7}Al_{4.3}$	81	0.31	212
Aged	$(CrCoNi)_{98.5}Al_{1.5}$	85	0.30	221

The calculated Young's modulus for the alloy in the homogenized condition is in good agreement with that determined from tensile tests, shown later in this work (E=204 GPa).

As discussed in literature review chapter, the Effective Atomic Radii for Strength (EARS) methodology [24] has already proved to be a valuable tool for estimating the atomic volume of elements (V_n) in an FCC solid solution. Here, the atomic radii reported previously [24] is reassessed using the critical resolved shear stress (CRSS) data of single crystal alloys [113–116] and the intercept value of the Hall-Petch equation fitted to experimental data of polycrystalline alloys [107,109,117]. In this way, the grain size contribution to the yield strength can be disregarded. The magnitude of this contribution is often an issue when analyzing polycrystalline alloys data due to uncertainty of the locking parameter in most cases. Furthermore, the aforementioned consideration is an excellent assumption for FCC single-phase alloys in recrystallized condition, where there is no second-phase particle contribution, and the work-hardening strengthening is negligible. In those cases of single crystal data, the CRSS was converted to polycrystalline yield strength using a Taylor factor for an untextured FCC polycrystal (M = 3.06). The data used in the EARS method are summarized in Table 5.3.

Table 5.3: Room temperature elastic constants and solid solution contribution to yield strength for several HEAs. The σ_{ss} component of polycrystalline alloys was considered as the intercept value of the Hall-Petch equation fitted to experimental data. The CRSS for single crystals alloys was converted to polycrystal data using

a Taylor factor (*M*) for an untextured FCC polycrystal (*M* = 3.06), i.e., $\sigma_{ss} = M \times \tau_{ss}$.

Alloy composition (at. %)	Shear modulus, G (GPa)	Poisson's ratio, v	Experimental σ_{ss} (MPa)
$Ni_{60}Co_{40}$	82[b]	0.29[b]	52 [118]
FeCoNi	60[a]	0.35[a]	63 [107]
MnFeNi	73[a]	0.24[a]	119 [107]
MnCoNi	77[a]	0.23[a]	86 [107]
$(NiCo)_{95}Cr_5$	84[b]	0.29[b]	30 [107]
$(NiCo)_{80}Cr_{20}$	86[b]	0.30[b]	167 [107]
$(NiCr)_{80}Co_{20}$	86[b]	0.31[b]	280 [107]
CrCoNi	87[a]	0.30[a]	211[sx] [113]
$(CrCoNi)_{97}Al_3$	83[c]	0.31[c]	223 [109]
MnFeCoNi	77[a]	0.22[a]	108 [107]
CrFeCoNi	84 [a]	0.28 [a]	128[sx] [116]
$(CrFeCoNi)_{96}Al_4$	79[c]	0.29[c]	131 [117]
$(CrFeCoNi)_{93}Al_7$	75[c]	0.29[c]	185[sx] [114]
CrCoFeMnNi	80[a]	0.26[a]	135[sx] [115]

[a] Measured by Wu et. al.[25];
[b] Values calculated using the equations $G = 76c_{Ni} + 92c_{Co} + 93c_{Cr}$ and $\nu = 0.31c_{Ni} + 0.27c_{Co} + 0.32c_{Cr}$. These equations were derived using the rule of mixture ($\sum_n c_n G_n$ and $\sum_n c_n \nu_n$, respectively) and the elastic constants for Ni, CoNi, and CrCoNi alloys reported by Wu et. al. [25];
[c] Elastic constants calculated using the empirical relationship proposed by Varvenne et. al. [31], where $G = G(T)(1 - 1.51c_{Al})$ and $\nu = \nu(T) + 0.2c_{Al}$. The values of the elastic constants of the base HEAs, $G(T)$ and $\nu(T)$, were measured by Wu et. al. [25]. Details are given in text.
[sx] Single crystal data.

The output results from the EARS method are shown in Table 5.4. For comparison, this table also displays the “Pure metal atomic volume” calculated from the lattice parameter of the elements in their original structure [42], the “Okamoto atomic volume” estimated using a first-principle method [41], the “Solution atomic volume” calculated by Varvenne et. al. [15,112] using solid

solution lattice parameter data, and “Effective Atomic Radii for Strength (EARS)” calculated by Coury et. al. in previous work [24]. The latter values were converted to atomic volume using the relationship $V_n = 4\sqrt{2}r_n^3$. Due to the lack of experimental data reporting the effect of Ti on the CRSS of the Cr-Mn-Fe-Co-Ni alloys family, the atomic volume of this element was calculated from the lattice parameter of Ni-Ti solid solution data [42]. It was estimated as 14.48 Å^3.

Table 5.4: Atomic volume calculated by different approaches: using the lattice parameter data of the elements in their original structure (pure metal atomic volume) [42], determined through ab initio method by Okamoto et. al. (Okamoto atomic volume) [41], calculated using EARS method in previous work (EARS atomic volume – previous work) [24], estimated utilizing solid solution lattice parameter data (Solution atomic volume) [15,112], calculated using the EARS method in this work (EARS atomic volume – this work).

Element	**Pure metal atomic volume (Å^3)** [42]	**Okamoto atomic volume (Å^3)** [41]	**EARS atomic volume (Å^3) – previous work** [24]	**Solution atomic volume (Å^3)** [15,112]	**EARS atomic volume(Å^3) – this work**
Ni	10.94	10.76	10.44	10.94	10.94
Cr	11.02	11.56	12.45	12.27	12.86
Co	11.08	10.25	10.86	11.12	11.52
Fe	10.82	10.25	11.82	12.09	12.18
Mn	12.59	10.66	12.26	12.60	12.66
Al	16.60	-	-	14.00	13.52
Ti	18.16	-	-	14.48[a]	-

[a] Calculated in this work using the lattice parameter of Ni-Ti solid solution extracted from [42].

The difference between the atomic volume calculated by the distinct approaches is of only a few Å^3. However, these small differences can have a large impact on the magnitude of the solid solution strengthening component, as shown in Figure 5.11. This is justified by the power-law dependence between σ_{SS} and V_n, implicitly expressed in the model equations.

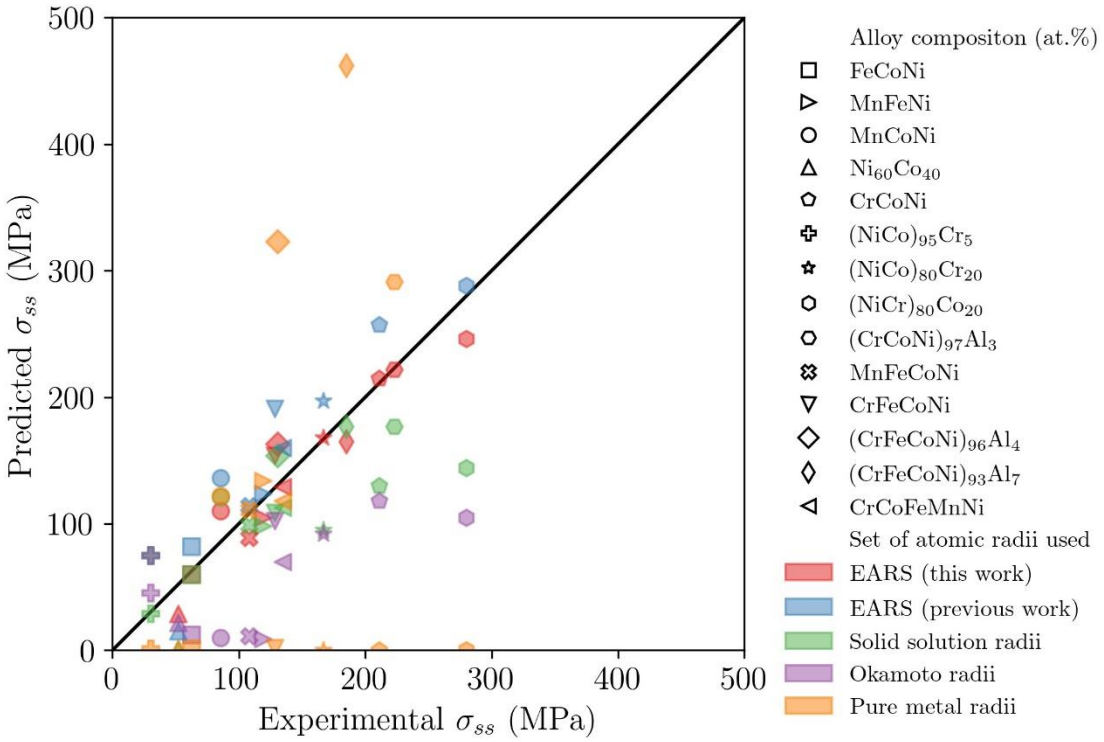

Figure 5.11: Predicted versus experimental (reported in Table 5.3) solid solution contribution to yield strength. The different sets of atomic radii used in the calculations are detailed in Table 4.

A good agreement between the experimental and the theoretical values of σ_{SS} is achieved when the atomic volume is estimated using the EARS and solid-solution methods, as can be observed in Figure 5.11. However, the atomic volume estimated by the former methodology in a previous work [24] tends to overpredict the solid solution contribution, whereas those calculated using the latter method tend to underestimate the solid solution contribution, mainly for those alloys with high chromium content. Among all the approaches analyzed, the σ_{SS} estimated using the EARS values calculated in this work has the smallest mean absolute error, only 18 MPa.

Using the value of solid solution atomic volume for Ti and those of EARS calculated in this work, the lattice parameter of a large number of FCC single phase HEAs were calculated and plotted versus experimental values extracted from literature [15,117,119–122]. The results are shown in Figure 5.12. The Vegard's law was assumed valid for the calculation of the lattice constants.

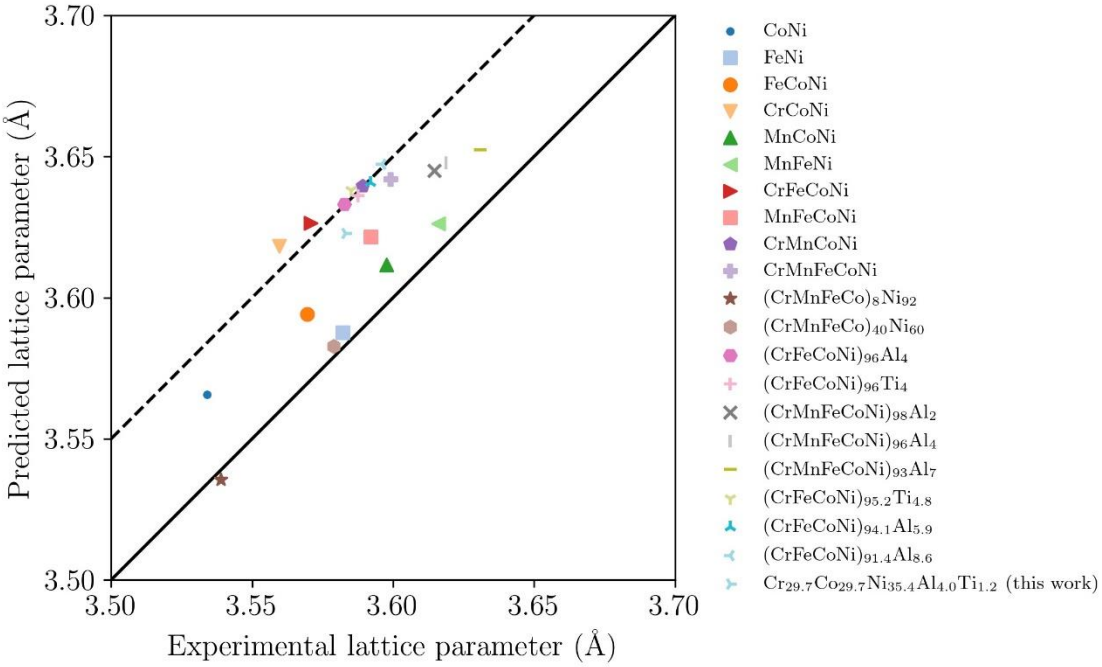

Figure 5.12: Room temperature lattice constant versus Vegard's law predictions for several HEAs. The experimental values were extracted from the literature [15,117,119–122], and the predicted lattice parameters were calculated using the EARS values estimated in this work given in Table 5.4.

Although for several alloys the lattice parameter is overestimated, the maximum absolute error is less than 0.05 Å in all cases. This indicates that EARS is also a valuable method for predicting the lattice parameter of single-phase FCC HEAs in the Cr-Mn-Fe-Co-Ni-Al-Ti system. As can be seen in Figure 5.12, the deviations are higher for the alloys with a high chromium content (over ~20%at.), in which the lattice parameter is overpredicted by ~0.045 Å in most alloys, as indicated by the dashed line in Figure 5.12. It is worth mentioning that Varvenne's model and Vegard's law assume an ideal solid solution, where the atoms are randomly distributed in the lattice sites. On the other hand, recent studies have reported the presence of chemical short-range order (SRO) in the Cr-Co-Ni alloys [123–125]. As indicated in [125], Ni-Ni and Cr-Co clusters are likely to form in the latter system. The effect of SRO on mechanical properties is still a controversial issue in the literature [126]. However, some degree of SRO may be one of the reasons for the linearity deviation in the lattice parameter of high chromium content HEAs.

Based on the previous findings, it is proposed the following empirical relationship to predict the room temperature lattice parameters of FCC alloys in the Cr-Mn-Fe-Co-Ni-Al-Ti system:

$$a = \sum_n c_n a_n + c_{Cr} c_{Co} a_{Cr-Co} \quad (5.7)$$

where c_n is the concentration of nth element in the alloy and a_n is a constant associated with each element. The latter constant is related to the atomic volume of the elements by $a_n = \sqrt[3]{4V_n}$, where V_n is the EARS atomic volume value of the nth element determined in this work. An additional term for accounting for Cr-Co interactions, namely a_{Cr-Co}, is also present in Equation 5.7. All the resulting coefficients are summarized in Table 5.5.

Table 5.5: Coefficients associated with each element to predict the room temperature lattice parameter of FCC alloys in the Cr-Mn-Fe-Co-Ni-Al-Ti system.

	Cr	**Mn**	**Fe**	**Co**	**Ni**	**Al**	**Ti**	**Cr-Co**
a_n (Å)	3.72	3.70	3.65	3.59	3.52	3.78	3.87	-0.61

The results of tensile tests in the different aging conditions for the $Cr_{29.7}Co_{29.7}Ni_{35.4}Al_{4.0}Ti_{1.2}$ are shown in Figure 5.13. The mean intercept length ($\bar{l}$) of the grains in the different aging conditions are reported in the first column of Table 5.6. All the samples presented similar grain sizes independently of aging time, which is not intuitive since the grains are expected to coarse as aging time increases. However, both the inclusions and the precipitates act as Zenner pinning sites, which inhibit grain growth during aging [64,127,128].

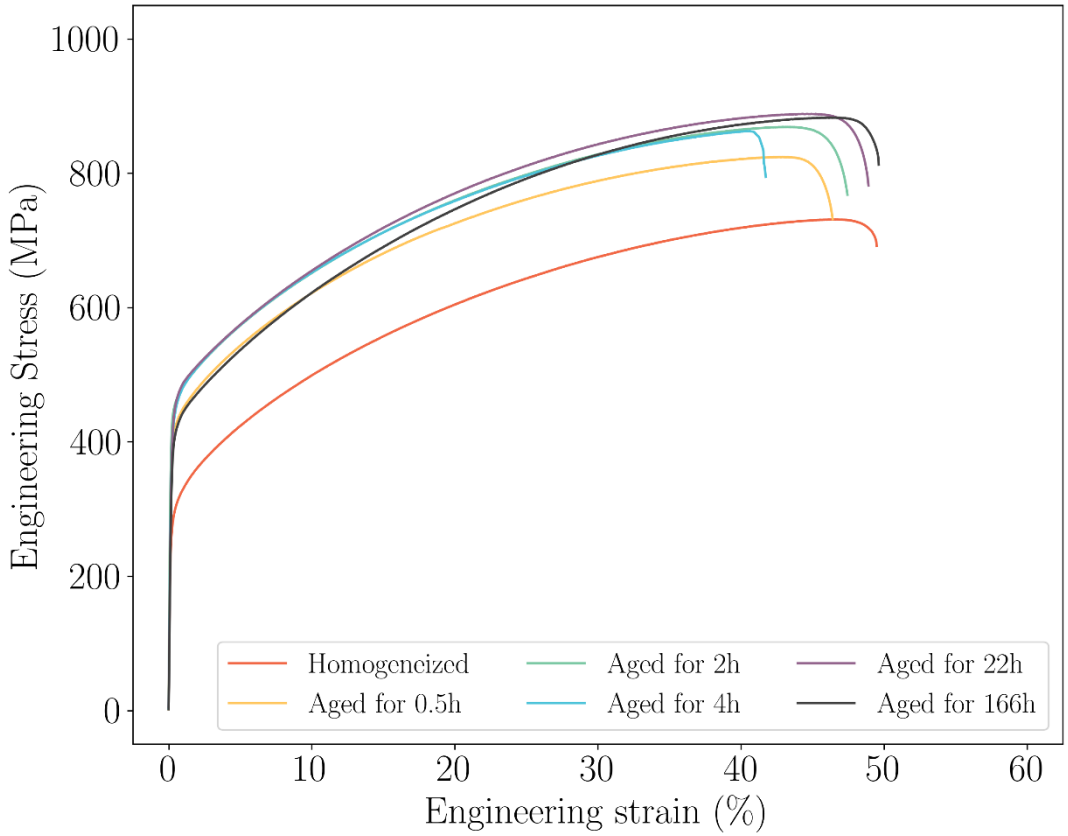

Figure 5.13: Tensile engineering stress-strain curves of $Cr_{29.7}Co_{29.7}Ni_{35.4}Al_{4.0}Ti_{1.2}$ alloy aged at 850 °C for different times.

The mean precipitate radius ($\bar{r}$) in each condition is shown in the second column of Table 5.6. The specimens aged for 0.5 and 22h had their precipitates radius calculated from experimentally determined coarsening rate constant reported previously ($k = 1.72 \times 10^{-28} \mathrm{m}^3/s$), in the other conditions $\bar{r}$ was measured from TEM micrographs.

During coarsening, the precipitate volume fraction and the composition of the equilibrium phases are kept nearly constant. Accordingly, the solid solution strengthening contribution to yield strength does not change in this late stage. As shown in Equations 3.1-3.4, σ_{ss} is basically a composition dependent parameter.

The mean experimental values of the yield strength (σ_{ys}) are summarized in Table 5.6. The sum of the calculated solid solution component (σ_{ss}) and grain size contribution (σ_{gs}) is in good agreement with the experimental results for homogenized alloy. It corroborates previous studies, which showed that

Varvenne model predicts well the solid solution contribution in the Cr-Co-Ni-Fe-Mn system [24], now also demonstrated for small additions of Ti and Al.

Table 5.6: Experimental determined data of mean intercept length ($\bar{l}$), mean precipitate radius ($\bar{r}$), and mean $\sigma_{0.2\%}$ yield strength for $Ni_{35.4}Cr_{29.7}Co_{29.7}Al_{4.0}Ti_{1.2}$ alloy aged at 850 °C for different times. The uncertainty of $\bar{l}$ and $\bar{r}$ are represented as standard deviations of the measurements. The calculated values for grain boundary and solid solution strengthening mechanisms are reported in columns σ_{gs} and σ_{ss}, respectively. The last column presents the precipitation hardening contribution for strength (σ_p), calculated by subtracting $\sigma_{ys} - \sigma_{gs} - \sigma_{ss}$.

	$\bar{l}$ (μm)	$\bar{r}$ (nm)	σ_{ys} (MPa)	σ_{gs} (MPa)	σ_{ss} (MPa)	σ_p (MPa)
Homogenized	78 ± 7	-	287	60	243	-
Aged for 0.5 h	55 ± 6	7	418	71	222	124
Aged for 2 h	71 ± 6	9 ± 2	445	63	222	159
Aged for 4 h	67 ± 3	12 ± 2	439	65	222	151
Aged for 22 h	69 ± 6	24	446	64	222	159
Aged for 166 h	58 ± 5	45 ± 11	413	69	222	121

Figure 5.14a shows the yield strength as a function of mean precipitate radius, where a classic aging response is followed. The predicted magnitude of each contribution to yield strength is detailed in Figure 5.14b.

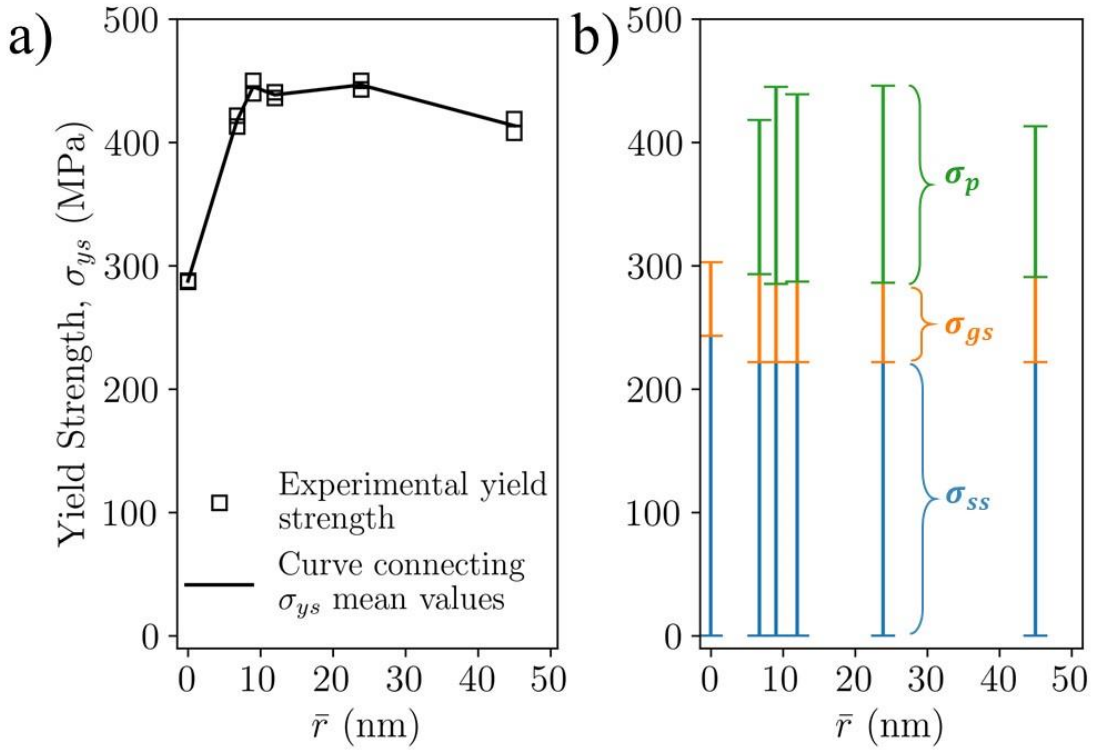

Figure 5.14: a) Yield strength of $Ni_{35.4}Cr_{29.7}Co_{29.7}Al_{4.0}Ti_{1.2}$ alloy as a function of mean precipitate radius; (b) magnitude of the strengthening mechanisms throughout the different aging conditions analyzed in this work.

As can be observed, the solid solution contribution is the dominant strengthening mechanism in all conditions evaluated. However, upon aging, an increment in the yield strength up to ~160MPa was observed compared to its counterpart in the homogenized condition. This corresponds to an increase of ~55% in σ_{ys}. As can be noted from the data in Table 5.6, this gain in strength can be attributed mainly to the precipitation of the nanometric ordered particles, demonstrating that precipitation hardening is also an effective strengthening mechanism that must be taken into consideration for optimizing the mechanical properties of HEA alloys.

In this 1st approach for designing precipitation-hardened high entropy alloys, the composition was not optimized to present a maximized precipitation hardening contribution. As theorized by Equation 3.22, this component depends heavily on the antiphase boundary energy and the volume fraction of precipitates.

When alloy strength is one of the primary concerns in designing new precipitation-hardened HEAs, the composition should be adjusted to have a good compromise between solid solution strengthening, volume fraction of precipitates, and a maximized antiphase boundary energy. Furthermore, additional precautions should be taken to avoid the formation of topologically closed packed (TCP) phases such as σ, μ, and Laves due to their detrimental effect on mechanical properties. In this context, the 2nd approach used in this work was developed.

5.2 2nd Method

Figure 5.15 shows the thermodynamic calculation for $Cr_{20}Co_{12.5}Ni_{60}Al_{2.5}Ti_5$, $Cr_{22.5}Co_{10}Ni_{60}Al_5Ti_{2.5}$, and $Cr_{20}Co_{17.5}Ni_{50}Al_{12}$ alloys displaying the molar fraction of equilibrium phases as a function of temperature.

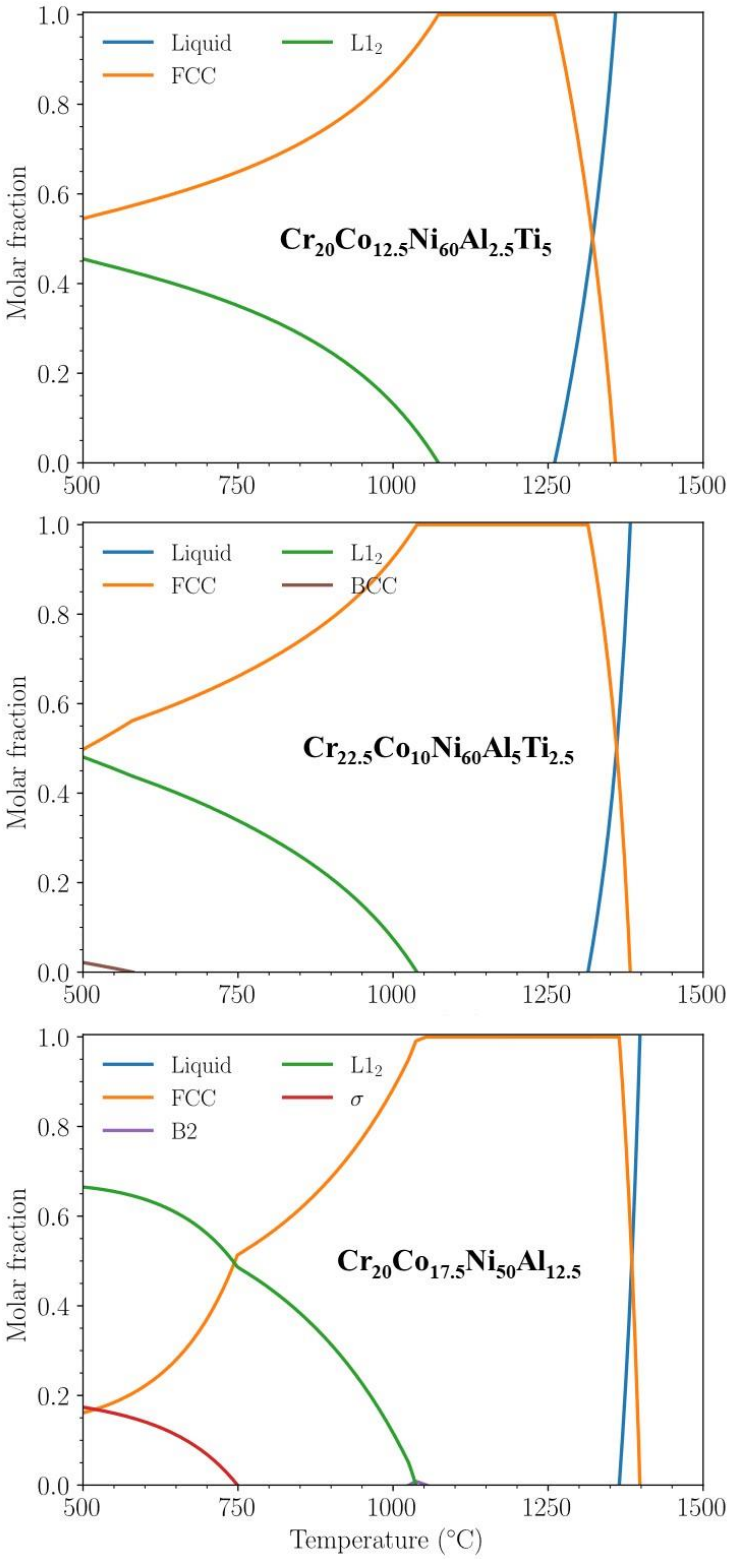

Figure 5.15: Thermodynamic calculation of $Cr_{20}Co_{12.5}Ni_{60}Al_{2.5}Ti_5$, $Cr_{22.5}Co_{10}Ni_{60}Al_5Ti_{2.5}$, and $Cr_{20}Co_{17.5}Ni_{50}Al_{12.5}$ alloys displaying the molar fraction of equilibrium phases as a function of temperature.

The as-cast cylindrical ingots of the three different alloys are shown in Figure 5.16. Representative microstructures of the alloys in the as-cast and homogenized conditions are shown in Figure 5.17. In all alloys, a dendritic microstructure is observed in the as-cast condition. The growth direction of primary dendrites arms is aligned to the expected growth direction. The micrographs of the homogenized samples, shown in the right column of Figure 5.17, indicates that the homogenization treatment was adequate to reduce the microsegregation in all alloys. During chemical etching, the regions around inclusion particles are preferentially etched (as shown later in the left column of Figure 5.18), which makes the light reflects in a diffuse manner in these locations. Therefore, the inclusions appear as dark spots at the lower magnification micrographs presented in Figure 5.17.

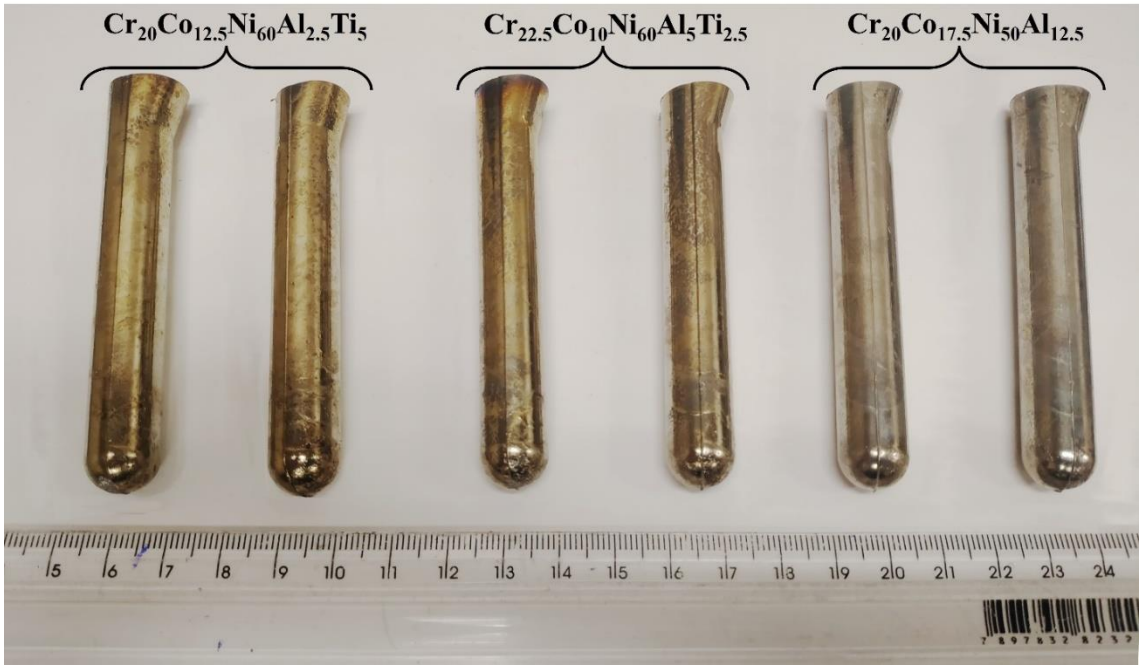

Figure 5.16: Ingots of $Cr_{20}Co_{12.5}Ni_{60}Al_{2.5}Ti_5$, $Cr_{22.5}Co_{10}Ni_{60}Al_5Ti_{2.5}$, and $Cr_{20}Co_{17.5}Ni_{50}Al_{12.5}$ alloys produced in an Arc-Melter furnace.

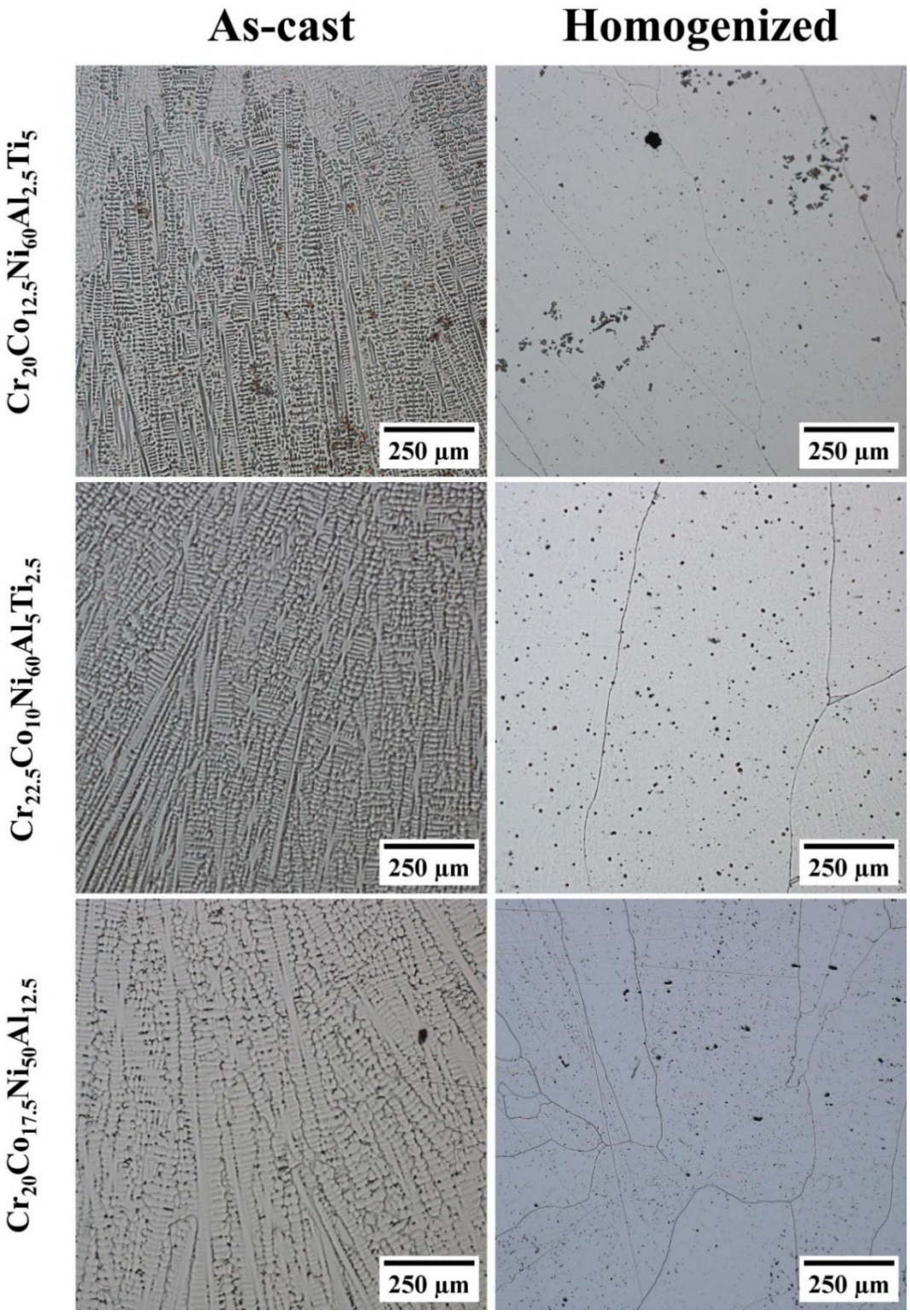

Figure 5.17: Optical micrographs of $Cr_{20}Co_{12.5}Ni_{60}Al_{2.5}Ti_5$, $Cr_{22.5}Co_{10}Ni_{60}Al_5Ti_{2.5}$, and $Cr_{20}Co_{17.5}Ni_{50}Al_{12.5}$ alloys in the as-cast and homogenized conditions after chemical etching with Glyceregia etchant.

In the two titanium containing alloys, the inclusions were identified as titanium nitride (TiN). This inclusion is commonly observed in most superalloys since Ti is a strong nitride former element [93,129]. On the other hand, Al-N rich inclusions were observed in the Ti-free alloy. Figure 5.18 shows in the left column SEM images of the observed inclusions, and in the right column their respective EDS spectrum. The result of EDS quantification is shown as insets in the spectrums. It should be noted here that nitrogen (N) was quantified in the inclusions only to show qualitatively that this element is present in these defects, since the quantification of light elements such as nitrogen using EDS technique is inaccurate.

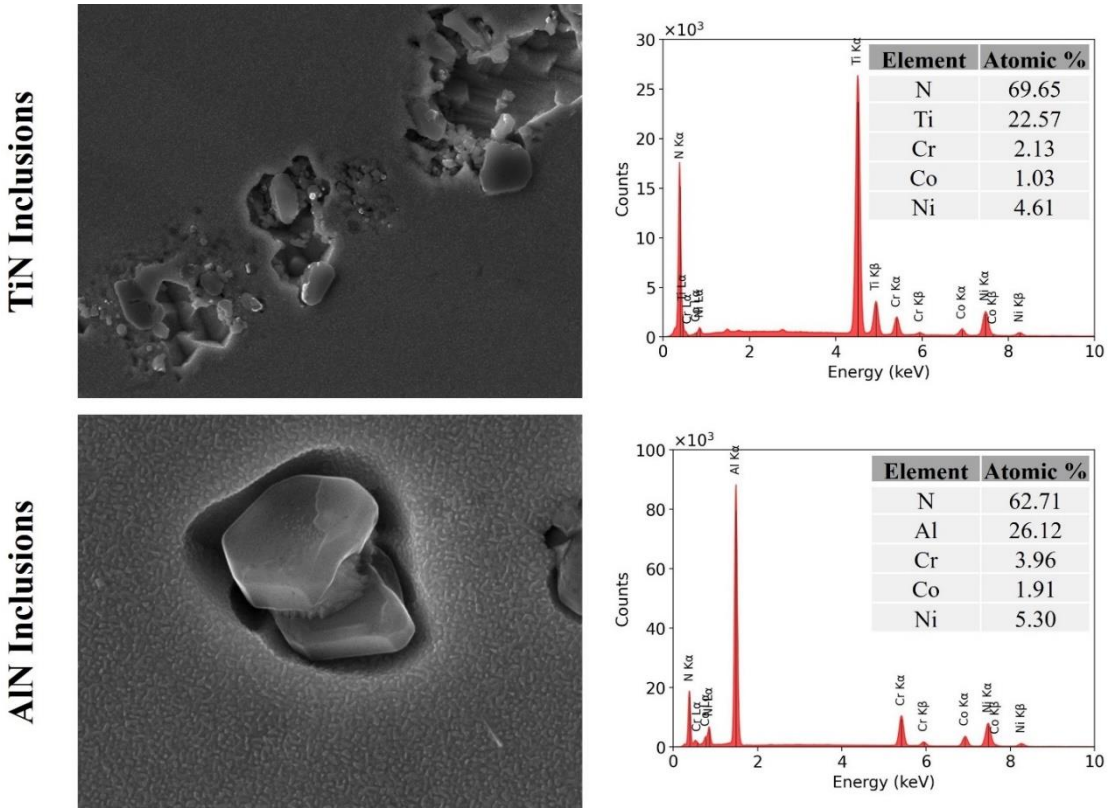

Figure 5.18: Left column: SEM images of observed inclusions in the investigated alloy acquired using Everhart-Thornley detector (E-T); Right column: EDS spectrum of inclusion. The table inset present a qualitative chemical composition of the defects.

For quantifying the volume fraction of inclusions, sixteen different fields of the samples in homogenized condition were analyzed. The analyses were performed in the samples in the as-polished condition A representative image of

each alloy in the latter condition is shown in Figure 5.19. As can be observed, for the 5at.% Ti alloy, the inclusions tends to agglomerate in some regions, while for 2.5at.% Ti and the Ti-free alloys the inclusions are homogeneously distributed throughout the sample. Using the ImageJ software these volumetric defects were properly segmented, as can be seen in the right middle and right columns of Figure 5.19.

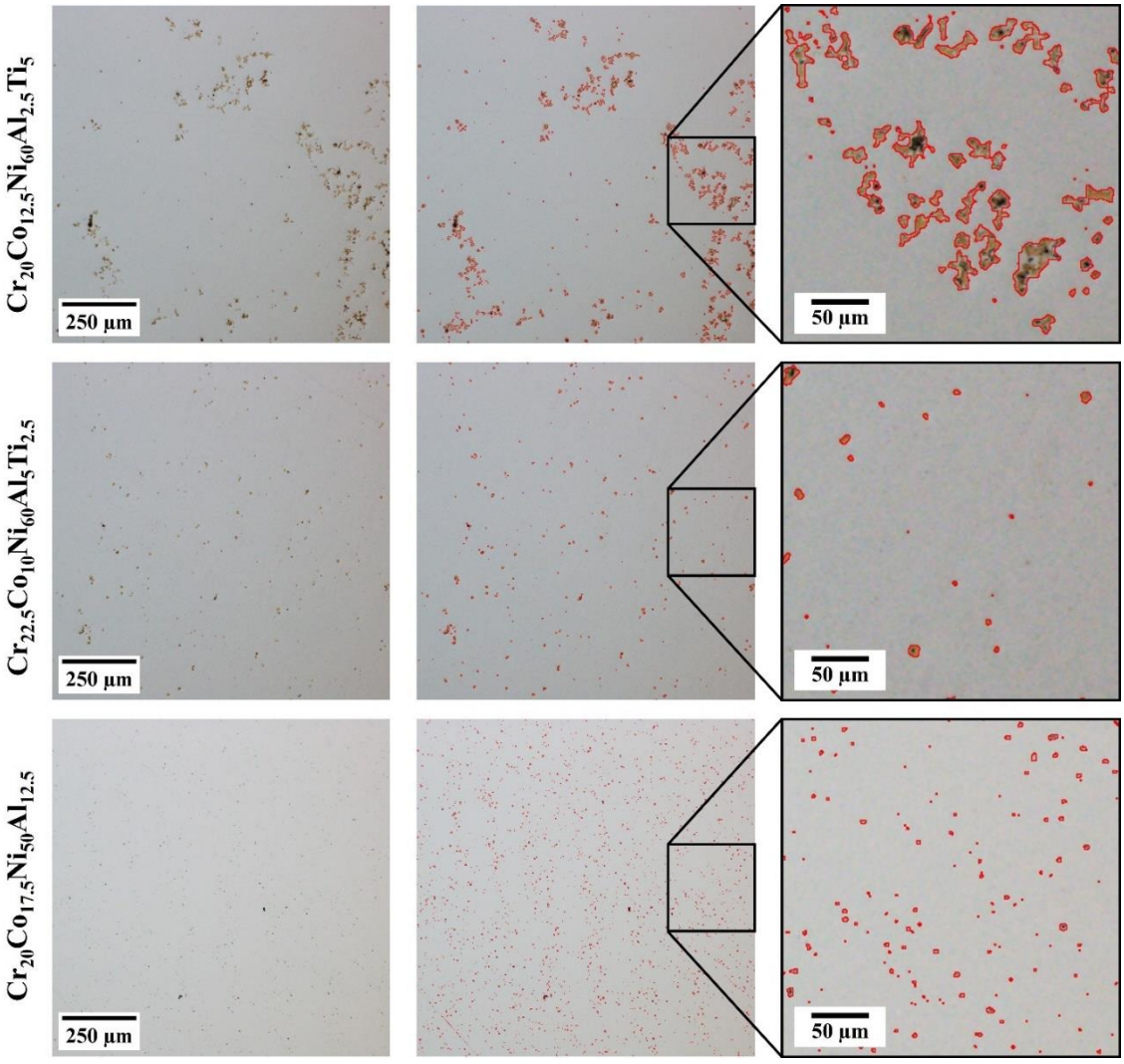

Figure 5.19: Optical micrographs of $Cr_{20}Co_{12.5}Ni_{60}Al_{2.5}Ti_5$, $Cr_{22.5}Co_{10}Ni_{60}Al_5Ti_{2.5}$, and $Cr_{20}Co_{17.5}Ni_{50}Al_{12.5}$ alloys in the homogenized condition in the as-polished state.

After segmenting all the images, the mean volume fraction of inclusions was measured, and the results are shown in Figure 5.20. Since the inclusions present a very irregular shape, the Feret diameter, given by Equation 5.8, was

chosen as a representative parameter to measure the mean planar inclusion sizes.

$$\langle F \rangle = \frac{P}{\pi}. \tag{5.8}$$

In Equation 5.8, P is the perimeter of the object (note that for a circular object $\langle F \rangle$ equals to 2r). The average Feret diameter is also shown in Figure 5.20. As can be observed, $\langle F \rangle$ decreases with decreasing Ti concentration in the alloys.

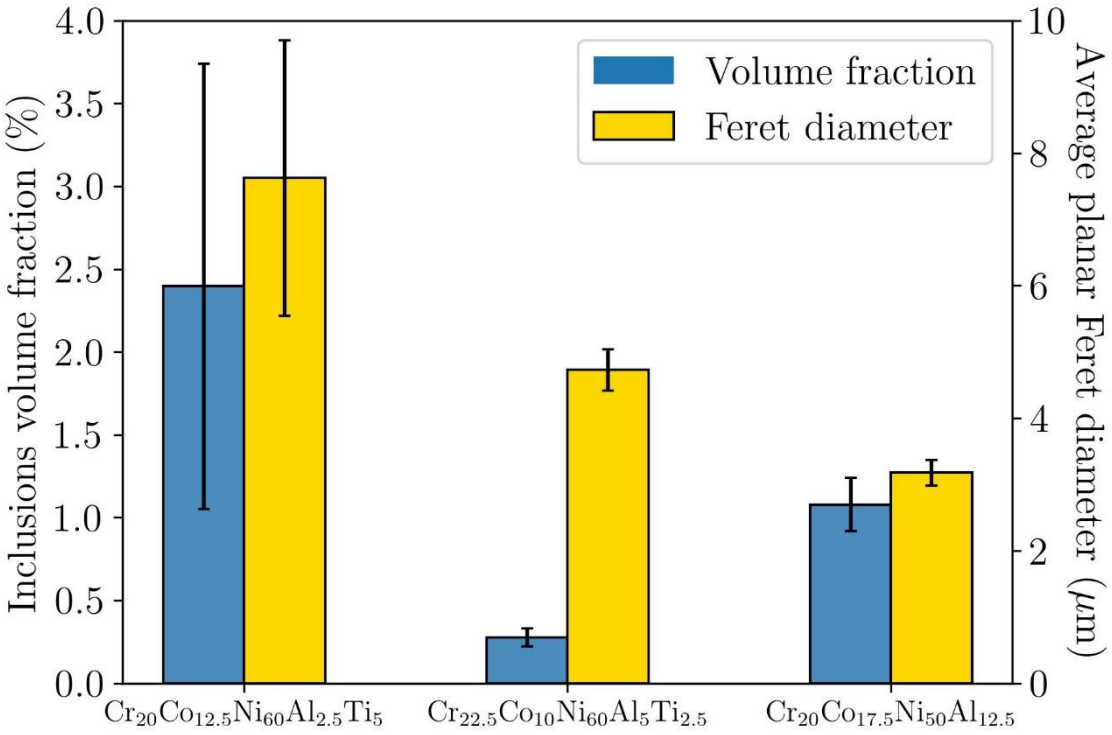

Figure 5.20: Volume fraction and mean planar Feret diameter of inclusions observed on $Cr_{20}Co_{12.5}Ni_{60}Al_{2.5}Ti_5$, $Cr_{22.5}Co_{10}Ni_{60}Al_5Ti_{2.5}$, and $Cr_{20}Co_{17.5}Ni_{50}Al_{12.5}$ alloys produced in this work.

For a better understanding of the effect of Nitrogen as well as the alloy chemistry in the equilibrium fraction of TiN inclusions, a compositional screening in the $(Ni_{60}Cr_{20}Co_{10}Al_{10-x}Ti_x)_{1-y}(N_{100})_y$ system was performed through CALPHAD calculations. The following limits and atomic step concentration was taken for x and y:

$$\begin{cases} 0 \le x \le 10, & \Delta x = 1 \\ 0 \le y \le 0.0044, & \Delta y = 0.0004 \end{cases}$$

A representative phase equilibrium calculation as a function of temperature, for a Ti containing alloy, is shown in Figure 5.21. As can be seen, the TiN phase (represented in the diagram as Fcc_MC) are formed in the melt and remains stable at lower temperatures. Therefore, once the inclusions are formed, they remain in the alloy under typical thermo-mechanical processing.

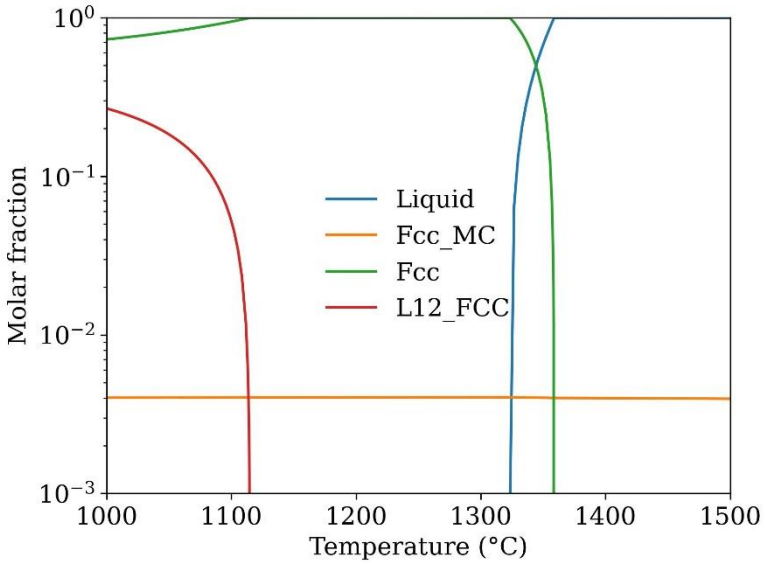

Figure 5.21: Results of the thermodynamic calculation for the $(\mathrm{Ni_{60}Cr_{20}Co_{10}Al_5Ti_5})_{0.998}(\mathrm{N_{100}})_{0.002}$ alloy displaying the mole fraction of the equilibrium phases as a function of temperature. The calculation was performed using the CALPHAD method via software PandatTM and PanNi2021 database.

The effect of Nitrogen concentration and the alloy composition, at 1500 °C, on the molar fraction of titanium nitride is shown in Figure 5.22. It is worth mentioning that the molar fraction of inclusions is expected to be lower than their volume fraction, since the density of TiN is lower than that of the Cr-Co-Ni-Al-Ti phases. It can be noted that, for a same level of Nitrogen, the calculated molar fraction of TiN is almost independent of x_{Ti}/x_{Al} ratio for values greater than 0.25. This is in contradiction with what is experimentally observed, where the 5%Ti alloy presents a higher volume fraction of inclusions than the 2.5% Ti alloy. To address this inconsistency, concentration analyses of Nitrogen on the produced alloys as well as the metals used as raw materials were performed. Results are summarized in the Table 5.7. Furthermore, during the melting of the ingots, a

leaking was observed in the Arc-Melter chamber. The alloys were produced in the following order $Cr_{20}Co_{12.5}Ni_{60}Al_{2.5}Ti_5$, $Cr_{22.5}Co_{10}Ni_{60}Al_5Ti_{2.5}$, and $Cr_{20}Co_{17.5}Ni_{50}Al_{12.5}$. This is also the ascending order of argon gas pressure used during melting to prevent contamination from the atmosphere. Therefore, both atmospheric air and Titanium used as raw material acted as sources of interstitial contamination.

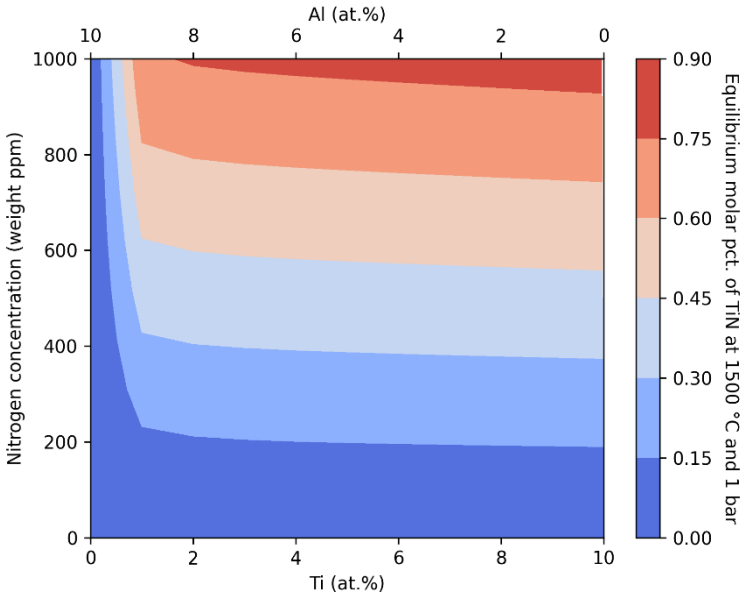

Figure 5.22: Equilibrium TiN molar fraction at 1500 °C as a function of nitrogen concentration and x_{Ti}/x_{Al} ratio for $(Ni_{60}Cr_{20}Co_{10}Al_{10-x}Ti_x)_{1-y}(N_{100})_y$ system. The calculation was performed using the CALPHAD method via software Pandat™ and PanNi2021 database.

Table 5.7: Concentration of Nitrogen, Oxygen, and Carbon on the raw materials and in the produced alloys in this work.

	Nitrogen (wt. ppm)	Oxygen (wt. ppm)	Carbon (wt. ppm)
Cr	8.9 ± 1.2	30.7 ± 12.2	56.7 ± 5.8
Co	0.2 ± 0.0	29.7 ± 1.8	143.3 ± 11.5
Ni	0.8 ± 0.1	6.2 ± 0.4	70 ± 10
Al	2.3 ± 0.9	41.5 ± 29.7	310 ± 60.8
Ti	1518.5 ± 565.7	1416.7 ± 370.2	160 ± 35
$Cr_{20}Co_{12.5}Ni_{60}Al_{2.5}Ti_5$	1301.8 ± 44.1	360.4 ± 39.9	56.7 ± 30.6
$Cr_{22.5}Co_{10}Ni_{60}Al_5Ti_{2.5}$	294.2 ± 23.8	83.8 ± 3.3	43.3 ± 32.1
$Cr_{20}Co_{17.5}Ni_{50}Al_{12.5}$	141.2 ± 17.5	42.1 ± 0.3	93.3 ± 5.8

Although a relative high-volume fraction of inclusions was observed in all alloys, its effect on the yield strength is expected to be negligible. Assuming the interaction dislocation-inclusion given by the Orowan mechanism and considering the inclusion as spherical particles, their contribution to yield strength can be roughly estimated by Equation 5.9:

$$\tau_c^{Orowan} = \frac{2\sqrt{3}}{\sqrt{\pi}} \frac{\Gamma}{a} \frac{\sqrt{f}}{r_0}. \tag{5.9}$$

where f is the volume fraction of inclusions, r_0 is the spatial inclusion radius in a monodisperse system, Γ is the dislocation line tension, and *a* is the lattice parameter of the matrix. The line tension is in the order of $\Gamma \approx 0.1 - 0.8 \times 10^{-9} N$, and $a \approx 0.35 \times 10^{-9} m$ for most Ni-based superalloys [51]. As shown in Figure 5.23, the contribution is dominated by the particle radius. The volume fraction of inclusion has only a slight effect on τ_c^{Orowan}, which is justified by its square root dependence. Assuming the ratio Γ/a equals unity, particles with sizes in the nanometer range may provide a contribution of about 100-1000 MPa, while particles in the micrometer range have a contribution smaller than 1 MPa to yield strength.

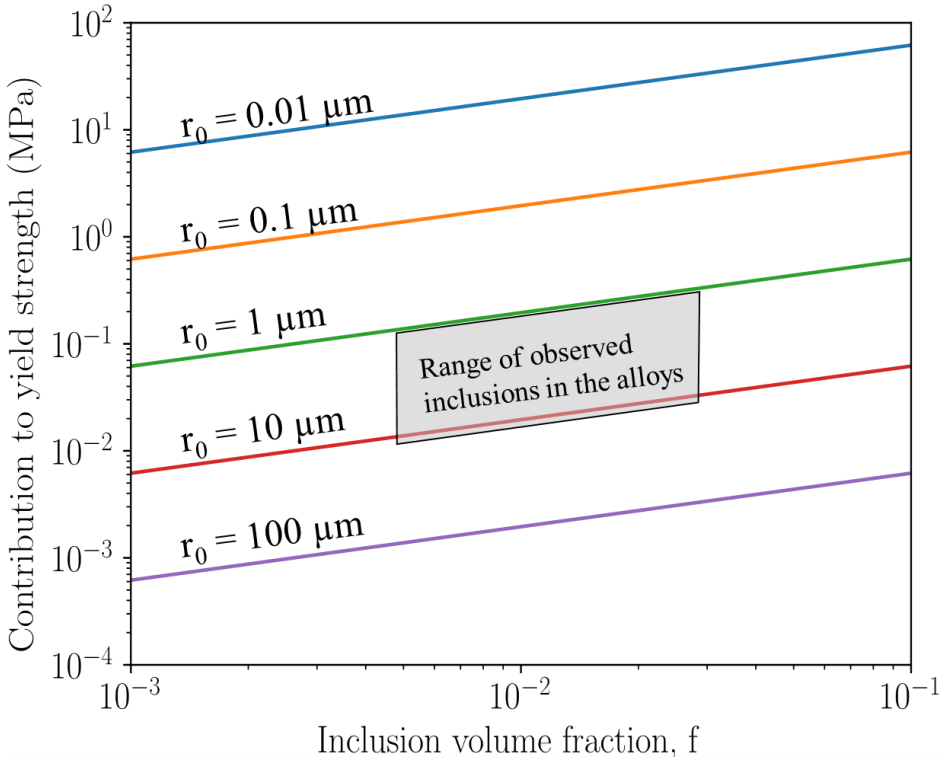

Figure 5.23: Effect of volume fraction and mean radius of inclusions on the contribution to yield strength, considering Γ/a equal unity.

Although the inclusions are expected to have an insignificant effect on yield strength, they may lead to a loss of ductility, fatigue, and creep resistance, since they act as preferential site for crack nucleation and aid the crack propagation [130]. As discussed by Mitchell [129], the most effective means of controlling the nitrogen content in Ni-superalloys lies in the choice of clean raw materials for the alloy production.

Cold rolled sheets of the three designed alloys are shown in Figure 5.24. The heads and tails of the sheets were cut after the rolling. The sheets show no surface cracking and only minor edge cracking.

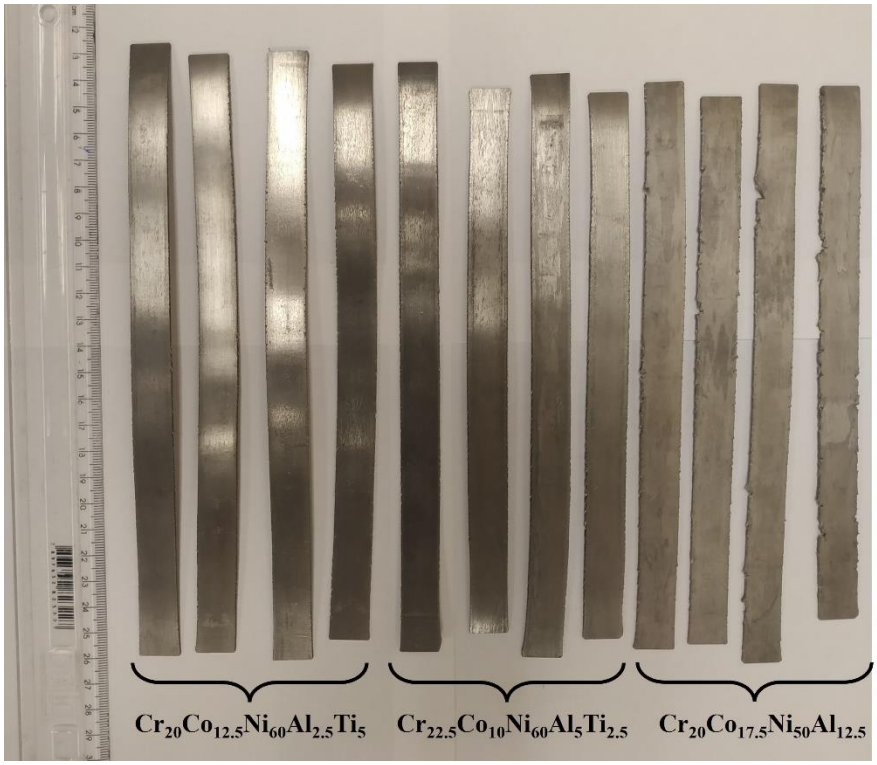

Figure 5.24: Cold rolled sheet of $Cr_{20}Co_{12.5}Ni_{60}Al_{2.5}Ti_5$, $Cr_{22.5}Co_{10}Ni_{60}Al_5Ti_{2.5}$, and $Cr_{20}Co_{17.5}Ni_{50}Al_{12.5}$ alloys.

The results of the thermal analyses carried out on samples of the selected alloys aged at 750 °C are shown in Figure 5.25. The solvus was determined as the final temperature of the endothermic reaction of FCC+$L1_2$→FCC, whereas the *solidus* was determined as the start temperature of the endothermic melting peak of the alloys. The results predicted by thermodynamic calculations are presented in the table inset the figure. As can be seen, there is good agreement between the values measured experimentally and those calculated by the CALPHAD method. Since the final temperature of the endothermic peak is uncertain, it is not possible to determine the *liquidus* with relative accuracy. However, it can be noted that the width of the melting peaks scales with the width of the calculated solidification interval.

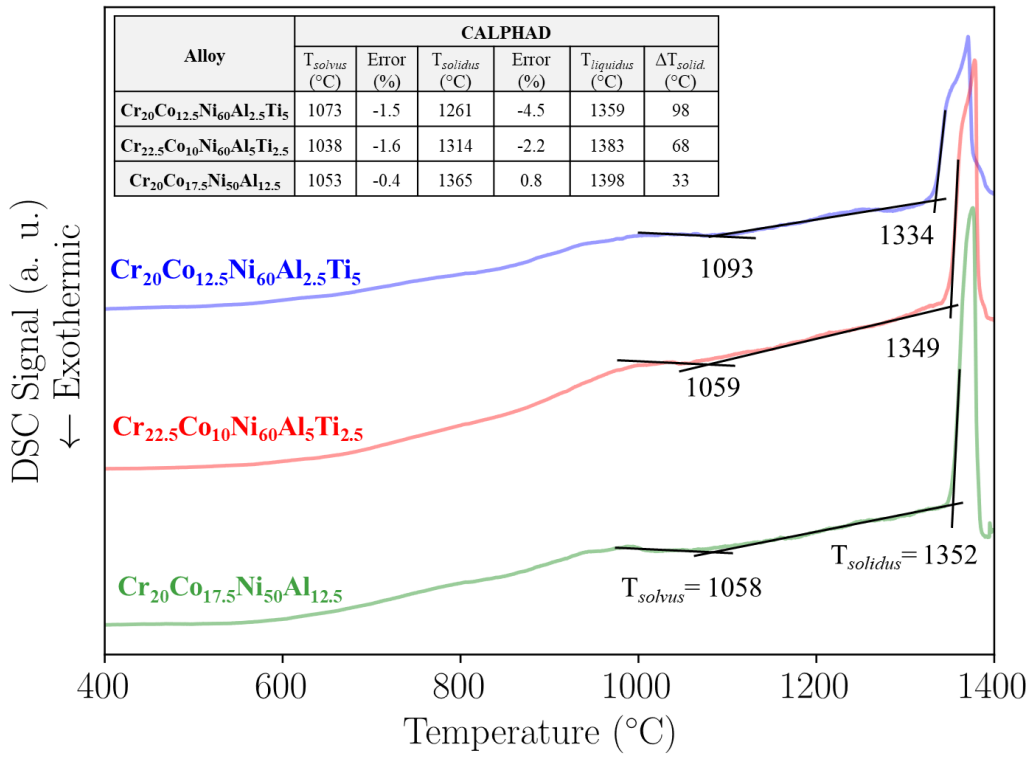

Figure 5.25: DSC curves of $Cr_{20}Co_{12.5}Ni_{60}Al_{2.5}Ti_5$, $Cr_{22.5}Co_{10}Ni_{60}Al_5Ti_{2.5}$, and $Cr_{20}Co_{17.5}Ni_{50}Al_{12.5}$ alloys heated using a heating rate of 10°C/min. The errors shown in the table inset were calculated using Kelvin scale as the CALPHAD method employs this scale during calculations.

SEM images of the cold-rolled sheets after solution treatment at 1200 °C for 1h plus water quenching is shown in the left column of Figure 5.26. These images were acquired using the SEM backscattered electron detector. Annealing twins and inclusions elongated along the rolling direction can be observed in the images. No second-phase particles could be seen in the grain boundaries of the alloys, even at higher magnification. TEM images of the solution treated alloys acquired on a low index zone axis and their respective diffraction pattern (shown inset) are presented in right column of Figure 5.26. The colors of the patterns were inverted to improve the clarity of the superlattice reflections. The dark-field TEM images were acquired using the superlattice reflection of $L1_2$ phase. The approximate radius of these particles is also presented inset each TEM image. The formation of $L1_2$ precipitates upon fast cooling is often observed for nickel superalloys with relative high equilibrium fraction of $L1_2$ phase at high temperature.

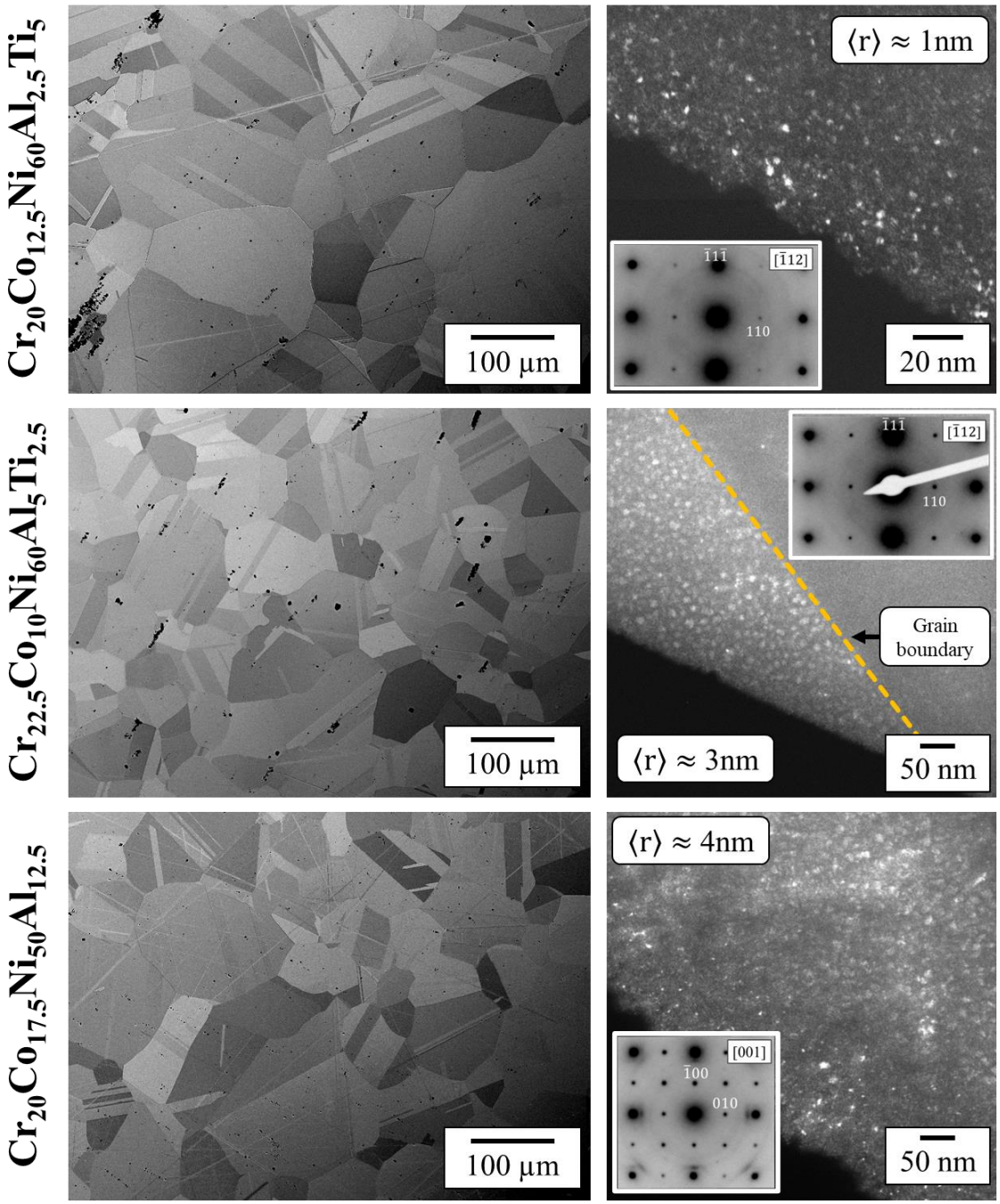

Figure 5.26: SEM images acquired using backscattered electron detector and TEM images of $Cr_{20}Co_{12.5}Ni_{60}Al_{2.5}Ti_5$, $Cr_{22.5}Co_{10}Ni_{60}Al_5Ti_{2.5}$, and $Cr_{20}Co_{17.5}Ni_{50}Al_{12.5}$ alloys in the solution treated condition (1h at 1200 °C plus water quenching).

Figure 5.27 shows SEM images acquired using Everhart-Thornley detector of the designed alloys after aging treatment at 750 °C for 200h. At this

condition, discontinuous precipitation colonies and discrete particles can be observed along the grain boundaries in all alloys.

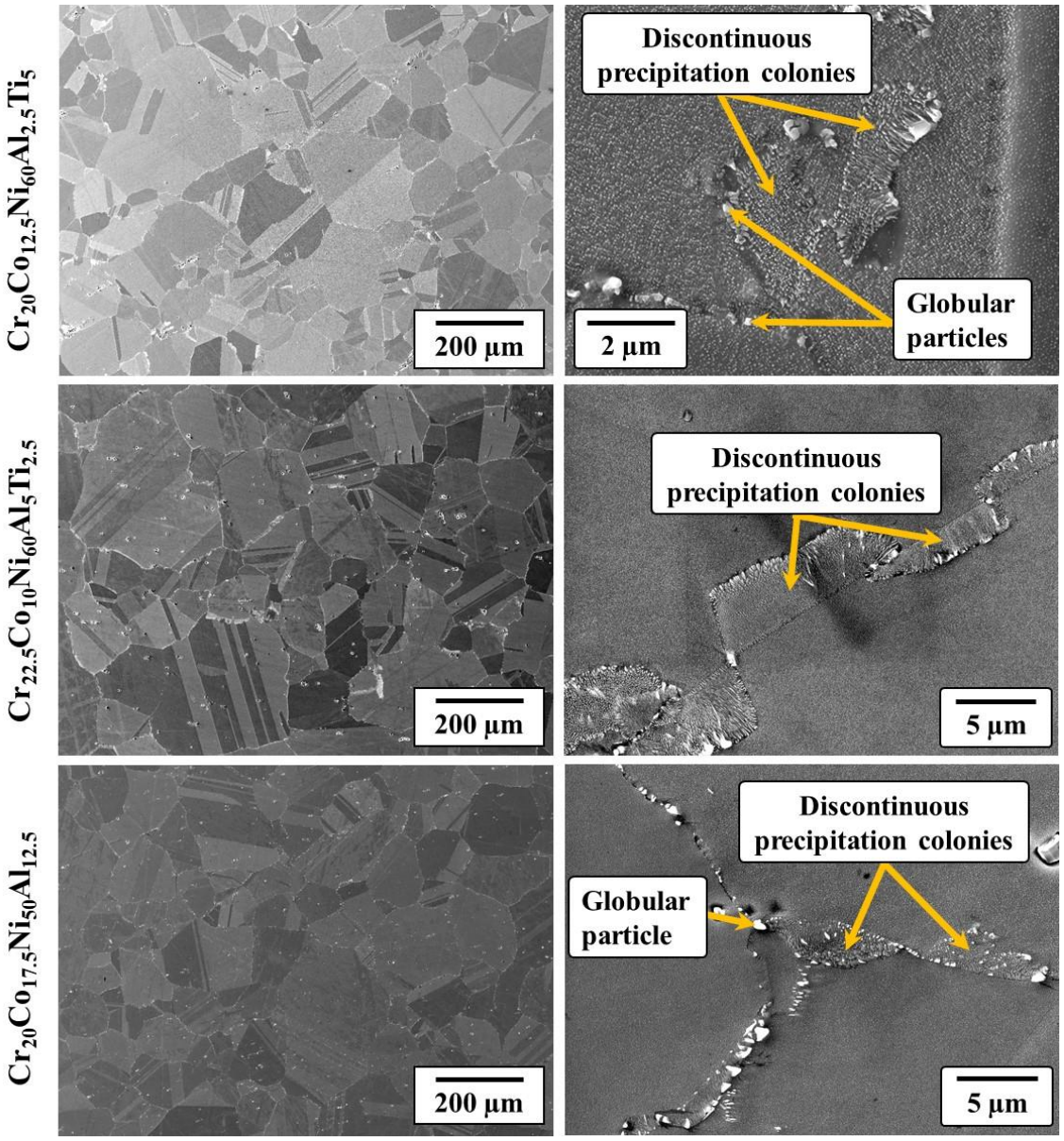

Figure 5.27: SEM images of $Cr_{20}Co_{12.5}Ni_{60}Al_{2.5}Ti_5$, $Cr_{22.5}Co_{10}Ni_{60}Al_5Ti_{2.5}$, and $Cr_{20}Co_{17.5}Ni_{50}Al_{12.5}$ alloys acquired using Everhart-Thornley detector after aging treatment at 750 °C for 200h.

Discontinuous precipitation (DP) is defined as a solid-state precipitation reaction characterized by grain boundary migration with the growing cell tips [131]. The morphology of DP products is often lamellar, occasionally fibrous or rod-type, and very rarely globular [132]. This reaction is also known as cellular or

zipper precipitation [130]. The DP cells may grow in only one direction or in opposite directions from the original grain-boundary position. This reaction has been observed for a long time in a wide range of alloys [133], ranging from simple binaries, for example Pb-Sn [134], to more complex systems such as those of stainless steels [135] and superalloys [136]. Recently, such undesired precipitation behavior has been reported in several HEAs [137–141].

Three basic types of discontinuous precipitation reactions are proposed in the literature to explain most of the reactions in binaries systems [133], as schematically illustrated in Figure 5.28. In the first type, a single-phase supersaturated matrix α' transforms to an alternated lamellae microstructure of β and solute-depleted α, with no change in the crystal structure of α. The driving force for the latter reaction is the reduction in Gibbs free energy due to the transformation of α' in more stable phases α+β. In the second type of reaction, a matrix α' with an excess of solute and containing discrete, stable, coherent precipitates β transforms to a lamellae solute depleted α plus coarser β. This reaction is also known as discontinuous coarsening. In this case, the driving force is mainly attributed to the reduction of Gibbs free energy through the reduction of the interfacial energy of the microstructure. If the solute solubility in both α and β changes, the reaction is given by α'+β'→α+β. In the third type of reaction, coherent, discrete, and metastable β precipitates transform to a more stable δ phase via reaction α+β→α+δ. The driving force for the latter transformation is similar to the type 1 reaction.

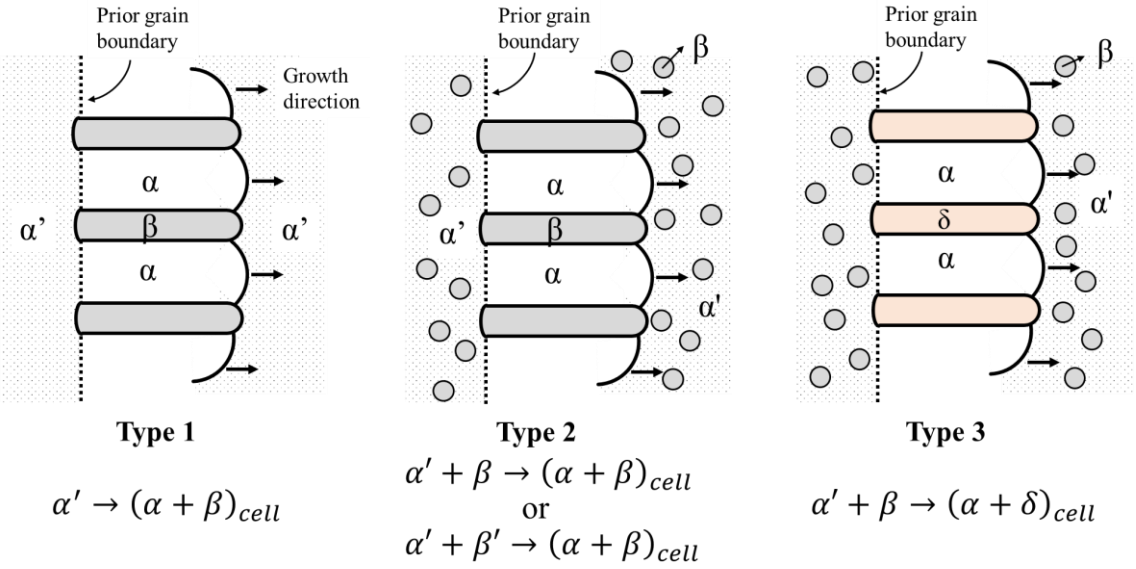

Figure 5.28: Classification of discontinuous precipitation reaction types [133]

An SEM image of a cellular colony observed in the $Cr_{20}Co_{17.5}Ni_{50}Al_{12.5}$ alloy is presented in detail in Figure 5.29a. The image inset reveals that $L1_2$ precipitates within the cellular colonies transforms into $L1_2$ laths. Additionally, bright globular particles are visible in the vicinity of DP colonies. These observations suggests that type 1 and type 2 reactions may be taking place during the aging treatment of the alloys under investigation. Figure 5.29b shows the prior grain boundary (indicated by the dashed yellow line), the actual grain boundary (indicated by the dashed red line), and the growth direction of the cellular colonies (indicated by the red arrows) presented in Figure 5.29a. Although the image shows details of a colony presented in the $Cr_{20}Co_{17.5}Ni_{50}Al_{12.5}$ alloy, a similar behavior was observed in the other alloys studied in this work.

Line EDS measurements, shown in Figure 5.30, indicates the presence of chromium rich carbides in the investigated alloys. Chemical analyses across the cellular colonies shows that the composition has no significant change from matrix plus precipitate region. Although the presence of carbon in the alloys was unexpected, a concentration of approximately 50 wt. ppm was observed in the produced alloys, as shown previously in Table 5.7. As can be noted, Aluminum and Titanium were the primarily source of this contamination. However, the intentional addition of carbon to commercial Ni-superalloys is common, as it can

lead to the formation of carbide particles along the grain boundaries. This, in turn, can enhance the creep strength of the alloy by inhibiting grain-boundary sliding at high-temperature applications.

The common classes of carbides found in superalloys and their crystallographic information are shown in Table 5.8 [130]. In many superalloys the MC carbide, which is usually rich in Ti, Ta and/or Hf, precipitates at high temperatures. The $M_{23}C_6$ carbides is formed at lower temperatures (around 750 °C), particularly in alloys which are Cr -rich.

The $M_{23}C_6$ carbides typically presents the following crystallographic relationship with the FCC matrix:

$$\{100\}_{M_{23}C_6} || \{100\}_{FCC}$$

$$\langle 100\rangle_{M_{23}C_6} || \langle 100\rangle_{FCC}$$

Furthermore, this carbide has a lattice parameter from two to three times larger than the lattice parameter of FCC matrix in Ni-superalloys.

Table 5.8: Common classes of carbides observed in Ni-superalloys.

Phase	Space Group	Pearson symbol	Prototype structure	Lattice Parameter (Å)
MC	$\mathrm{Fm\bar{3}m}$	cF8	NaCl	a = 4.30-4.70
$M_{23}C_6$	$\mathrm{Fm\bar{3}m}$	cF116	$Cr_{23}C_6$	a = 10.50-10.70
M_6C	$\mathrm{Fd\bar{3}m}$	cF112	Fe_3W_3C	a = 10.85-11.75

Although the understanding of discontinuous precipitation reaction is desirable, the precise conditions during which DP occurs or is preferred over continuous precipitation (CP) (Type 2 reaction) is still a matter of controversy in the literature [131]. The reaction initiation may change in the same system depending on aging temperatures. Furthermore, it may differ from one alloy to another, even in a similar class of alloys, and it may be more complex in multicomponent systems. For example, Nystrom et. al. [142] investigated a refractory nickel superalloy ($Ni_{61.1}Cr_{5.4}Co_{13.2}Al_{13.8}W_2Hf_{0.1}Re_{2.1}Ta_{2.4}$, in at%) and

noticed the following reaction on grain boundary FCC+ $L1_2$ → FCC_{cell}+$L1_{2cell}$+TCP, where TPC is a Rhenium-rich Topological Close Packed (TCP) phase, identified as the P-phase by the authors. Similar behavior was observed for a variation of commercial nickel superalloys CMSX-4 with high-Re content [143]. Yang and coworkers [139] studied the $Ni_{29.9}Cr_{15}Co_{30}Fe_{13}Al_6Ti_6B_{0.1}$ (at. %) alloy. They observed a two-step discontinuous reaction along the grain boundaries. First, the coherent, discrete $L1_2$ precipitates embedded in an FCC matrix transformed to a lamellar FCC plus metastable $L1_2$ phase along the grain boundaries. With the progress of aging, the lamellae FCC plus metastable $L1_2$ transformed into a lamellar (FCC+$L1_2$) + blocky Heusler ($L2_1$) phase.

Since discontinuous precipitation is a controversial topic in the literature, a complete characterization of DP products as well as an investigation of the reasons for DP formation in the selected alloys are suggested as future work.

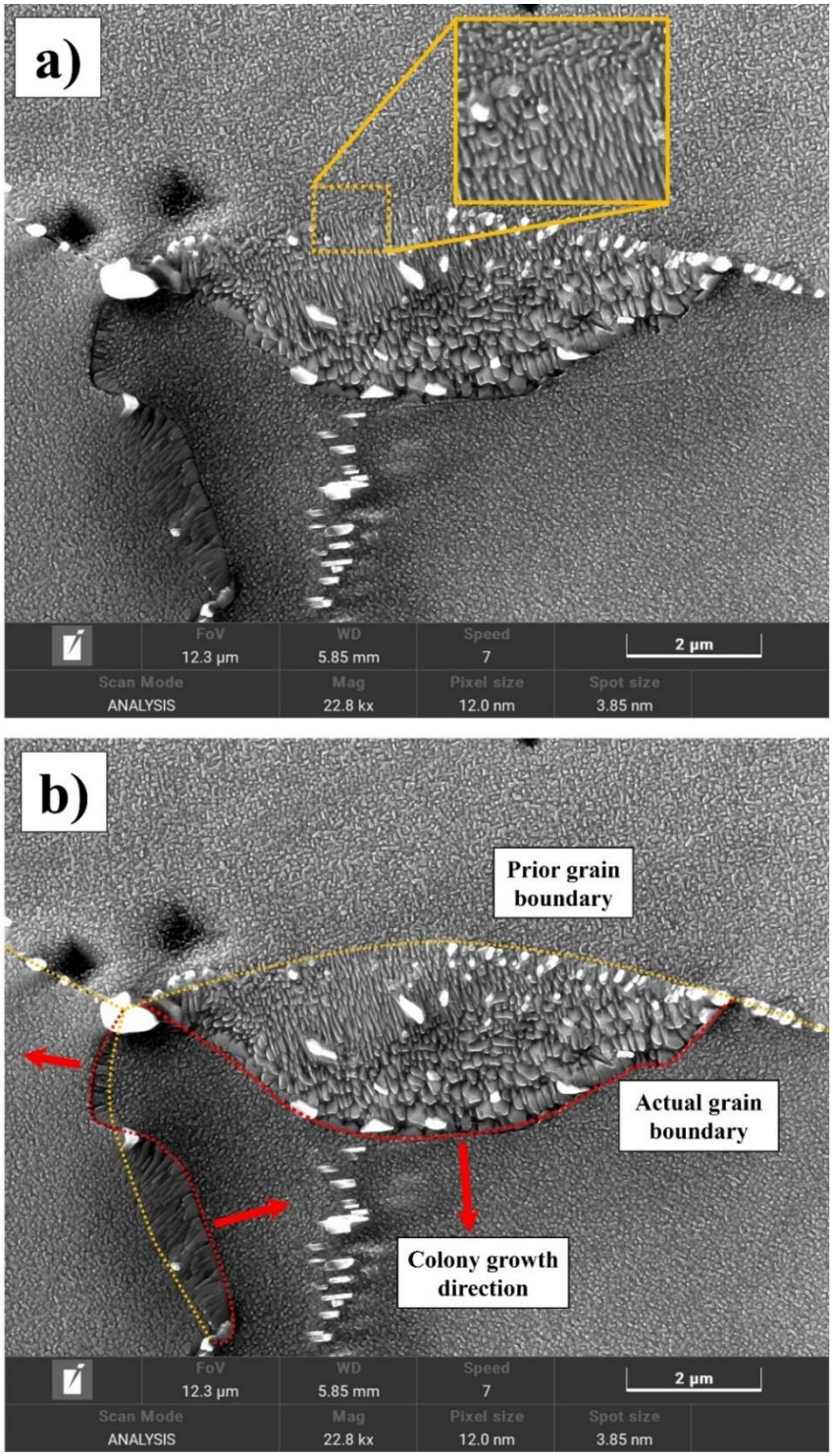

Figure 5.29: (a) SEM images acquired using Everhart-Thornley detector of grain boundary microstructure of $Cr_{20}Co_{17.5}Ni_{50}Al_{12.5}$ alloy after aging at 750 °C for 200h. Before SEM analysis, the sample was chemically etched with Glyceregia.

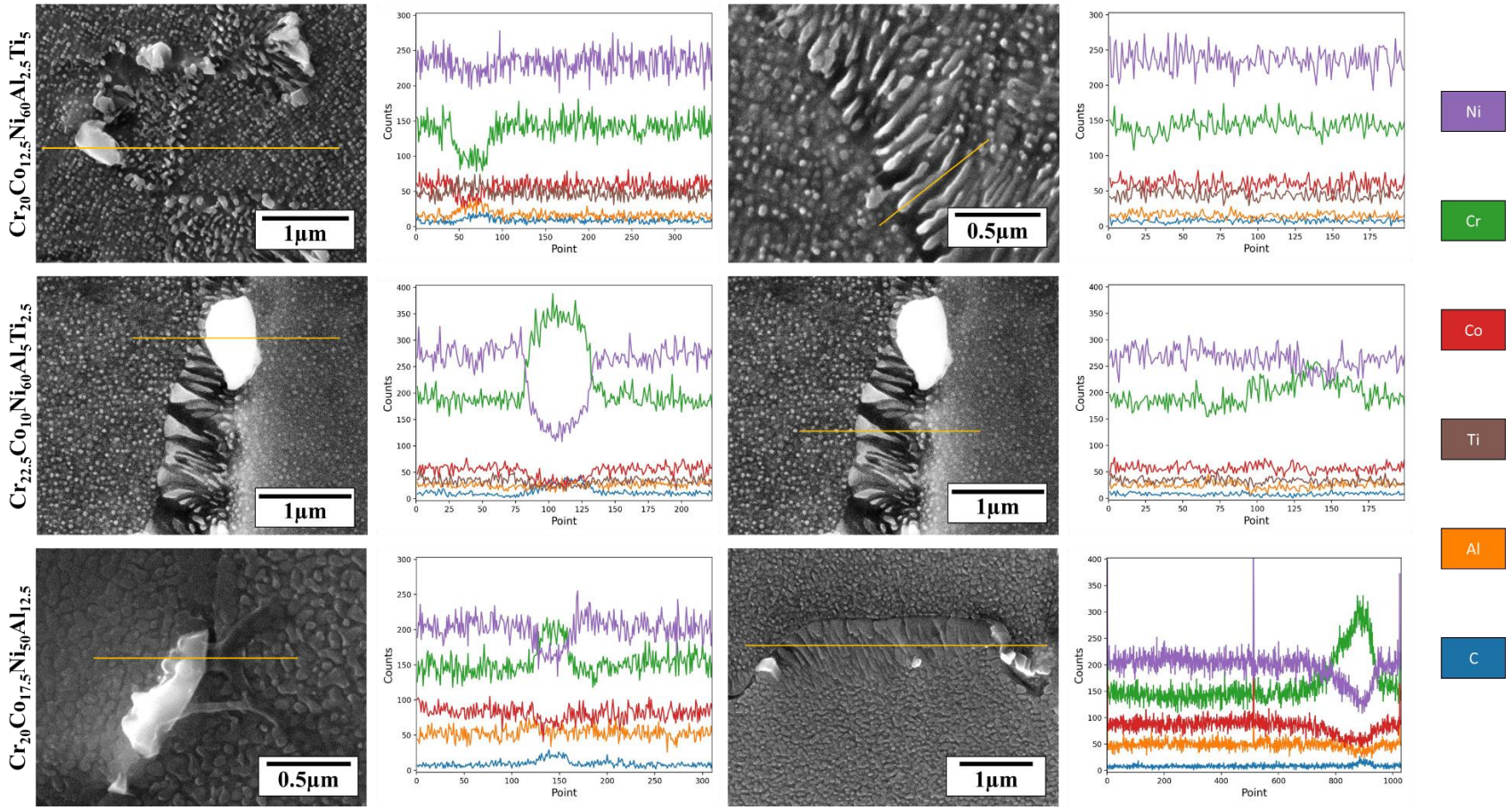

Figure 5.30: EDS line scan along different regions of $Cr_{20}Co_{12.5}Ni_{60}Al_{2.5}Ti_5$, $Cr_{22.5}Co_{10}Ni_{60}Al_5Ti_{2.5}$, and $Cr_{20}Co_{17.5}Ni_{50}Al_{12.5}$ alloys after aging treatment at 750 °C for 200h. The yellow line over the SEM images indicates the location of the EDS line scan. The resulting scan is shown in the plot on the right side adjacent to each image. The elemental identification color is displayed in the rightmost column.

High resolution SEM images taken from the interior of randomly chosen grains are shown in Figure 5.31. The mean equivalent radius of the precipitates and the standard deviation of the measurements are shown in the insets of each image. The particles are homogeneously distributed along the matrix in all alloys. The chemical etching attacks the FCC matrix, an accurate quantification of volume fraction of precipitates is not possible to be measured, since etching depth is not known and may be uneven through the sample.

In both Ti containing alloys, the particles present a spherical morphology, while in the Ti-free alloy the precipitates show an irregular morphology. As indicated by the red dashed ellipse, in this latter alloy spherical particles coalesce and give origin to the irregular shape precipitates, which is justified by the higher volume fraction of the $L1_2$ phase in this case. The high standard deviation on the particles size is also a consequence of this phenomenon. Typically, $L1_2$ precipitates show a spherical morphology when the lattice misfit δ (defined in Equation 5.10) is smaller than $\pm 0.2\%$ [130]. Therefore, the spherical morphology of the particles indicates a very low lattice mismatch between $L1_2$ and FCC lattice parameters. This feature is especially interesting for creep resistance property, since particles with lower misfit presents a lower coarsening rate compared to non-spherical particles, for example, with the cuboidal morphology often observed in superalloys when the $0.5 \leq |\delta| \leq 1\%$.

A representative EDS spectrum of a matrix plus precipitates region of each alloy is shown in the right column of Figure 5.31. As can be noted, trace of carbon is present in all spectrums. EDS measurements were performed in the interior of three randomly chosen grain, very apart from each other, and their results are summarized inset the EDS spectrum. The standard deviation of the measurements indicates a very homogeneous chemical composition along the samples. The results also show that the grain interior presents a chemical composition close to the target, which corroborates the CALPHAD phase equilibrium predictions.

The diffraction pattern of the samples in the solution treated and aged for 200h at 750 °C are shown in Figure 5.32. No extra peaks are observed in the diffraction pattern of the alloys after the aging treatment. The absence of the carbides reflections in the pattern is justified mainly by two reasons: (1) because of their high lattice parameter, their most intense reflections are observed at 2θ positions smaller than 30° when using Cu Kα radiation; (2) the low volume fraction of these phases, as observed in Figure 5.26, contribute to a low intensity of their reflection. The unknown peak observed in the Ti-free alloy is most likely from Al-N rich inclusions.

In Ni-superalloys the FCC and $L1_2$ structure present close lattice parameters. Usually, the lattice misfit is less than ±1% [52,130]. Therefore, the interplanar distance and, consequently, the 2θ position of the FCC hkl and fundamental reflection of $L1_2$ phase are close, and their peaks tends to overlap in the XRD pattern.

$$\delta = \frac{a_{L1_2} - a_{FCC}}{a_{FCC}} \tag{5.10}$$

Although the $L1_2$ ordered phase has a primitive cubic lattice, its superlattice reflections are much weaker than the fundamental reflections of the disordered FCC structure. This fact is explained by the low structure factor of the former. Therefore, due to background noise and low scattering factor, the superlattice reflection of $L1_2$ cannot be observed in the diffraction patterns.

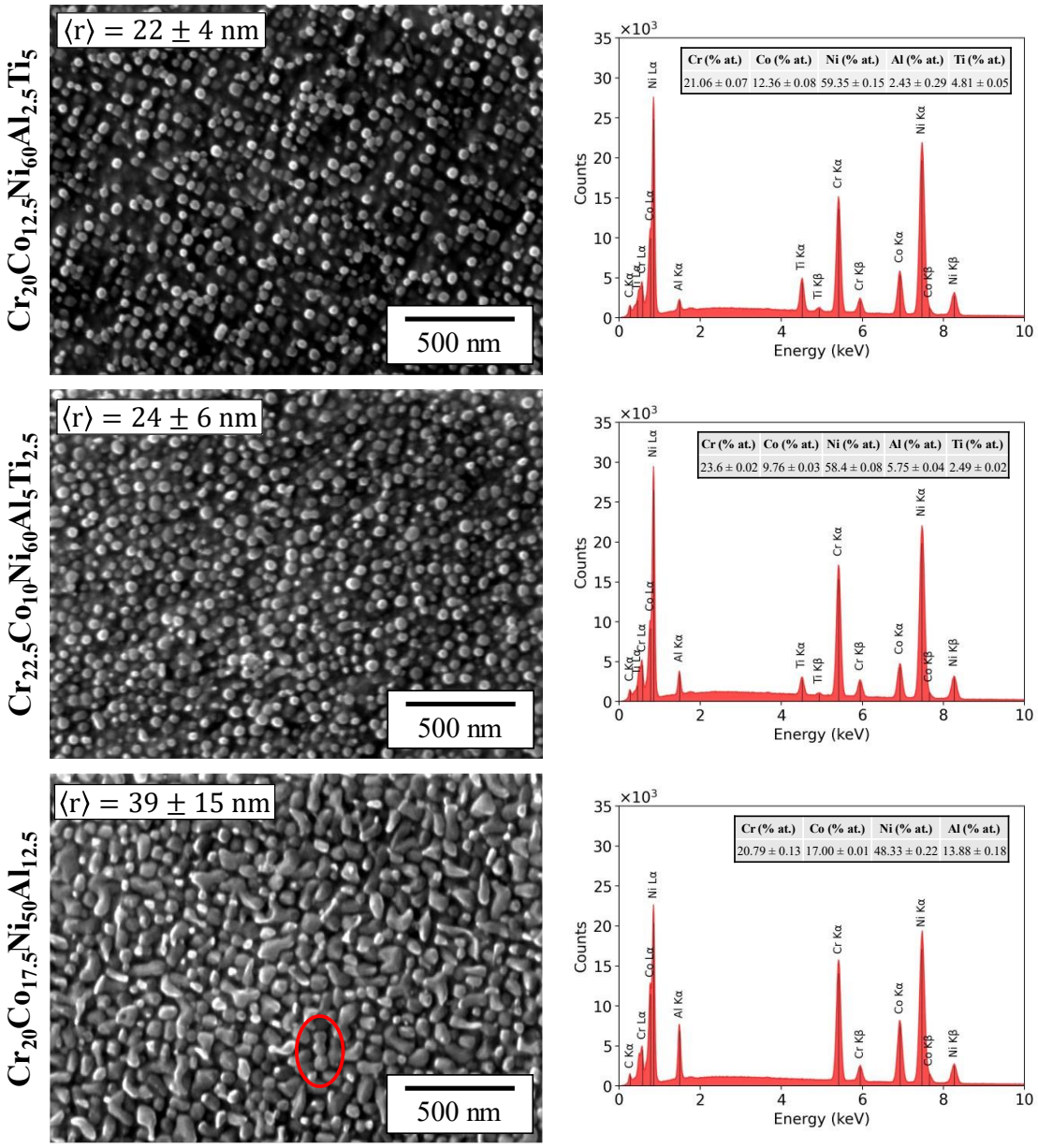

Figure 5.31: Left column: SEM images acquired using Everhart-Thornley detector of $Cr_{20}Co_{12.5}Ni_{60}Al_{2.5}Ti_5$, $Cr_{22.5}Co_{10}Ni_{60}Al_5Ti_{2.5}$, and $Cr_{20}Co_{17.5}Ni_{50}Al_{12.5}$ alloys after aging treatment at 750 °C for 200h. Before SEM analysis the samples were chemically etched with glyceregia etchant. The average precipitate radius and the standard deviation of measurements are shown in the inset. Right column: EDS spectrum of a typical region in the interior of a grain in the designed alloys.

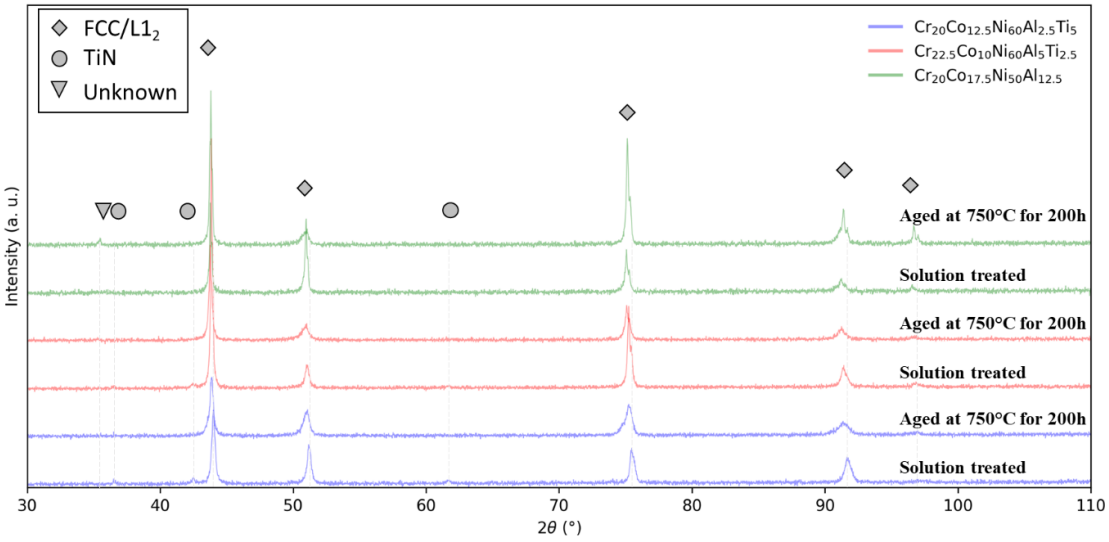

Figure 5.32: XRD patterns of $Cr_{20}Co_{12.5}Ni_{60}Al_{2.5}Ti_5$, $Cr_{22.5}Co_{10}Ni_{60}Al_5Ti_{2.5}$, and $Cr_{20}Co_{17.5}Ni_{50}Al_{12.5}$ alloys in the solution-treated (1h at 1200 °C) and aged condition (200h at 750 °C).

The hardness as a function of the aging time of $Cr_{20}Co_{12.5}Ni_{60}Al_{2.5}Ti_5$, $Cr_{22.5}Co_{10}Ni_{60}Al_5Ti_{2.5}$, and $Cr_{20}Co_{17.5}Ni_{50}Al_{12.5}$ alloys is shown in Figure 5.33. The error bars represent the standard deviation of measurements. An increase in the hardness value in both Ti-containing alloys is observed until ~100h of aging, and the peak aging condition is achieved in the time interval between 100 and 200h of heat treatment. On the other hand, the Ti-free alloy reach the peak aging condition earlier, at about 20h of treatment and the hardness remains constant until the 200h of aging. Most likely due to a higher coarsening rate and because of coalescence effect, the Ti-free alloys achieve the critical radius earlier than the Ti-containing alloys.

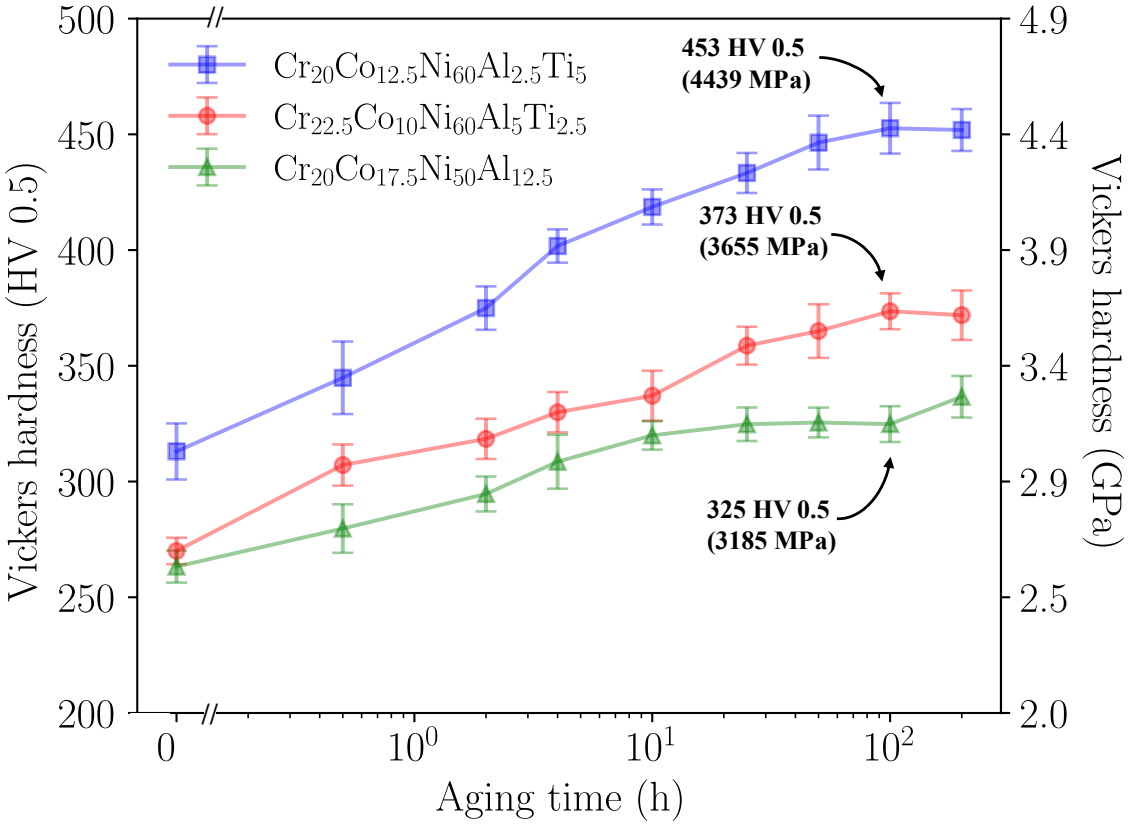

Figure 5.33: Hardness as a function of aging time at 750 °C of $Cr_{20}Co_{12.5}Ni_{60}Al_{2.5}Ti_5$, $Cr_{22.5}Co_{10}Ni_{60}Al_5Ti_{2.5}$, and $Cr_{20}Co_{17.5}Ni_{50}Al_{12.5}$ alloys.

Tensile engineering stress-strain curves of the selected alloys tested at room temperature, 650, 750, and 850°C are shown in the Figure 5.34. Before the tests, the samples were solution treated at 1200 °C for 1h and aged at 750 °C for 100h. At room temperature, the alloys presented high yield strength values and moderate ductility under tension. Fracture surface images of the tested specimens are shown Figure 5.35. Some specimens displayed poor ductility (<1%) at high temperatures, and their fracture surface analyses clearly show a brittle intergranular fracture, which is likely to be associated with the discontinuous precipitation along the grain boundaries.

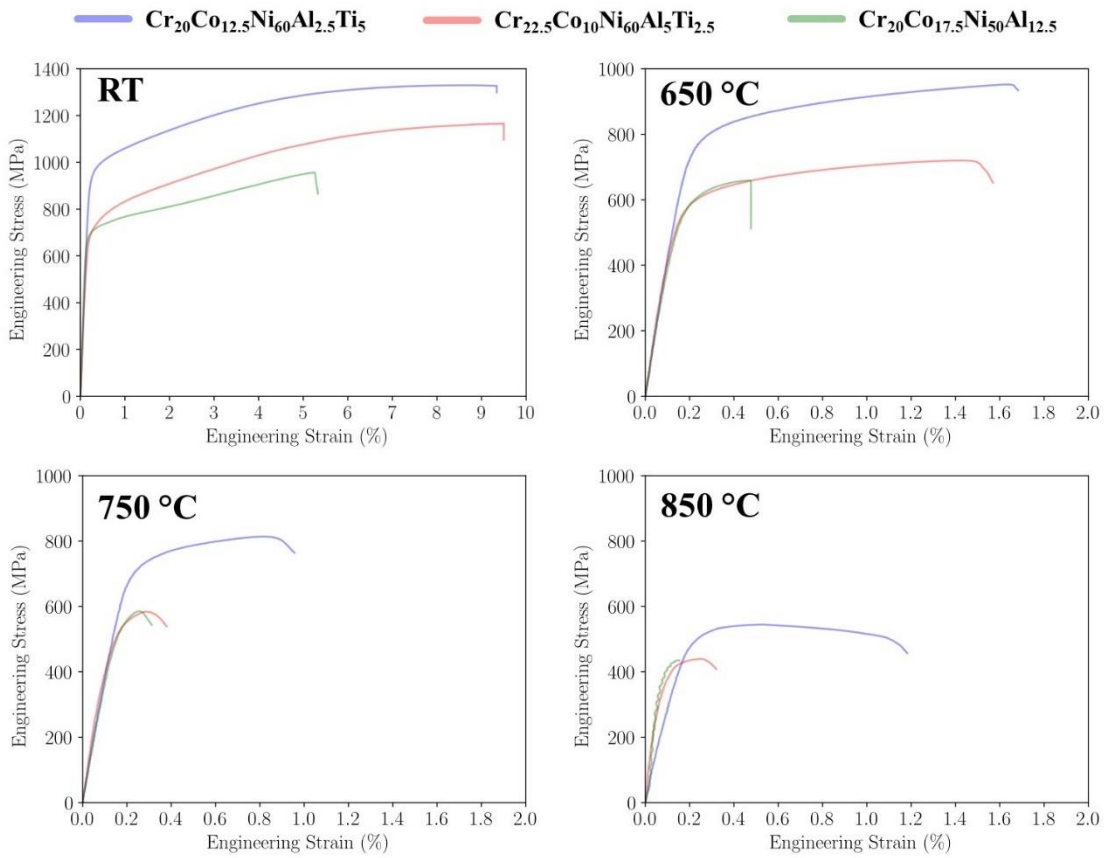

Figure 5.34: Tensile engineering stress-strain curves of $Cr_{20}Co_{12.5}Ni_{60}Al_{2.5}Ti_5$, $Cr_{22.5}Co_{10}Ni_{60}Al_5Ti_{2.5}$, and $Cr_{20}Co_{17.5}Ni_{50}Al_{12.5}$ alloys tested at room temperature, 650, 750, and 850°C.

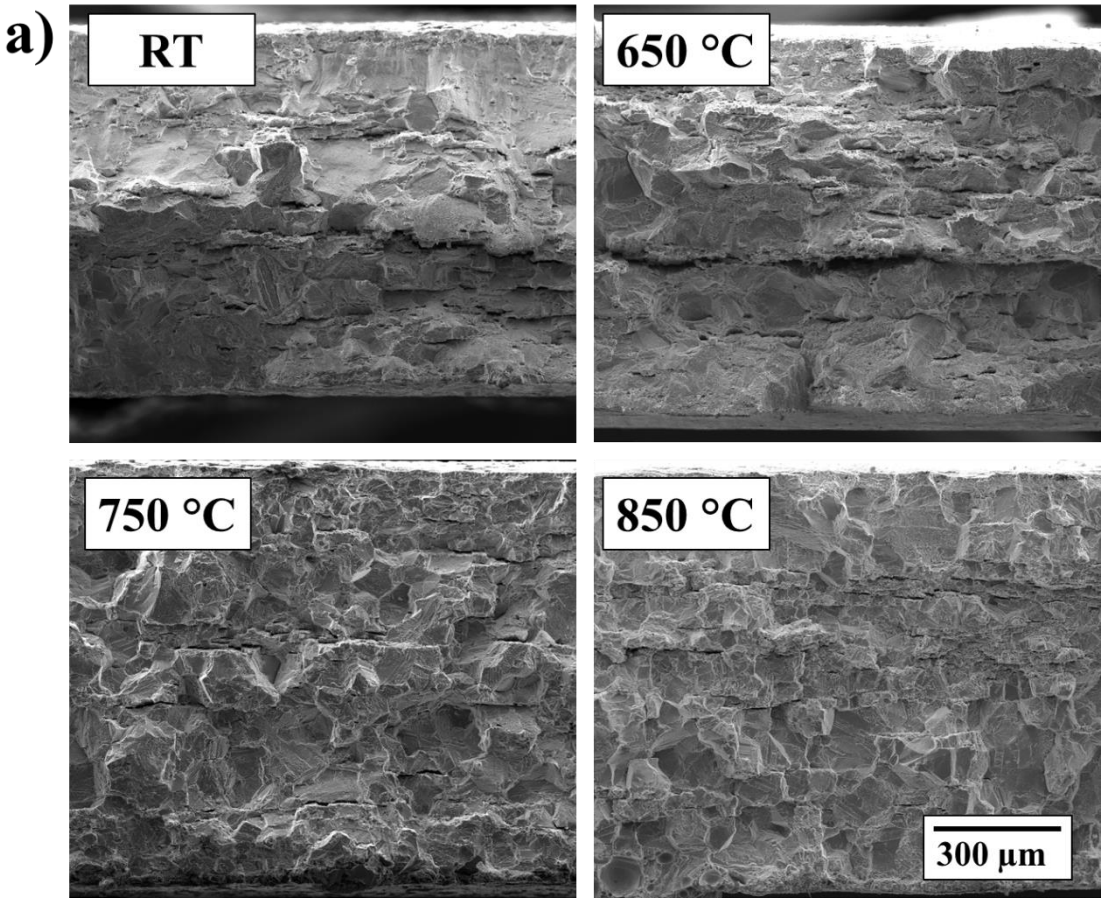

Figure 5.35: Continued on next page.

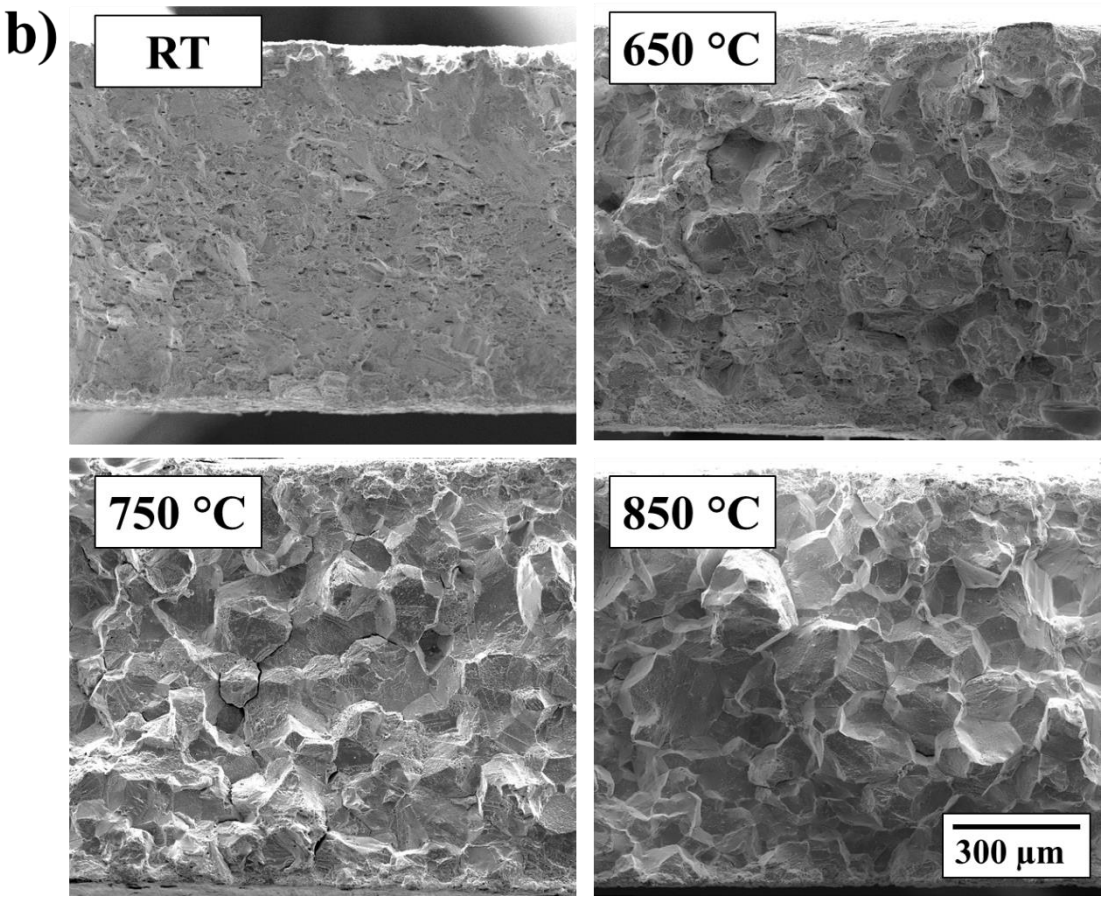

Figure 5.35: continued on next page.

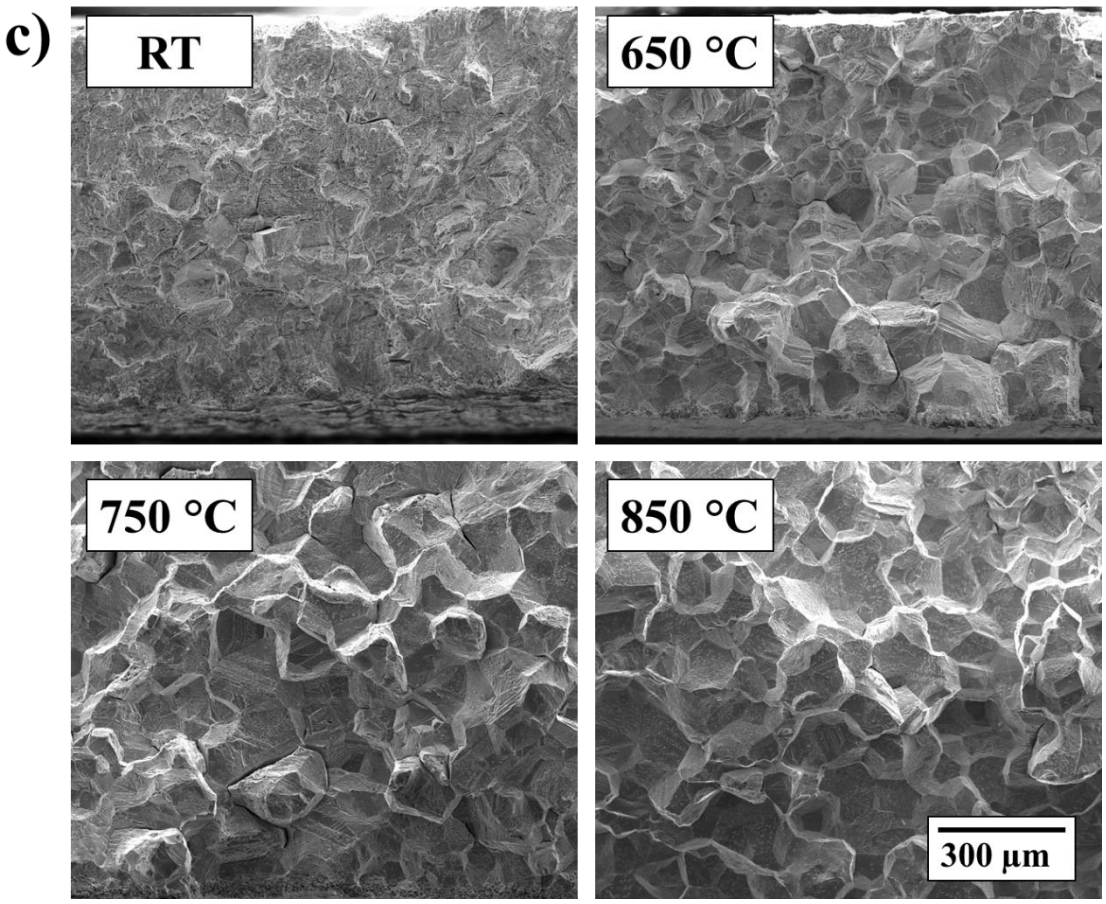

Figure 5.35: (Figure continued from previous page) SEM images acquired using Everhart-Thornley detector of the fracture surface of tensile test specimens of (a) $Cr_{20}Co_{12.5}Ni_{60}Al_{2.5}Ti_5$, (b) $Cr_{22.5}Co_{10}Ni_{60}Al_5Ti_{2.5}$, and (c) $Cr_{20}Co_{17.5}Ni_{50}Al_{12.5}$ alloys tested at different temperatures. All images were acquired at same magnification.

The yield strength of $Cr_{20}Co_{12.5}Ni_{60}Al_{2.5}Ti_5$, $Cr_{22.5}Co_{10}Ni_{60}Al_5Ti_{2.5}$, and $Cr_{20}Co_{17.5}Ni_{50}Al_{12.5}$ alloys as a function of the test temperature is shown in Figure 5.36. The error bars represent the standard deviation of the measurements. Table 3.2 is repeated here for sake of comparation between the modeling predictions and the experimentally measured yield strength.

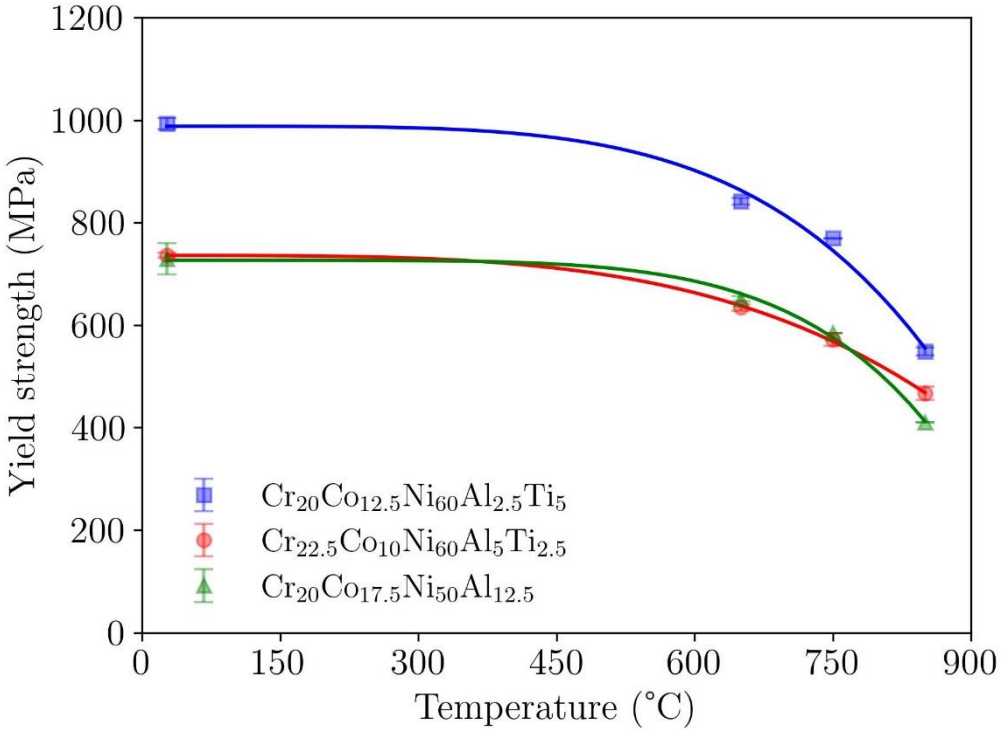

Figure 5.36: Yield strength as function of tensile test temperature for $Cr_{20}Co_{12.5}Ni_{60}Al_{2.5}Ti_5$, $Cr_{22.5}Co_{10}Ni_{60}Al_5Ti_{2.5}$, and $Cr_{20}Co_{17.5}Ni_{50}Al_{12.5}$ alloys. Tests were performed under a strain rate of 10^{-3}s.

Table 3.2: Equilibrium molar fraction of $L1_2$ phase at 750 °C (f_{L12}), solid solution hardening contribution to yield strength (σ_{ss}), and precipitation hardening contribution to yield strength (σ_{pp}) for $Cr_{20}Co_{12.5}Ni_{60}Al_{2.5}Ti_5$, $Cr_{22.5}Co_{10}Ni_{60}Al_5Ti_{2.5}$, and $Cr_{20}Co_{17.5}Ni_{50}Al_{12.5}$ alloys.

Alloy	σ_{ss} (MPa)	f_{L12} at 750 °C	χ_{APB} (mJ/m²)	σ_{pp} (MPa)	$\sigma_{ss} + \sigma_{pp}$ (MPa
$Cr_{20}Co_{12.5}Ni_{60}Al_{2.5}Ti_5$	216	0.35	329	1035	1251
$Cr_{22.5}Co_{10}Ni_{60}Al_5Ti_{2.5}$	211	0.34	209	645	856
$Cr_{20}Co_{17.5}Ni_{50}Al_{12.5}$	206	0.49	158	583	790

In all cases, even ignoring the grain boundary hardening mechanism, the proposed model overpredicts the yield strength value. As discussed previously, the peak aged strength contribution equation might fail to quantitatively predict the maximum precipitation hardening contribution but can be used to guide the alloy design. Despite not showing a quantitative agreement, the experimental trend is successfully captured by the proposed methodology. The

$Cr_{20}Co_{12.5}Ni_{60}Al_{2.5}Ti_5$ alloy is in fact the alloy with highest yield stress; even with a volume fraction close to that of $Cr_{22.5}Co_{10}Ni_{60}Al_5Ti_{2.5}$, its strength is 35% higher. This demonstrates that not only the volume fraction but also the antiphase boundary energy estimation should be taking into considering during design of alloys with optimized yield stress, which is well captured by the modeling. Furthermore, even with quite different volume fraction of precipitates, the yield strength of the two latter alloys were close, which is also well captured by the proposed methodology. Therefore, the proposed model provides a promising path for the faster identification and development of new alloys with optimized mechanical properties. Moreover, other variables such as density and alloy's cost can be easily calculated and added to the proposed model, aiding in the choice of the best alloy for a giving application.

Since discontinuous precipitation may be responsible for the reduced ductility observed in the alloys, a step further was made to try to mitigate its formation. The growth of discontinuous precipitation colonies may occur by diffusion through the lattice or by diffusion through the grain boundaries. The former is usually the dominant diffusion mechanism at high homologous temperatures, whereas the latter dominates at low homologous temperatures [131]. To investigate the influence of temperature on the discontinuous precipitation reaction, the selected alloys were aged for 50h at 750, 850, and 950 °C. Their microstructure was characterized by SEM, and the results are presented in the Figure 5.37.

Additionally, high energy X-ray diffraction (HEXRD) was carried out on these samples to identify the phases present and evaluate any potential phase transformation at higher aging temperatures. The diffraction patterns are displayed in the Figure 5.38, which revealed the presence of only the FCC, $L1_2$, and inclusion phases. The carbides observed previously by line EDS analyses could not be identified, most likely due to their low volume fraction.

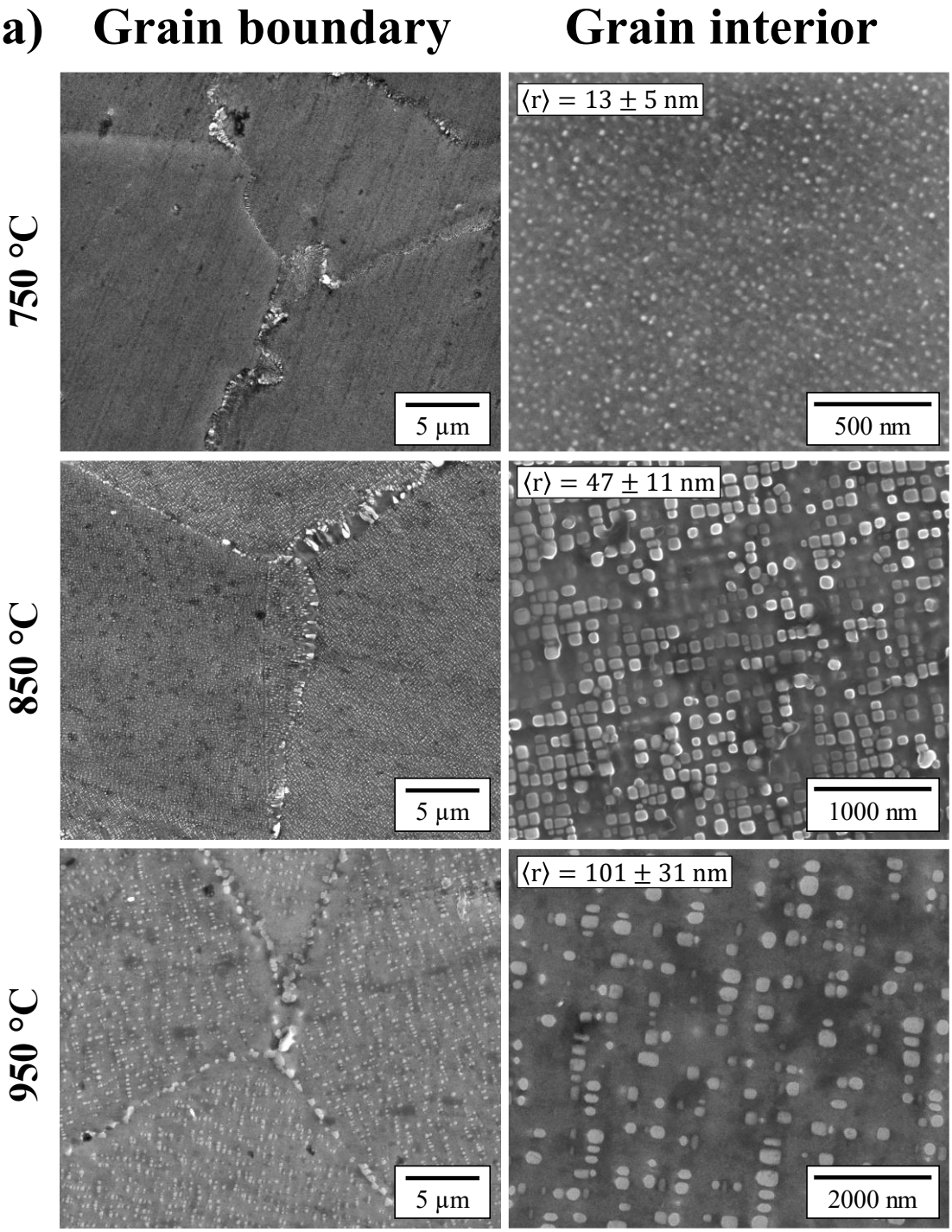

Figure 5.37: (Figure continued next page)

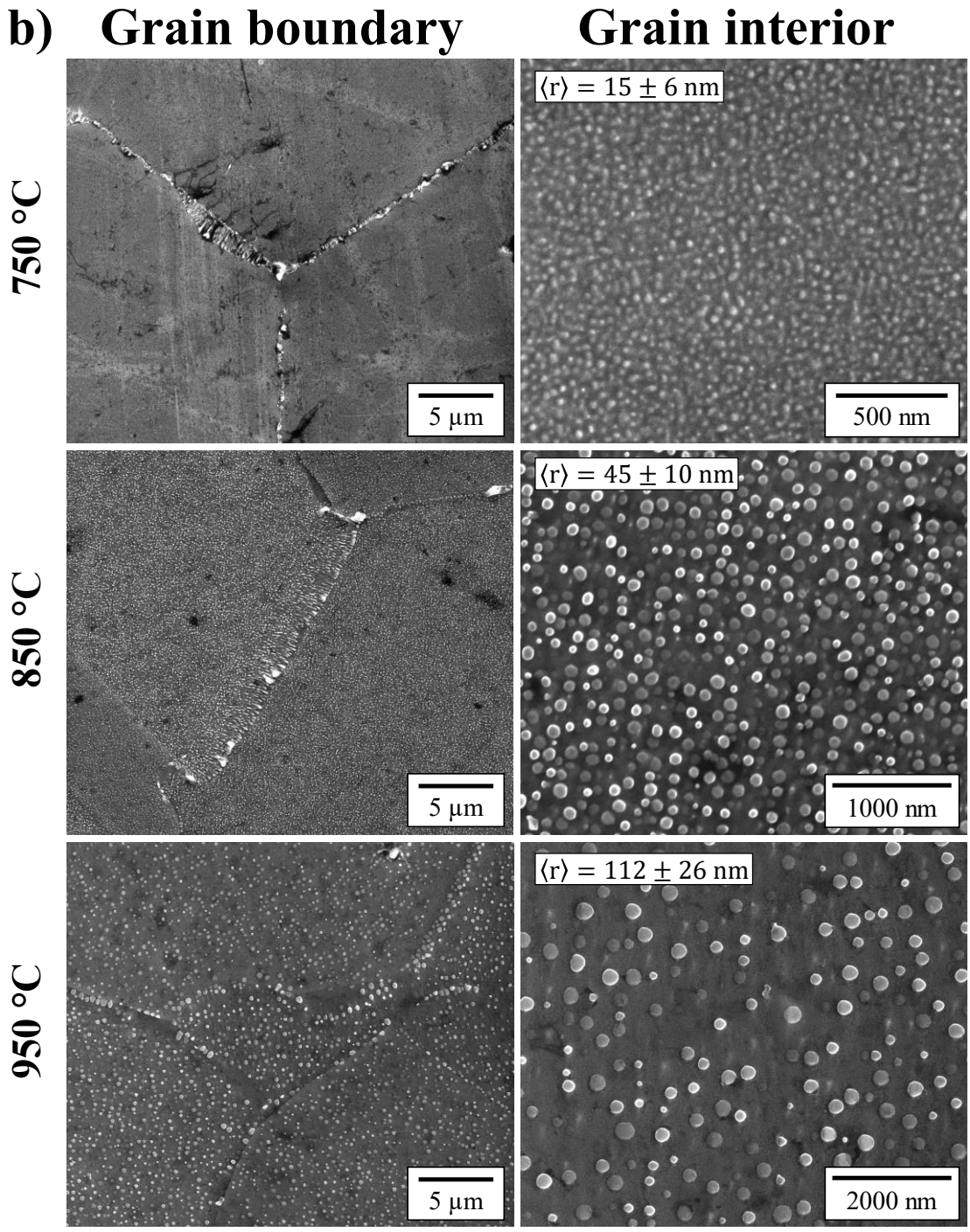

Figure 5.37: (Figure continued next page)

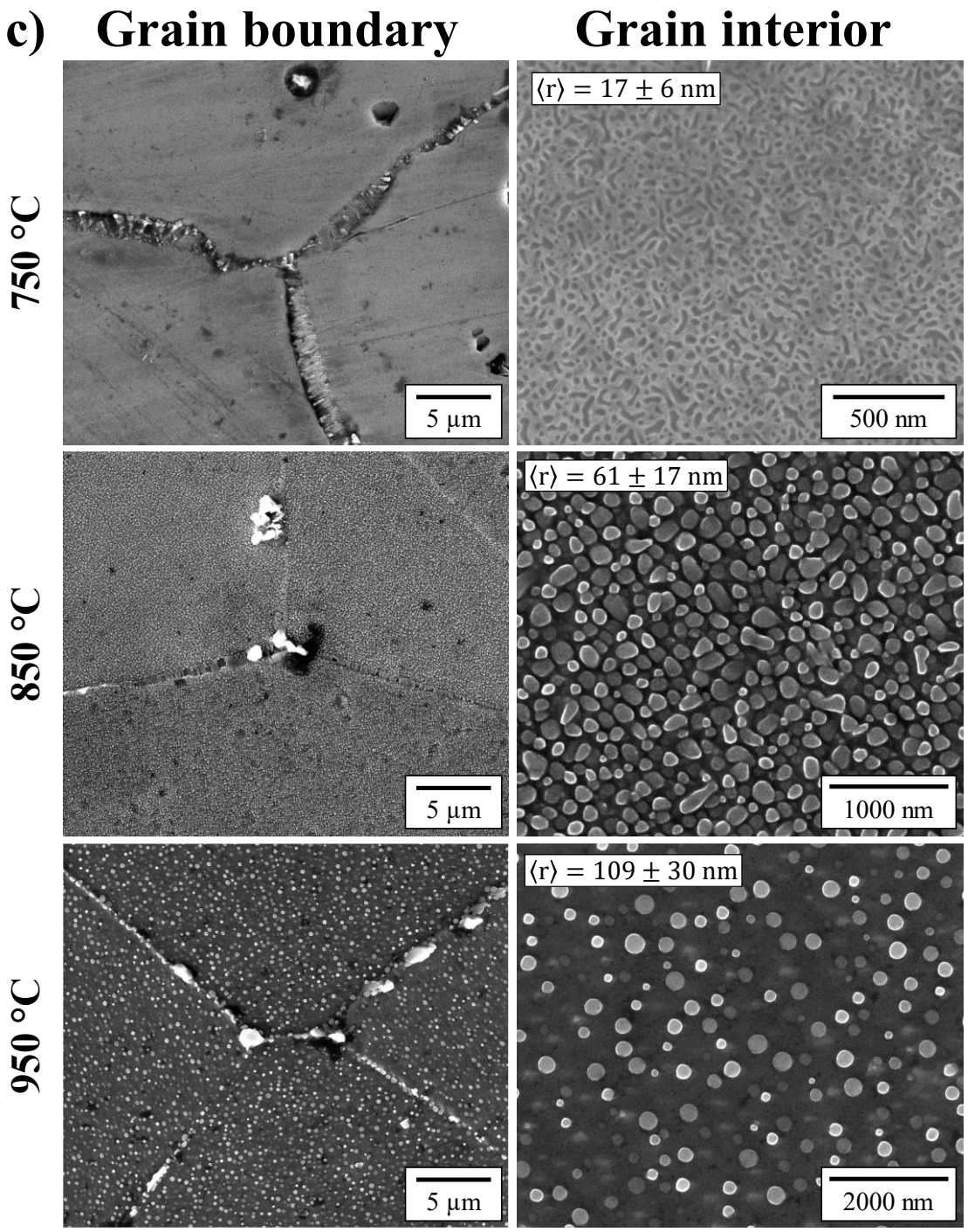

Figure 5.37: (Figure continued from previous page). Grain boundary and grain interior microstructure of (a) $Cr_{20}Co_{12.5}Ni_{60}Al_{2.5}Ti_5$, (b) $Cr_{22.5}Co_{10}Ni_{60}Al_5Ti_{2.5}$, and (c) $Cr_{20}Co_{17.5}Ni_{50}Al_{12.5}$ alloys after aging treatment at 750, 850 e 950 °C for 50h.

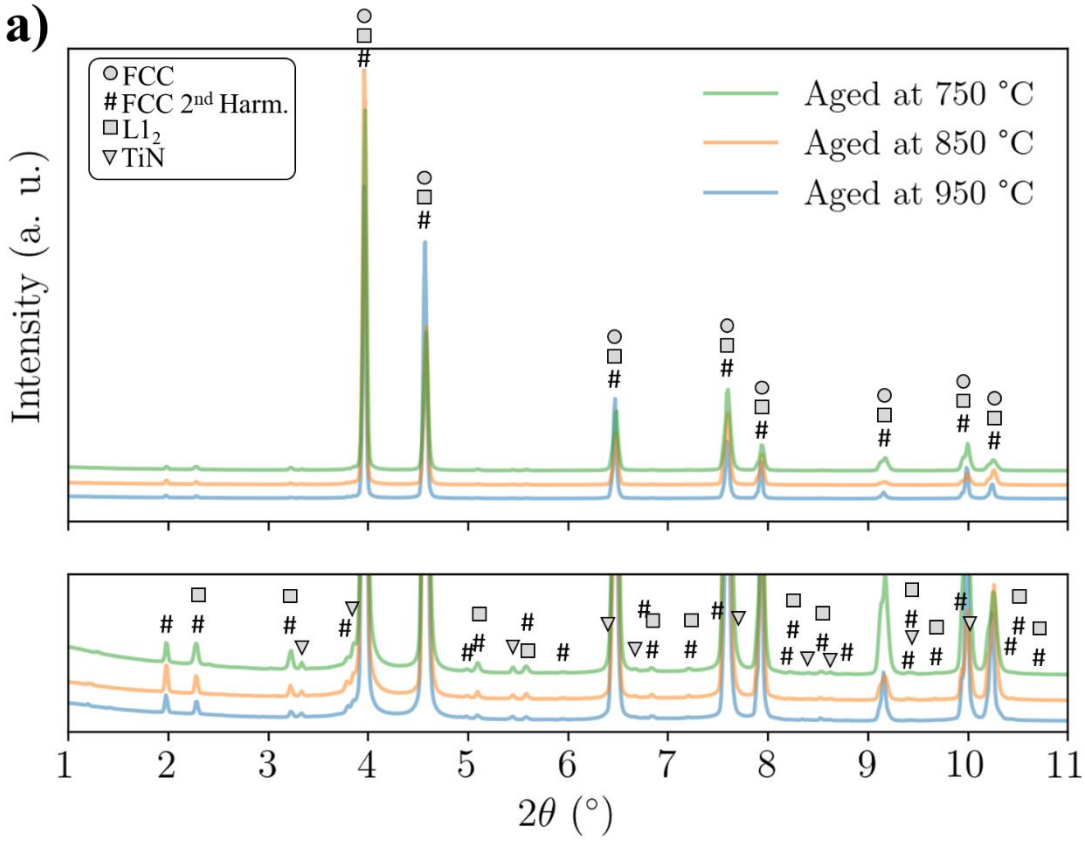

Figure 5.38: (Figure continued next page)

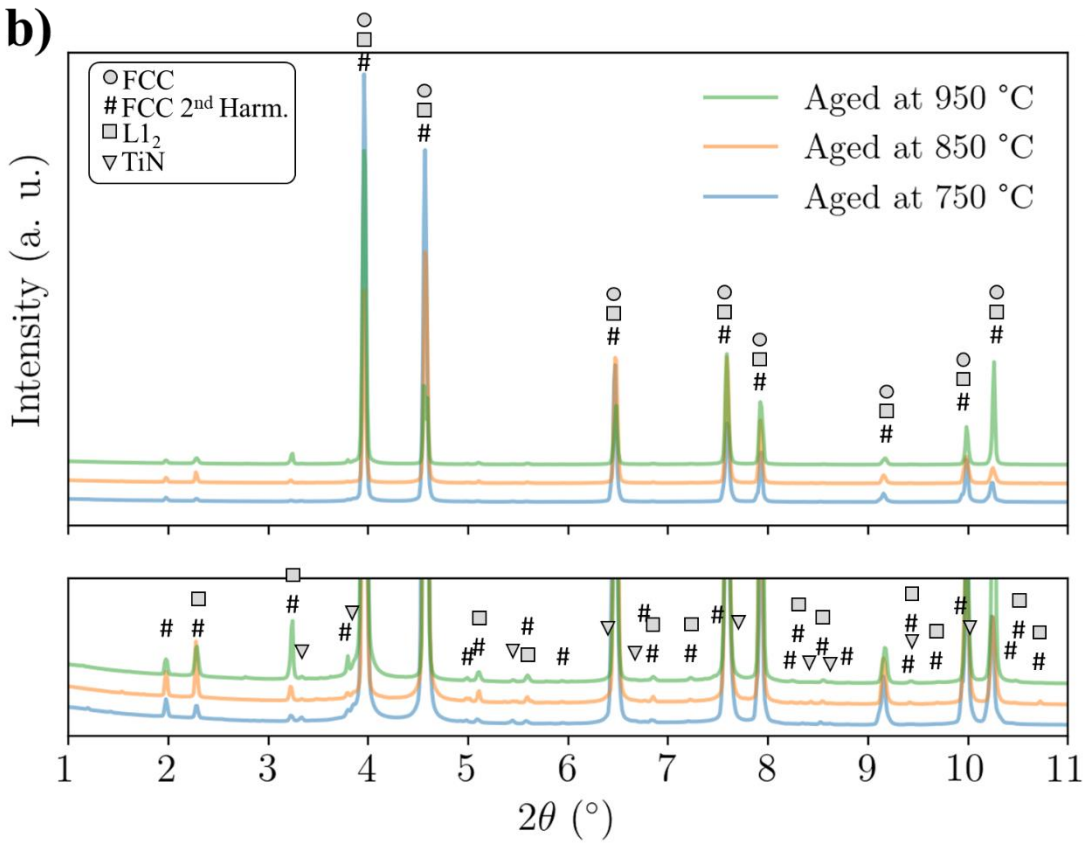

Figure 5.38: (Figure continued next page)

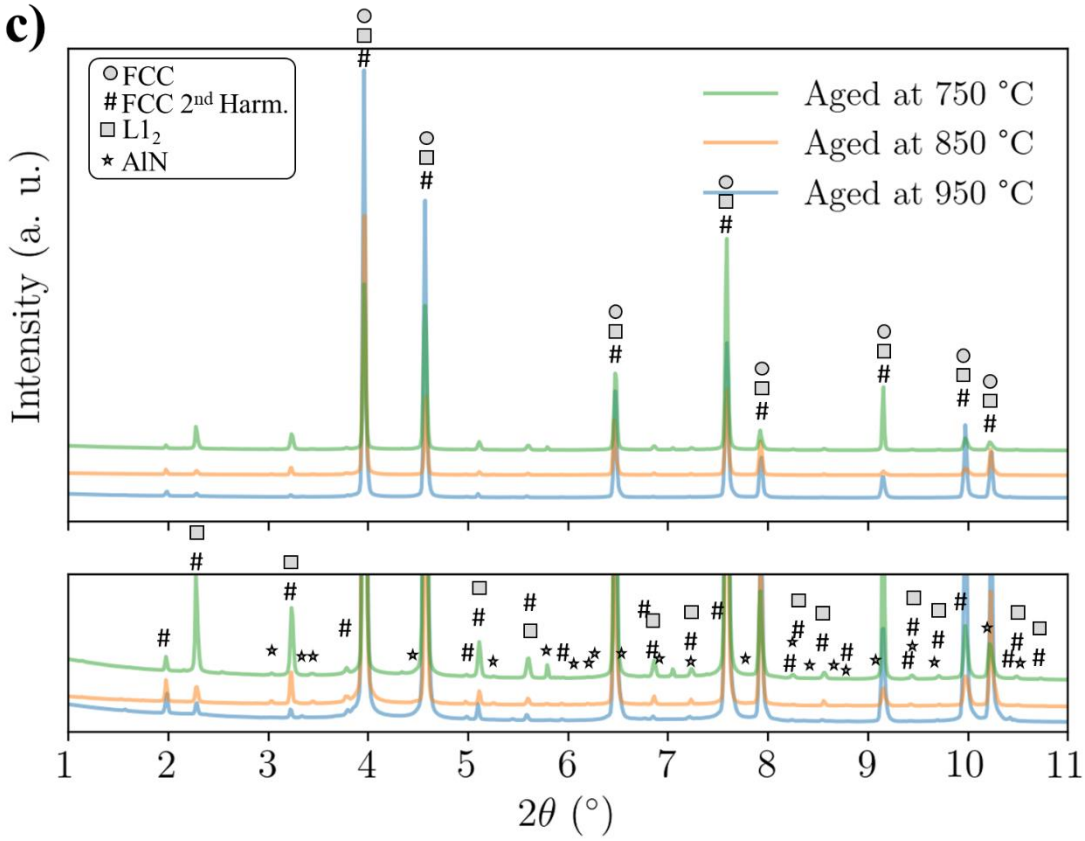

Figure 5.38: (Figure continued from previous page). High energy X-ray diffraction of (a) $Cr_{20}Co_{12.5}Ni_{60}Al_{2.5}Ti_5$, (b) $Cr_{22.5}Co_{10}Ni_{60}Al_5Ti_{2.5}$, and (c) $Cr_{20}Co_{17.5}Ni_{50}Al_{12.5}$ alloys after aging treatment at 750, 850 e 950 °C for 50h.

The discontinuous precipitation in the selected alloys is greatly reduced with increasing aging temperature, as observed from SEM images. However, the equilibrium volume fraction of the $L1_2$ phase decreases with higher temperatures, which leads to a lower contribution to yield strength through precipitation hardening. To improve the ductility of the alloys without reducing their yield stress, an alternative heat treatment route is proposed. This approach involves a first aging treatment at 950°C followed by a secondary aging treatment at 750°C. In the former, the $L1_2$ precipitates formed along grain boundaries may generate a particle pinning effect, significantly retarding the migration of grain boundaries and mitigating the DP reaction. The second aging treatment aims to increase the volume fraction of the $L1_2$ phase, which improves the precipitate hardening contribution to yield strength. By employing this two-stage aging treatment, it may

be possible to balance the strength and ductility of the alloy, achieving an optimal combination of these properties.

6 SUMMARY AND CONCLUSIONS

In this work, two different approaches for designing precipitation-hardened high entropy alloys were presented.

In the first approach, CALPHAD was used to design an alloy ($Cr_{29.7}Co_{29.7}Ni_{35.4}Al_{4.0}Ti_{1.2}$) with a highly concentrated Cr-Co-Ni matrix and $L1_2$ precipitates. The designed alloy was produced, processed, and characterized. Thermodynamic calculation showed a good agreement with experimental results. Chemical composition, volume fraction, and solvus temperature were close to calculated values. Experimental data indicated that particle growth during coarsening is controlled by diffusion mechanism. Particle size distribution showed a good agreement with the results of LSW theory, although some particles with scaled-size larger than the maximum allowable in this theory were observed. Results showed that the precipitates were effective to increase the yield stress of the alloy by about ~55% compared to its homogenized counterpart. Furthermore, a recently developed solid solution strengthening model was coupled with classical grain boundary strengthening, and precipitation hardening models to predict the yield strength of alloys in the Cr-Co-Ni-Al-Ti system.

In the 2nd approach, knowledge gained from the first study was used to propose a new strategy for designing precipitation-hardened HEAs with optimized yield stress. Specifically, equilibrium solidification calculations were performed using the CALPHAD method to screen a series of Cr-Co-Ni-Al-Ti alloys. After applying some filtering criteria, the remaining alloys had their solid solution hardening and maximum precipitation hardening contributions to yield strength estimated. Three alloys were selected to test the effectiveness of the proposed method. These alloys were produced, processed, and characterized. The results showed that the intended microstructure was achieved, with the designed alloys consisting of an FCC matrix containing dispersed $L1_2$ precipitates. The mechanical properties were evaluated by tensile tests at room temperature, 650, 750 and 850 °C. It was observed that the proposed model successfully captures the trends in the yield strength.

Overall, the work presented in this thesis opens up new avenues for high-throughput HEA alloy development. The proposed method is highly versatile and

can be adapted to other systems. The results obtained in this study demonstrate the potential of this approach for accelerating the discovery and development of novel HEAs with tailored properties.

7 RECOMMENDATIONS FOR FUTURE WORK

The findings presented in this thesis have identified certain themes that require further investigation. As such, the following topics are proposed as recommendations for future research:

- Test the proposed methodology with experimental data of yield stress of alloys available in the literature;
- Analyze and develop models that quantitatively capture the precipitation hardening contribution at peak strength;
- Carry out an in-depth characterization of the phases present in the discontinuous precipitation colonies and investigate the discontinuous coarsening mechanism;
- Study the coarsening kinetics, the activation energy for coarsening diffusion, and the distribution of particle sizes in the designed alloys;
- Expand the proposed methodology for design precipitation-hardened alloys in other systems, such as Cr-Co-Ni-Al-Ti-Nb. The latter element tends to increases the APB energy and, thus enhance the precipitation-hardening contribution to yield strength.

8 REFERENCES

[1] B. Cantor, Multicomponent and high entropy alloys, Entropy. 16 (2014) 4749–4768. https://doi.org/10.3390/e16094749.

[2] B.J. Yeh, S.-K.S. Chen, S. Lin, J.J.-Y. Gan, T.-S.T. Chin, T.-T.T. Shun, C.-H.C. Tsau, J.-W. Yeh, S.-K.S. Chen, S. Lin, J.J.-Y. Gan, T.-S.T. Chin, T.-T.T. Shun, C.-H.C. Tsau, S.-Y. Chang, Nanostructured High-Entropy Alloys with Multiple Principal Elements: Novel Alloy Design Concepts and Outcomes, Adv Eng Mater. 6 (2004) 299–303. https://doi.org/10.1002/adem.200300567.

[3] T.K. Chen, T.T. Shun, J.W. Yeh, M.S. Wong, Nanostructured nitride films of multi-element high-entropy alloys by reactive DC sputtering, Surf Coat Technol. 188–189 (2004) 193–200. https://doi.org/10.1016/j.surfcoat.2004.08.023.

[4] J. Yeh, S. Lin, T. Chin, J. Gan, S. Chen, T.-T. Shun, C.-H. Tsau, S.-Y. Chou, Formation of simple crystal structures in Cu-Co-Ni-Cr-Al-Fe-Ti-V alloys with multiprincipal metallic elements, Metallurgical and Materials Transactions A. 35 (2004) 2533–2536. https://doi.org/10.1007/s11661-006-0234-4.

[5] B. Cantor, I.T.H. Chang, P. Knight, A.J.B. Vincent, Microstructural development in equiatomic multicomponent alloys, Materials Science Engineering A. 375–377 (2004) 213–218. https://doi.org/10.1016/j.msea.2003.10.257.

[6] P.-K. Huang, J.-W. Yeh, T.-T. Shun, S.-K. Chen, Multi-Principal-Element Alloys with Improved Oxidation and Wear Resistance for Thermal Spray Coating, Adv Eng Mater. 6 (2004) 74–78. https://doi.org/10.1002/adem.200300507.

[7] J.W. Yeh, Physical Metallurgy of High-Entropy Alloys, Jom. 67 (2015) 2254–2261. https://doi.org/10.1007/s11837-015-1583-5.

[8] M.C. Gao, J.-W. Yeh, P.K. Liaw, Yong Zhang, High-Entropy Alloys Fundamentals and Applications, 1st ed., Springer, 2016. https://doi.org/10.1007/978-3-319-27013-5_12.

[9] D.B. Miracle, O.N. Senkov, A critical review of high entropy alloys and related concepts, Acta Mater. 122 (2017) 448–511. https://doi.org/10.1016/j.actamat.2016.08.081.

[10] I. Toda-Caraballo, A general formulation for solid solution hardening effect in multicomponent alloys, Scr Mater. 127 (2017) 113–117. https://doi.org/10.1016/j.scriptamat.2016.09.009.

[11] I. Toda-caraballo, J.S. Wróbel, S.L. Dudarev, D. Nguyen-manh, P.E.J. Rivera-díaz-del-castillo, Acta Materialia Interatomic spacing distribution in multicomponent alloys, Acta Mater. 97 (2015) 156–169. https://doi.org/10.1016/j.actamat.2015.07.010.

[12] I. Toda-Caraballo, P.E.J. Rivera-Díaz-Del-Castillo, Modelling solid solution hardening in high entropy alloys, Acta Mater. 85 (2015) 14–23. https://doi.org/10.1016/j.actamat.2014.11.014.

[13] I. Toda-Caraballo, E.I. Galindo-Nava, P.E.J. Rivera-Díaz-Del-Castillo, Unravelling the materials genome: Symmetry relationships in alloy properties, J Alloys Compd. 566 (2013) 217–228. https://doi.org/10.1016/j.jallcom.2013.02.148.

[14] G. Bracq, M. Laurent-Brocq, C. Varvenne, L. Perrière, W.A. Curtin, J.-M. Joubert, I. Guillot, Combining experiments and modelling to explore the solid solution strengthening of high and medium entropy alloys, Acta Mater. 177 (2019) 266–279. https://doi.org/10.1016/j.actamat.2019.06.050.

[15] C. Varvenne, A. Luque, W.A. Curtin, Theory of strengthening in fcc high entropy alloys, Acta Mater. 118 (2016) 164–176. https://doi.org/10.1016/j.actamat.2016.07.040.

[16] W.G. Nöhring, W.A. Curtin, Correlation of microdistortions with misfit volumes in High Entropy Alloys, Scr Mater. 168 (2019) 119–123. https://doi.org/10.1016/j.scriptamat.2019.04.012.

[17] M.C. Gao, J.-W. Yeh, P.K. Liaw, Yong Zhang, High-Entropy Alloys Fundamentals and Applications, 1st ed., Springer, 2016. https://doi.org/10.1007/978-3-319-27013-5_12.

[18] P.D. Jablonksi, M.C. Gao, C.S. Carney, N. Doğan, P.D. Jablonksi, J.A. Hawk, D.E. Alman, Design of Refractory High-Entropy Alloys, Jom. 67 (2015) 2653–2669. https://doi.org/10.1007/s11837-015-1617-z.

[19] Y. Zhang, T. Ting, Z. Tang, M.C. Gao, K.A. Dahmen, P.K. Liaw, Z. Ping, Progress in Materials Science Microstructures and properties of high-entropy alloys, Prog Mater Sci. 61 (2014) 1–93. https://doi.org/10.1016/j.pmatsci.2013.10.001.

[20] Z. Li, K.G. Pradeep, Y. Deng, D. Raabe, C.C. Tasan, Metastable high-entropy dual-phase alloys overcome the strength–ductility trade-off, Nature. 534 (2016) 227–230. https://doi.org/10.1038/nature17981.

[21] J.W. Yeh, Recent progress in high-entropy alloys, Annales de Chimie: Science Des Materiaux. 31 (2006) 633–648. https://doi.org/10.3166/acsm.31.633-648.

[22] C.K.H. Borg, C. Frey, J. Moh, T.M. Pollock, S. Gorsse, D.B. Miracle, O.N. Senkov, B. Meredig, J.E. Saal, Expanded dataset of mechanical properties and observed phases of multi-principal element alloys, Sci Data. 7 (2020) 430. https://doi.org/10.1038/s41597-020-00768-9.

[23] F.G. Coury, P. Wilson, K.D. Clarke, M.J. Kaufman, A.J. Clarke, High-throughput solid solution strengthening characterization in high entropy alloys, Acta Mater. 167 (2019) 1–11. https://doi.org/10.1016/j.actamat.2019.01.029.

[24] F.G. Coury, K.D. Clarke, C.S. Kiminami, M.J. Kaufman, A.J. Clarke, High Throughput Discovery and Design of Strong Multicomponent Metallic Solid Solutions, Sci Rep. 8 (2018) 1–10. https://doi.org/10.1038/s41598-018-26830-6.

[25] Z. Wu, H. Bei, G.M. Pharr, E.P. George, Temperature dependence of the mechanical properties of equiatomic solid solution alloys with face-centered cubic crystal structures, Acta Mater. 81 (2014) 428–441. https://doi.org/10.1016/j.actamat.2014.08.026.

[26] B. Gludovatz, A. Hohenwarter, K.V.S. Thurston, H. Bei, Z. Wu, E.P. George, R.O. Ritchie, Exceptional damage-tolerance of a medium-entropy

alloy CrCoNi at cryogenic temperatures, Nat Commun. 7 (2016) 1–8. https://doi.org/10.1038/ncomms10602.

[27] G. Laplanche, A. Kostka, C. Reinhart, J. Hunfeld, G. Eggeler, E.P.P. George, Reasons for the superior mechanical properties of medium-entropy CrCoNi compared to high-entropy CrMnFeCoNi, Acta Mater. 128 (2017) 292–303. https://doi.org/10.1016/j.actamat.2017.02.036.

[28] G.Y. Koga, N. Birbilis, G. Zepon, C.S. Kiminami, W.J. Botta, M. Kaufman, A. Clarke, F.G. Coury, Corrosion resistant and tough multi-principal element Cr-Co-Ni alloys, J Alloys Compd. 884 (2021). https://doi.org/10.1016/j.jallcom.2021.161107.

[29] F. Otto, A. Dlouhý, C. Somsen, H. Bei, G. Eggeler, E.P. George, The influences of temperature and microstructure on the tensile properties of a CoCrFeMnNi high-entropy alloy, Acta Mater. 61 (2013) 5743–5755. https://doi.org/10.1016/j.actamat.2013.06.018.

[30] S. Gorsse, J.P. Couzinié, D.B. Miracle, From high-entropy alloys to complex concentrated alloys, C R Phys. 1 (2018) 1–16. https://doi.org/10.1016/j.crhy.2018.09.004.

[31] J. Chen, X. Zhou, W. Wang, B. Liu, Y. Lv, W. Yang, D. Xu, Y. Liu, A review on fundamental of high entropy alloys with promising high–temperature properties, J Alloys Compd. 760 (2018) 15–30. https://doi.org/10.1016/j.jallcom.2018.05.067.

[32] Y.T. Chen, Y.J. Chang, H. Murakami, S. Gorsse, A.C. Yeh, Designing high entropy superalloys for elevated temperature application, Scr Mater. 187 (2020) 177–182. https://doi.org/10.1016/j.scriptamat.2020.06.002.

[33] S. Praveen, H.S. Kim, High-Entropy Alloys: Potential Candidates for High-Temperature Applications – An Overview, Adv Eng Mater. 20 (2018) 1–22. https://doi.org/10.1002/adem.201700645.

[34] N. Eißmann, U. Mühle, U. Gaitzsch, G. Walther, T. Weißgärber, B. Kieback, Precipitation hardening of high entropy alloy CoCrFeMnNi containing titanium, J Alloys Compd. 857 (2021) 157610. https://doi.org/10.1016/j.jallcom.2020.157610.

[35] V. Nandal, R. Sarvesha, S.S. Singh, E.-W. Huang, Y.-J. Chang, A.-C. Yeh, S. Neelakantan, J. Jain, Influence of pre-deformation on the precipitation characteristics of aged non-equiatomic Co1.5CrFeNi1.5 high entropy alloys with Ti and Al additions, J Alloys Compd. 855 (2021) 157521. https://doi.org/10.1016/j.jallcom.2020.157521.

[36] M. Wang, H. Cui, Y. Zhao, C. Wang, N. Wei, Y. Zhao, X. Zhang, Q. Song, A simple strategy for fabrication of an FCC-based complex concentrated alloy coating with hierarchical nanoprecipitates and enhanced mechanical properties, Mater Des. 180 (2019) 107893. https://doi.org/10.1016/j.matdes.2019.107893.

[37] G.E. Dieter, Mechanical Metallurgy, 3rd ed., McGraw-Hill Education, Singapore, 1986.

[38] A. Argon, Strengthening Mechanisms in Crystal Plasticity, Oxford University Press, 2007. https://doi.org/10.1093/acprof:oso/9780198516002.001.0001.

[39] C.R. LaRosa, M. Shih, C. Varvenne, M. Ghazisaeidi, Solid solution strengthening theories of high-entropy alloys, Mater Charact. 151 (2019) 310–317. https://doi.org/10.1016/j.matchar.2019.02.034.

[40] R. Labusch, A Statistical Theory of Solid Solution Hardening, Physica Status Solidi (b). 41 (1970) 659–669. https://doi.org/10.1002/pssb.19700410221.

[41] N.L. Okamoto, K. Yuge, K. Tanaka, H. Inui, E.P. George, Atomic displacement in the CrMnFeCoNi high-entropy alloy – A scaling factor to predict solid solution strengthening, AIP Adv. 6 (2016) 125008. https://doi.org/10.1063/1.4971371.

[42] W.B. Pearson, A Handbook of Lattice Spacings and Structures of Metals and Alloys, Elsevier, 1958. https://doi.org/10.1016/C2013-0-08243-6.

[43] F.G. Coury, K.D. Clarke, C.S. Kiminami, M.J. Kaufman, A.J. Clarke, High Throughput Discovery and Design of Strong Multicomponent Metallic Solid Solutions, Sci Rep. 8 (2018) 1–10. https://doi.org/10.1038/s41598-018-26830-6.

[44] S. Nag, C. Varvenne, W.A. Curtin, Solute-strengthening in elastically anisotropic fcc alloys, Model Simul Mat Sci Eng. 28 (2020). https://doi.org/10.1088/1361-651X/ab60e0.

[45] A.J. Ardell, Intermetallics as Precipitates and Dispersoids in High-Strength Alloys, in: Intermetallic Compounds. Crystal Structures of Intermetallic Compounds., 1994: pp. 257–286.

[46] K.G. Wang, G.Q. Wang, Phase coarsening in multicomponent systems, Phys Rev E. 95 (2017) 1–9. https://doi.org/10.1103/PhysRevE.95.022609.

[47] A.J. Ardell, The effect of volume fraction on particle coarsening: theoretical considerations, Acta Metallurgica. 20 (1972) 61–71. https://doi.org/10.1016/0001-6160(72)90114-9.

[48] A.J. Ardell, V. Ozolins, Trans-interface diffusion-controlled coarsening, Nat Mater. 4 (2005) 309–316. https://doi.org/10.1038/nmat1340.

[49] I.M. Lifshitz, V.V. Slyozov, The kinetics of precipitation from supersaturated solid solutions, Journal of Physics and Chemistry of Solids. 19 (1961) 35–50. https://doi.org/10.1016/0022-3697(61)90054-3.

[50] V.C. Wagner, Theorie der Alterung von Niederschlägen durch Umlösen (Ostwald-Reifung), Z. Elektrochem. 65 (1961) 581–591. https://doi.org/10.1002/bbpc.19610650704.

[51] A.J. Ardell, Precipitation hardening, Metallurgical Transactions A. 16 (1985) 2131–2165. https://doi.org/10.1007/BF02670416.

[52] E. Nembach, G. Neite, Precipitation hardening of superalloys by ordered γ′-particles, Prog Mater Sci. 29 (1985) 177–319. https://doi.org/10.1016/0079-6425(85)90001-5.

[53] Eckhard Nembach, Particle Strengthening of Metals and Alloys, 1st ed., Wiley-VCH, 1996.

[54] A.B. Kamara, A.J. Ardell, C.N.J. Wagner, Lattice Misfits in Four Binary Ni-Base 7/3" Alloys at Ambient and Elevated Temperatures, n.d.

[55] S. V. Prikhodko, H. Yang, A.J. Ardell, J.D. Carnes, D.G. Isaak, Temperature and composition dependence of the elastic constants of Ni3Al, Metallurgical and Materials Transactions A. 30 (1999) 2403–2408. https://doi.org/10.1007/s11661-999-0248-9.

[56] B. Noble, S.J. Harris, K. Dinsdale, Yield characteristics of aluminium–lithium alloys, Metal Science. 16 (1982) 425–430. https://doi.org/10.1179/030634582790427523.

[57] Z. Sun, G. Song, J. Ilavsky, G. Ghosh, P.K. Liaw, Nano-sized precipitate stability and its controlling factors in a NiAl-strengthened ferritic alloy, Sci Rep. 5 (2015) 1–9. https://doi.org/10.1038/srep16081.

[58] J.W. Goodrum, B.G. Lefevre, Strengthening by ordered precipitates in a Ni−Ni4Mo system, Metallurgical Transactions A. 8 (1977) 939–943. https://doi.org/10.1007/BF02661576.

[59] D.H. Jack, R.W.K. Honeycombe, Age hardening of an Fe-Ti-Si alloy, Acta Metallurgica. 20 (1972) 787–796. https://doi.org/10.1016/0001-6160(72)90126-5.

[60] M.C. Chaturvedi, D.W. Chung, Yielding behavior of a γ''-precipitation strengthened Co Ni Cr Nb Fe alloy, Metallurgical Transactions A. 12 (1981) 77–81. https://doi.org/10.1007/BF02648511.

[61] W. Hüther, B. Reppich, Order hardening of MgO by large precipitated volume fractions of spinel particles, Materials Science and Engineering. 39 (1979) 247–259. https://doi.org/10.1016/0025-5416(79)90063-6.

[62] A.J. Ardell, V. Munjal, D.J. Chellman, Precipitation hardening of Ni-Al alloys containing large volume fractions of γ′, Metallurgical Transactions A. 7 (1976) 1263–1268. https://doi.org/10.1007/BF02658809.

[63] B. Reppich, Particle Strengthening, in: R.W. Cahn, P. Haasen, E.J. Kramer (Eds.), Plastic Deformation and Fracture of Materials, in Materials Science and Technology : A Comprehensive Treatment, Volume 6, VCH, 1993: pp. 311–357.

[64] R.C. Reed, The Superalloys, Cambridge University Press, Cambridge, 2006. https://doi.org/10.1017/CBO9780511541285.

[65] R.W. Kozar, A. Suzuki, W.W. Milligan, J.J. Schirra, M.F. Savage, T.M. Pollock, Strengthening Mechanisms in Polycrystalline Multimodal Nickel-Base Superalloys, Metallurgical and Materials Transactions A. 40 (2009) 1588–1603. https://doi.org/10.1007/s11661-009-9858-5.

[66] S. Ochial, Y. Oya, T. Suzuki, Alloying behaviour of Ni3Al, Ni3Ga, Ni3Si and Ni3Ge, Acta Metallurgica. 32 (1984) 289–298. https://doi.org/10.1016/0001-6160(84)90057-9.

[67] E. Chen, A. Tamm, T. Wang, M.E. Epler, M. Asta, T. Frolov, Modeling antiphase boundary energies of Ni3Al-based alloys using automated density functional theory and machine learning, NPJ Comput Mater. 8 (2022). https://doi.org/10.1038/s41524-022-00755-1.

[68] G. Cacciamani, AN INTRODUCTION TO THE CALPHAD METHOD AND THE COMPOUND ENERGY FORMALISM (CEF), Tecnol Metal Mater Min. 13 (2016) 16–24. https://doi.org/10.4322/2176-1523.1048.

[69] B. Sundman, Q. Chen, Y. Du, A Review of Calphad Modeling of Ordered Phases, J Phase Equilibria Diffus. 39 (2018) 678–693. https://doi.org/10.1007/s11669-018-0671-y.

[70] D. Baither, C. Rentenberger, H.P. Karnthaler, E. Nembach, Three alternative experimental methods to determine the antiphase-boundary energies of the γ ′ precipitates in superalloys, Philosophical Magazine A. 82 (2002) 1795–1805. https://doi.org/10.1080/01418610210131407.

[71] D.J.H. Cockayne, I.L.F. Ray, M.J. Whelan, Investigations of dislocation strain fields using weak beams, Philosophical Magazine. 20 (1969) 1265–1270. https://doi.org/10.1080/14786436908228210.

[72] C. BARRETEAU, A. LOISEAU, C. RICOLLEAU, F. DUCASTELLE, Weak beam study of antiphase boundaries in Fe-27%Al as a function of temperature, Le Journal de Physique IV. 04 (1994) C3-65-C3-73. https://doi.org/10.1051/jp4:1994309.

[73] K.J. Hemker, M.J. Mills, Measuring APB and CSF Energies in Ni_3Al with Weak-Beam TEM and Image Simulations, Solid State Phenomena. 35–36 (1993) 449–454. https://doi.org/10.4028/www.scientific.net/SSP.35-36.449.

[74] Y.Q. Sun, P.M. Hazzledine, A TEM weak-beam study of dislocations in γ' in a deformed Ni-based superalloy, Philosophical Magazine A. 58 (1988) 603–617. https://doi.org/10.1080/01418618808209940.

[75] K.J. Hemker, M.J. Mills, Measurements of antiphase boundary and complex stacking fault energies in binary and B-doped Ni $_3$ Al using TEM, Philosophical Magazine A. 68 (1993) 305–324. https://doi.org/10.1080/01418619308221207.

[76] K.J. Hemker, M.J. Mills, Measuring APB and CSF Energies in Ni₃Al with Weak-Beam TEM and Image Simulations, Solid State Phenomena. 35–36 (1993) 449–454. https://doi.org/10.4028/www.scientific.net/SSP.35-36.449.

[77] D.J. Crudden, A. Mottura, N. Warnken, B. Raeisinia, R.C. Reed, Modelling of the influence of alloy composition on flow stress in high-strength nickel-based superalloys, Acta Mater. 75 (2014) 356–370. https://doi.org/10.1016/j.actamat.2014.04.075.

[78] B. Reppich, P. Schepp, G. Wehner, Some new aspects concerning particle hardening mechanisms in γ' precipitating nickel-base alloys—II. Experiments, Acta Metallurgica. 30 (1982) 95–104. https://doi.org/10.1016/0001-6160(82)90049-9.

[79] A.J. Ardell, J.C. Huang, Antiphase boundary energies and the transition from shearing to looping in alloys strengthened by ordered precipitates, Philos Mag Lett. 58 (1988) 189–197. https://doi.org/10.1080/09500838808214752.

[80] P.A. Flinn, Theory of Deformation in Superlattices, Transactions of the American Institute of Mining and Metallurgical Engineers. 218 (1960) 145–154.

[81] A.G. Khachaturyan, J.W. Morris, The interfacial tension of a sharp antiphase domain boundary, Philosophical Magazine A: Physics of Condensed Matter, Structure, Defects and Mechanical Properties. 56 (1987) 517–532. https://doi.org/10.1080/01418618708214403.

[82] V. Paidar, The structure and energy of antiphase boundaries in Ll2 alloys, Acta Metallurgica. 33 (1985) 1803–1811. https://doi.org/10.1016/0001-6160(85)90004-5.

[83] G. Inden, S. Bruns, H. Ackermann, Antiphase boundary energies in ordered f.c.c. alloys, Philosophical Magazine A. 53 (1986) 87–100. https://doi.org/10.1080/01418618608242809.

[84] A.P. Miodownik, N. Saunders, The calculation of APB energies in L12 compounds using a thermodynamic database, Applications of Thermodynamics in the Synthesis and Processing of Materials, Eds. P. Nash and B. Sundman,(Warrendale, PA: TMS, 1995). 91 (1995) 91–104.

[85] D.M. Collins, H.J. Stone, A modelling approach to yield strength optimisation in a nickel-base superalloy, Int J Plast. 54 (2014) 96–112. https://doi.org/10.1016/j.ijplas.2013.08.009.

[86] N. Saunders, M. Fahrmann, C.J. Small, The application of CALPHAD calculations to Ni-based superalloys, ROLLS ROYCE PLC-REPORT-PNR. (2000) 803–811.

[87] Y.-K. Kim, D. Kim, H.-K. Kim, E.-Y. Yoon, Y. Lee, C.-S. Oh, B.-J. Lee, A numerical model to predict mechanical properties of Ni-base disk superalloys, Int J Plast. 110 (2018) 123–144. https://doi.org/10.1016/j.ijplas.2018.06.011.

[88] M. Dodaran, A.H. Ettefagh, S.M. Guo, M.M. Khonsari, W.J. Meng, N. Shamsaei, S. Shao, Effect of alloying elements on the γ' antiphase boundary energy in Ni-base superalloys, Intermetallics (Barking). 117 (2020) 106670. https://doi.org/10.1016/j.intermet.2019.106670.

[89] K. V. Vamsi, S. Karthikeyan, Modeling APB energies in multicomponent Ni-base superalloys, Intermetallics (Barking). 132 (2021). https://doi.org/10.1016/j.intermet.2021.107124.

[90] O.I. Gorbatov, I.L. Lomaev, Y.N. Gornostyrev, A. V. Ruban, D. Furrer, V. Venkatesh, D.L. Novikov, S.F. Burlatsky, Effect of composition on antiphase boundary energy in <math> <mrow> <msub> <mi>Ni</mi> <mn>3</mn> </msub> <mi>Al</mi> </mrow> </math> based alloys: *Ab initio* calculations, Phys Rev B. 93 (2016) 224106. https://doi.org/10.1103/PhysRevB.93.224106.

[91] S.C.H. Llewelyn, K.A. Christofidou, V.J. Araullo-Peters, N.G. Jones, M.C. Hardy, E.A. Marquis, H.J. Stone, The effect of Ni:Co ratio on the elemental

phase partitioning in γ-γ′ Ni-Co-Al-Ti-Cr alloys, Acta Mater. 131 (2017) 296–304. https://doi.org/10.1016/j.actamat.2017.03.067.

[92] ASTM E8/E8M, Standard Test Methods for Tension Testing of Metallic Materials, 2016. https://doi.org/10.1520/E0008_E0008M-16A.

[93] S.K. Michelic, D. Loder, T. Reip, A. Ardehali Barani, C. Bernhard, Characterization of TiN, TiC and Ti(C,N) in titanium-alloyed ferritic chromium steels focusing on the significance of different particle morphologies, Mater Charact. 100 (2015) 61–67. https://doi.org/10.1016/j.matchar.2014.12.014.

[94] ASM Handbook, Vol 19: Fatigue and Fracture, ASM International, 1996.

[95] T. Philippe, P.W. Voorhees, Ostwald ripening in multicomponent alloys, Acta Mater. 61 (2013) 4237–4244. https://doi.org/10.1016/j.actamat.2013.03.049.

[96] P.L. Goldsmith, The calculation of true particle size distributions from the sizes observed in a thin slice, British Journal of Applied Physics. 18 (1967) 813–830. https://doi.org/10.1088/0508-3443/18/6/317.

[97] P.K. Footner, B.P. Richards, Long-term growth of superalloy y' particles, J Mater Sci. 17 (1982) 2141–2153. https://doi.org/10.1007/BF00540433.

[98] V. Seetharaman, K.B.S. Rao, D. Sundararaman, P. Rodriguez, Precipitation and tensile deformation behaviour of a nimonic 105 superalloy, Acta Metallurgica. 35 (1987) 565–575. https://doi.org/10.1016/0001-6160(87)90180-5.

[99] B. Reppich, W. Kühlein, G. Meyer, D. Puppel, M. Schulz, G. Schumann, Duplex γ′ particle hardening of the superalloy Nimonic PE 16, Materials Science and Engineering. 83 (1986) 45–63. https://doi.org/10.1016/0025-5416(86)90173-4.

[100] K. Bhanu Sankara Rao, V. Seetharaman, S.L. Mannan, P. Rodriguez, Effect of long-term exposure at elevated temperatures on the structure and properties of a nimonic PE 16 superalloy, Materials Science and Engineering. 58 (1983) 93–106. https://doi.org/10.1016/0025-5416(83)90140-4.

[101] E.H. Van der Molen, J.M. Oblak, O.H. Kriege, Control of γ′ particle size and volume fraction in the high temperature superalloy Udimet 700, Metallurgical Transactions. 2 (1971) 1627–1633. https://doi.org/10.1007/BF02913886.

[102] C.S. Jayanth, P. Nash, Experimental evaluation of particle coarsening theories, Materials Science and Technology. 6 (1990) 405–414. https://doi.org/10.1179/026708390790190874.

[103] Y. Guan, Y. Liu, Z. Ma, H. Li, H. Yu, Precipitation and coarsening behavior of γ′ phase in CoNi-base superalloy under different aging treatments, Vacuum. 175 (2020) 109247. https://doi.org/10.1016/j.vacuum.2020.109247.

[104] Y.C. Huang, C.H. Su, S.K. Wu, C. Lin, A study on the hall-petch relationship and grain growth kinetics in FCC-structured high/medium entropy alloys, Entropy. 21 (2019). https://doi.org/10.3390/e21030297.

[105] I. Toda-Caraballo, P.E.J. Rivera-Díaz-Del-Castillo, Modelling solid solution hardening in high entropy alloys, Acta Mater. 85 (2015) 14–23. https://doi.org/10.1016/j.actamat.2014.11.014.

[106] Z.C. Cordero, B.E. Knight, C.A. Schuh, Six decades of the Hall–Petch effect – a survey of grain-size strengthening studies on pure metals, International Materials Reviews. 61 (2016) 495–512. https://doi.org/10.1080/09506608.2016.1191808.

[107] S. Yoshida, T. Ikeuchi, T. Bhattacharjee, Y. Bai, A. Shibata, N. Tsuji, Effect of elemental combination on friction stress and Hall-Petch relationship in face-centered cubic high / medium entropy alloys, Acta Mater. 171 (2019) 201–215. https://doi.org/10.1016/j.actamat.2019.04.017.

[108] S.J. Sun, Y.Z. Tian, H.R. Lin, X.G. Dong, Y.H. Wang, Z.J. Wang, Z.F. Zhang, Temperature dependence of the Hall–Petch relationship in CoCrFeMnNi high-entropy alloy, J Alloys Compd. 806 (2019) 992–998. https://doi.org/10.1016/j.jallcom.2019.07.357.

[109] G.W. Hu, L.C. Zeng, H. Du, X.W. Liu, Y. Wu, P. Gong, Z.T. Fan, Q. Hu, E.P. George, Tailoring grain growth and solid solution strengthening of single-phase CrCoNi medium-entropy alloys by solute selection, J Mater

Sci Technol. 54 (2020) 196–205. https://doi.org/10.1016/j.jmst.2020.02.073.

[110] ASTM E112-96, Standard Test Methods for Determining Average Grain Size, (2004) 1–26.

[111] M.I. Mendelson, Average Grain Size in Polycrystalline Ceramics, Journal of the American Ceramic Society. 52 (1969) 443–446. https://doi.org/10.1111/j.1151-2916.1969.tb11975.x.

[112] C. Varvenne, W.A. Curtin, Strengthening of high entropy alloys by dilute solute additions: CoCrFeNiAl x and CoCrFeNiMnAl x alloys, Scr Mater. 138 (2017) 92–95. https://doi.org/10.1016/j.scriptamat.2017.05.035.

[113] B. Uzer, S. Picak, J. Liu, T. Jozaghi, D. Canadinc, I. Karaman, Y.I. Chumlyakov, I. Kireeva, On the mechanical response and microstructure evolution of NiCoCr single crystalline medium entropy alloys, Mater Res Lett. 6 (2018) 442–449. https://doi.org/10.1080/21663831.2018.1478331.

[114] S.G. Ma, S.F. Zhang, J.W. Qiao, Z.H. Wang, M.C. Gao, Z.M. Jiao, H.J. Yang, Y. Zhang, Superior high tensile elongation of a single-crystal CoCrFeNiAl0.3 high-entropy alloy by Bridgman solidification, Intermetallics (Barking). 54 (2014) 104–109. https://doi.org/10.1016/j.intermet.2014.05.018.

[115] M. Kawamura, M. Asakura, N.L. Okamoto, K. Kishida, H. Inui, E.P. George, Plastic deformation of single crystals of the equiatomic Cr−Mn−Fe−Co−Ni high-entropy alloy in tension and compression from 10 K to 1273 K, Acta Mater. 203 (2021) 116454. https://doi.org/10.1016/j.actamat.2020.10.073.

[116] Z. Wu, Y.F. Gao, H. Bei, Single crystal plastic behavior of a single-phase, face-center-cubic-structured, equiatomic FeNiCrCo alloy, Scr Mater. 109 (2015) 108–112. https://doi.org/10.1016/j.scriptamat.2015.07.031.

[117] X. Li, Z. Li, Z. Wu, S. Zhao, W. Zhang, H. Bei, Y. Gao, Strengthening in Al-, Mo- or Ti-doped CoCrFeNi high entropy alloys: A parallel comparison, J Mater Sci Technol. 94 (2021) 264–274. https://doi.org/10.1016/j.jmst.2021.02.060.

[118] S. Yoshida, T. Bhattacharjee, Y. Bai, N. Tsuji, Friction stress and Hall-Petch relationship in CoCrNi equi-atomic medium entropy alloy processed by

severe plastic deformation and subsequent annealing, Scr Mater. 134 (2017) 33–36. https://doi.org/10.1016/j.scriptamat.2017.02.042.

[119] M. Laurent-Brocq, L. Perrière, R. Pirès, F. Prima, P. Vermaut, Y. Champion, From diluted solid solutions to high entropy alloys: On the evolution of properties with composition of multi-components alloys, Materials Science and Engineering: A. 696 (2017) 228–235. https://doi.org/10.1016/j.msea.2017.04.079.

[120] J.Y. He, W.H. Liu, H. Wang, Y. Wu, X.J. Liu, T.G. Nieh, Z.P. Lu, Effects of Al addition on structural evolution and tensile properties of the FeCoNiCrMn high-entropy alloy system, Acta Mater. 62 (2014) 105–113. https://doi.org/10.1016/j.actamat.2013.09.037.

[121] Y. Tong, D. Chen, B. Han, J. Wang, R. Feng, T. Yang, C. Zhao, Y.L. Zhao, W. Guo, Y. Shimizu, C.T. Liu, P.K. Liaw, K. Inoue, Y. Nagai, A. Hu, J.J. Kai, Outstanding tensile properties of a precipitation-strengthened FeCoNiCrTi0.2 high-entropy alloy at room and cryogenic temperatures, Acta Mater. 165 (2019) 228–240. https://doi.org/10.1016/j.actamat.2018.11.049.

[122] H.-P. Chou, Y.-S. Chang, S.-K. Chen, J.-W. Yeh, Microstructure, thermophysical and electrical properties in AlxCoCrFeNi (0≤x≤2) high-entropy alloys, Materials Science and Engineering: B. 163 (2009) 184–189. https://doi.org/10.1016/j.mseb.2009.05.024.

[123] F.X. Zhang, S. Zhao, K. Jin, H. Xue, G. Velisa, H. Bei, R. Huang, J.Y.P. Ko, D.C. Pagan, J.C. Neuefeind, W.J. Weber, Y. Zhang, Local Structure and Short-Range Order in a NiCoCr Solid Solution Alloy, Phys Rev Lett. 118 (2017) 1–6. https://doi.org/10.1103/PhysRevLett.118.205501.

[124] R. Zhang, S. Zhao, J. Ding, Y. Chong, T. Jia, C. Ophus, M. Asta, R.O. Ritchie, A.M. Minor, Short-range order and its impact on the CrCoNi medium-entropy alloy, Nature. 581 (2020) 283–287. https://doi.org/10.1038/s41586-020-2275-z.

[125] Q. Li, H. Sheng, E. Ma, Strengthening in multi-principal element alloys with local-chemical-order roughened dislocation pathways, Nat Commun. 10 (2019) 3563. https://doi.org/10.1038/s41467-019-11464-7.

[126] E.P. George, W.A. Curtin, C.C. Tasan, High entropy alloys: A focused review of mechanical properties and deformation mechanisms, Acta Mater. 188 (2020) 435–474. https://doi.org/10.1016/j.actamat.2019.12.015.

[127] C.S. Smith, Grains, phases, interfaces: An interpretation of microstructure, Transactions of the Metallurgical Society of AIME. 175 (1948) 15–51.

[128] T. Gladman, P.R.S.L. A, On the theory of the effect of precipitate particles on grain growth in metals, Proc R Soc Lond A Math Phys Sci. 294 (1966) 298–309. https://doi.org/10.1098/rspa.1966.0208.

[129] A. Mitchell, Nitrogen in Superalloys, High Temperature Materials and Processes. 24 (2005) 101–110. https://doi.org/10.1515/HTMP.2005.24.2.101.

[130] M.J. Donachie, S.J. Donachie, Superalloys: A Technical Guide, 2nd ed., ASM International, 2002.

[131] D.A. Porter, K.E. Easterling, M. Sherif, Phase Transformation in Metals and Alloys, 3rd ed., CRC Press, Boca Raton, 2009.

[132] I. Manna, S.K. Pabi, W. Gust, Discontinuous reactions in solids, International Materials Reviews. 46 (2001) 53.

[133] D.B. Williams, E.P. Butler, Grain boundary discontinuous precipitation reactions, International Metals Reviews. 26 (1981) 153–183. https://doi.org/10.1179/imtr.1981.26.1.153.

[134] K.N. Tu, D. Turnbull, Morphology of cellular precipitation of tin from lead-tin bicrystals, Acta Metallurgica. 15 (1967) 369–376. https://doi.org/10.1016/0001-6160(67)90214-3.

[135] R.D. Knutsen, C.I. Lang, J.A. Basson, Discontinuous cellular precipitation in a Cr–Mn–N steel with niobium and vanadium additions, Acta Mater. 52 (2004) 2407–2417. https://doi.org/10.1016/j.actamat.2004.01.031.

[136] C.Y. Barlow, B. Ralph, Observations of cellular transformation products in nickel-base superalloys, J Mater Sci. 14 (1979) 2500–2508. https://doi.org/10.1007/BF00737041.

[137] N. An, Y. Sun, Y. Wu, J. Tian, Z. Li, Q. Li, J. Chen, X. Hui, High temperature strengthening via nanoscale precipitation in wrought CoCrNi-based

medium-entropy alloys, Materials Science and Engineering A. 798 (2020). https://doi.org/10.1016/j.msea.2020.140213.

[138] C.M. Kuo, C.W. Tsai, Effect of cellular structure on the mechanical property of Al0.2Co1.5CrFeNi1.5Ti0.3 high-entropy alloy, Mater Chem Phys. 210 (2018) 103–110. https://doi.org/10.1016/j.matchemphys.2017.10.064.

[139] T. Yang, Y.L. Zhao, L. Fan, J. Wei, J.H. Luan, W.H. Liu, C. Wang, Z.B. Jiao, J.J. Kai, C.T. Liu, Control of nanoscale precipitation and elimination of intermediate-temperature embrittlement in multicomponent high-entropy alloys, Acta Mater. 189 (2020) 47–59. https://doi.org/10.1016/j.actamat.2020.02.059.

[140] J.Y.C. Fang, W.H. Liu, J.H. Luan, T. Yang, Y. Wu, M.W. Fu, Z.B. Jiao, Competition between continuous and discontinuous precipitation in L12-strengthened high-entropy alloys, Intermetallics (Barking). 149 (2022). https://doi.org/10.1016/j.intermet.2022.107655.

[141] L. Fan, T. Yang, J.H. Luan, Z.B. Jiao, Control of discontinuous and continuous precipitation of γ'-strengthened high-entropy alloys through nanoscale Nb segregation and partitioning, J Alloys Compd. 832 (2020). https://doi.org/10.1016/j.jallcom.2020.154903.

[142] J.D. Nystrom, T.M. Pollock, W.H. Murphy, A. Garg, Discontinuous cellular precipitation in a high-refractory nickel-base superalloy, Metallurgical and Materials Transactions A. 28 (1997) 2443–2452. https://doi.org/10.1007/s11661-997-0001-1.

[143] A. Heckl, S. Cenanovic, M. Göken, R.F. Singer, Discontinuous precipitation and phase stability in Re- and Ru-containing nickel-base superalloys, Metall Mater Trans A Phys Metall Mater Sci. 43 (2012) 10–19. https://doi.org/10.1007/s11661-011-0833-6.